Quantum Probings of Curved Spacetimes

by

Wan Cong

A thesis
presented to the University of Waterloo
in fulfillment of the
thesis requirement for the degree of
Doctor of Philosophy
in
Physics

Waterloo, Ontario, Canada, 2021

Examining Committee Membership

The following served on the Examining Committee for this thesis. The decision of the Examining Committee is by majority vote.

External Examiner:	Masahiro Hotta Assistant Professor, Dept. of Physics, Tohoku University
Supervisors:	David Kubiznak Perimeter Institute of Theoretical Physics
	Robert Mann Professor, Dept. of Physics and Astronomy, University of Waterloo
Internal Members:	Niayesh Afshordi Associate Professor, Dept. of Physics and Astronomy, University of Waterloo
	Lucien Hardy Perimeter Institute of Theoretical Physics
Internal-External Member:	Eduardo Martin-Martinez Associate Professor, Dept. of Applied Mathematics, University of Waterloo

Author's Declaration

This thesis consists of material all of which I authored or co-authored: see Statement of Contributions included in the thesis. This is a true copy of the thesis, including any required final revisions, as accepted by my examiners.

I understand that my thesis may be made electronically available to the public.

Statement of Contributions

The contents of this thesis are based on the following publications and forthcoming articles.

Chapter 4 is based on:

> **Wan Cong**, Jiří Bičák, and David Kubizňák, and Robert B. Mann. *Quantum distinction of inertial frames: Local versus global*. Phys. Rev. D, 101:104060, May 2020 [1].

Chapter 5 is based on:

> **Wan Cong**, Jiří Bičák, David Kubizňák, and Robert B. Mann. *Quantum Detection of Inertial Frame Dragging*. Phys. Rev. D, 103(2):024027, 2021 [2].

Chapter 6 is based on:

> **Wan Cong**, Jiří Bičák, David Kubizňák, and Robert B. Mann. *Quantum Detection of Conicity*, Phys. Lett. B, 820:136482, 2021 [3].

Phys. Lett. B, 820:136482, 2021

Chapter 7 is based on:

> **Wan Cong**, Erickson Tjoa, and Robert B. Mann. *Entanglement Harvesting with Moving Mirrors*. JHEP, 06:021, 2019 [4]. [Erratum: JHEP 07, 051 (2019)],
>
> **Wan Cong**, Chen Qian, Michael R. R. Good, and Robert B. Mann. *Effects of Horizons on Entanglement Harvesting*. JHEP, 10:067, 2020 [5].

Chapter 9 is based on:

> Niloofar Abbasvandi, **Wan Cong**, David Kubizňák, and Robert B. Mann. *Snapping swallowtails in accelerating black hole thermodynamics*. Class. Quant. Grav., 36(10):104001, 2019 [6],
>
> Niloofar Abbasvandi, Wasif Ahmed, **Wan Cong**, David Kubizňák, and Robert B. Mann. *Finely Split Phase Transitions of Rotating and Accelerating Black Holes*. Phys. Rev. D, 100(6):064027, 2019 [7].

Abstract

This thesis is divided into two parts. The first part studies the response of Unruh DeWitt detectors in different spacetimes. One of the main goals here is to demonstrate that Unruh DeWitt detectors can detect spacetime features located far from the detectors themselves faster than classical detectors. We do so by placing the detectors in massive shells inside of which the spacetime is flat. We will show that detectors interacting with the quantum vacuum for a finite amount of time will be able to (i) detect the presence of a spherical shell, (ii) differentiate between a static shell and a rotating shell, and (iii) detect conical deficits located outside cylindrical shells. Next, we move on to study how the entanglement harvested between a pair of detectors is affected by the presence of Dirichlet boundaries in 1+1 dimensional Minkowski spacetime. Moving reflecting boundaries lead to particle creation, increasing the noise in the detectors which tends to suppress entanglement. However we find that in general optimal placement of the detectors from the mirror can instead enhance the amount of entanglement harvested as compared to global Minkowski spacetime. Accelerating mirrors which approach the speed of light asymptotically give rise to "information loss" in a toy analogy to the black hole scenario. We show that this leads to a late time linear increase in the entanglement, similar to the behaviour of the regularised entanglement entropy of the field.

In the second part of this thesis we will study the possible phase transitions of slowly accelerating Anti-deSitter black holes. We will do so in the extended phase space, identifying the cosmological constant Λ as a thermodynamic pressure. The acceleration adds another work term to the first law, coming from the tension of the cosmic string pulling on the black hole. We find that while charged slowly accelerating black holes display Van der Waal's type phase transitions like their non-accelerating counterparts, this is only true at low string tensions. At higher string tensions, we find reentrant phase transitions and a no black hole region in the phase diagram not seen in the non-accelerating case. We will also consider rotating slowly accelerating black holes. In addition to the reentrant phase transition in the charged case, rotating black holes can further demonstrate zeroth order phase transitions. The $P-T$ phase diagrams also present subtle differences between the two cases.

Acknowledgements

This thesis would not have been possible without the ideas and insights of my PhD supervisors David Kubiznak and Robert Mann. Thank you so much for your patience and guidance in research and my physics career in general over these four years. To David, thank you for getting me into Perimeter Institute. Even though as a frugal PhD student I did not eat Bistro food, I did enjoy the nice office and the free gym which I found out about only after seeing squash rackets in your office. Happy times :). It is a pity things closed down without giving me a chance to take a shot at the reduced PI concert tickets! I thank Robb for my first actual viewing of the amazing Milky Way bend on the Manitoulin Island and for taking all the nice group photos there which was never shared with the group; for joining weekly group meetings virtually even when on the road or on some remote island (sometimes I wished you were less hardworking). Thank you for making time to discuss physics even when things are up to "here" (I am positioning my hand in a salute style horizontally at a level slightly above my eyebrows). I am also grateful to Jiří Bičák, with whom the trilogy on shells forming three chapters of this thesis was completed. Thank you for all the recommendation letters and for your wise advice and help regarding my future career.

To my undergraduate final year project supervisor Valerio Scarani: thank you for introducing research to me around seven years ago, when I did not know what arXiv was, and for your yearly well-wishes. I will not have my current understanding of quantum physics without your little blue book!

I would also like thank all the members on my PhD advisory committee — Eduardo Martin-Martinez, Niayesh Asfhordi and Lucien Hardy — thank you for your feedbacks during all those committee meetings.

I am also grateful to everyone in Robb and David's research group for all the scientific discussions we have had, especially my collaborators Rahim, with whom I collaborated on my very first PhD project; Erickson, from whom I learnt most Mathematica from; and Niloofar, my office mate and almost-neighbour. Laura and Keith Ng have also been extremely patient with my questions on UDW and Mathematica, thank you!

Last but not least, I would like to thank all my friends for their accompaniment, be it virtually or physically, and for all the happy memories. In alphabetical order, Jia Hui, Rantong, Siong Yin, and Yuliang — sorry for the long list, this is after all, all my friends. Your names are here because I truly appreciate your friendship; please do not feel pressured to do likewise for your PhD/ Masters theses.

*This thesis is dedicated to my parents Mr. Jingwei Cong (*丛晶伟）*and Ms. Xiaoping Ma* （马小辫）*. Thank you for your support, understanding and never-ending offer of financial support; honestly, I am just frugal, not poor!* 爱你们哟！

Table of Contents

Chapter 1

Introduction

This thesis consists of two parts. Part I deals with the detection of spacetime features using Unruh-DeWitt detectors and Part II studies the thermodynamics of accelerating black holes in anti-de Sitter spacetimes. These two seemingly disparate topics are ultimately linked to quantum gravity: the quantum field with which the Unruh-DeWitt detector interacts is quantized on a curved spacetime, a semi-classical approximation of how gravity interacts with quantum matter, while the entropy of a black hole is quantum in origin. In this introductory chapter, I will discuss (i) why a quantum theory of gravity is desirable, (ii) how research in this direction branched into the two topics studied in this thesis and, (iii) the specific questions pursued in later chapters.

For the rest of the thesis, we will work in units where the Planck's constant $\hbar$, gravitational constant G, speed of light c and the Boltzmann's constant k_B are all set to unity and use the convention in which the spacetime metric has the mostly (+) signature.

Why quantum gravity?

The Einstein's field equations

$$G_{\mu\nu} = 8\pi T_{\mu\nu} \tag{1.1}$$

tell us how the curvature of spacetime, described by the Einstein tensor $G_{\mu\nu}$, is sourced by the presence of matter, encoded in the energy-momentum stress tensor $T_{\mu\nu}$. An important example is provided by the energy-momentum tensor of the electromagnetic (EM) field. At low energies, quantum corrections from quantum electro-dynamics (QED) are small, hence the classical EM stress tensor can be used to compute the resulting curvature. However at higher field strengths and energies, quantum effects need to be taken into account.

We then face a difficulty due to the inherent incompatibility between general relativity, where each event has a definite spacetime coordinate, and quantum theory, where events are probabilistic with no definite coordinates. The incompatibility also expresses itself in Eq. (1.1): while the left hand side of (1.1) continues existing as an ordinary tensor field, the stress tensor on the right hand side would be an operator-valued tensor field $\hat{T}_{\mu\nu}$ in the quantum theory. This is the first indication that we need a new theory, one which describes consistently how gravity interacts with quantum fields.

Going to even smaller scales brings us eventually to the Planck length $\ell_p \equiv \left(\frac{G\hbar}{c^3}\right)^{1/2}$, the characteristic length scale obtained from the three fundamental constants. This is the scale where all three effects, quantum ($\hbar$), relativistic (c) and gravity (G) will play equally important roles in explaining physics i.e., no one effect is dominating over the others. It is conjectured that at this scale even gravity and hence spacetime itself should be "quantized". Unfortunately, the corresponding energy scale is so high - about 15 orders of magnitude above the scale at which the Large Hadron Collider operates - that we do not know empirically how quantum gravity behaves, or even if gravity should be quantized at all. Part of the unrelenting enthusiasm in quantizing gravity (see e.g., [8] for more) stems from the hope that it would resolve many of the open problems today, including the singularities and divergences which arise generically respectively in general relativity and quantum field theory (QFT).

The semi-classical picture

In Part I of this thesis, we will not be quantising gravity and will instead work in the semi-classical regime where gravity remains classical but quantum fields are quantised on curved spacetimes. This is expected to be a good approximation describing how gravity affects quantum matter above the Planck scale. Using this technique, Hawking made the groundbreaking discovery of black hole radiation in the seminal paper [9]. This discovery sparked off many interesting questions, such as if unitarity of quantum physics should be preserved, what the source of black hole entropy is and what the end state of black hole evaporation is [10, 11]. Another important discovery made using this technique was the Unruh effect (also known as the Fulling-Davies-Unruh effect) [12, 13, 14] — accelerating observers in the Minkowski vacuum perceive thermal environments with temperatures proportional to their proper accelerations. The utility of this technique also extends to cosmological modelling of inflation, dark energy and so on.

What distinguishes this technique from ordinary QFT is the dependence of quantisation on spacetime geometry and topology, in particular, the background spacetime affects

the quantum state of the field and the entanglement present between different regions. Entanglement in the quantum field [15, 16] is an interesting topic to study not least because it is a hallmark of quantum theory. On the application side, entanglement between Hawking radiation and field modes inside the black hole is the source of the information loss paradox [10, 11]. Holography [17, 18] has also placed entanglement in the spotlight, with suggestions of entanglement entropy being the source of black hole entropy [19] and spacetime geometry itself being built up from entanglement structures [20].

However, the study of entanglement in quantum fields is somewhat hampered by the fact that conventional measures of entanglement such as the von Neumann entropy are formally divergent. An indirect way of studying entanglement in the field is by allowing atoms to interact with the field. The entanglement in the field may be "picked up" by the atoms and we can treat the resulting amount of entanglement between the atoms as a measure of entanglement present in the field (see e.g. [21] for more discussions). For example, this method has been used to probe whether entanglement is severed [22] across a firewall [23] and to study the entanglement present in the quantum vacuum [24, 25]. The use of atoms provides a concrete manifestation of entanglement in a form that we are accustomed to thinking about and is a convenient way to bypass divergences.

Unruh DeWitt detectors

Indeed, while the theoretical entanglement and algebraic structure of the quantum field is a rich and interesting subject, they remain as abstract notions unrelated to observer experiences unless we find ways to probe and extract this information from the field. A central theme of this thesis is the use of the aforementioned atoms for this purpose. For example, we will look at how black holes and boundaries impact the amount of entanglement between two atoms. In addition to studying the entanglement present in the field, we will also demonstrate how vacuum fluctuations of the field, which depend on the global spacetime geometry, affect the spontaneous excitation probability of these atoms. As a result these atoms can be used to detect global spacetime features, presenting a "quantum advantage" in this area over classical detectors.

Following this idea that structures within a quantum field can be operationally probed using atoms, we consider a popular model known as the Unruh-DeWitt (UDW) model. In this model the atom interacts with the field through a monopole type coupling. It was first introduced in [14] to solve the ambiguity of "particles" in curved spacetimes: in general curved spacetimes there are multiple ways to quantize the field, each having different particle contents (see Chapter 2 for more details). The excitation probability of the atom on the other hand is unambiguous. In this sense, the atom is a particle detector, with an

excitation event corresponding to the detection of a field quantum. The Unruh effect, an illustration of the quantum vacuum not being vacuous depending on who is observing it, was first demonstrated using this model.

The versatility of the UDW model makes it useful in studying field properties as it brings abstract concepts into the realm of quantum mechanical systems. Particle detection and study of entanglement structure are two well-known examples. Other fundamental concepts being explored include indefinite causal structure [26] and the existence of a bandlimit in the field [27]. Meanwhile, the model itself can also be optimised, for example, by considering derivative coupling [28], finite versus infinite time coupling [29, 30], coupling to fermionic fields [31, 32], two-level systems versus simple harmonic oscillator systems [33, 34] and so on. Finally, there are also various techniques that can be used to compute the time evolution of the detector-field systems, including perturbation theory and evolution through Master equations. Some of these are reviewed in [35]. These are all examples of active areas of research on UDW detectors.

As mentioned above, spacetime curvature affects the quantization of the field. For example, we would expect the vacuum of Minkowski spacetime to be quite different from that of a black hole spacetime. Indeed, these differences can be picked up again by UDW detectors, as they respond thermally far from a black hole but remain unexcited in Minkowski spacetime. In the first part of this thesis, we shall look at more scenarios in which UDW detectors can be used to detect spacetime features.

Black hole thermodynamics

Besides creating the information paradox [10, 11], the discovery of Hawking radiation also established black holes as thermodynamic systems. The fact that entropy can be attributed to a black hole (see below) is an indication that these gravitational systems do have some quantum degrees of freedom (dof). The central theme of Part II of this thesis is to study a consequence of this quantumness — phase transitions of black holes.

By making use of the semi-classical method above, Hawking discovered in [36] that black holes radiate like black bodies at temperatures T proportional to their surface gravity κ and obey the first law of thermodynamics,

$$\delta M = T\delta S + \Omega\delta J + \Phi\delta Q\,, \tag{1.2}$$

written in terms of the black hole mass M, angular velocity Ω, angular momentum J, electric charge Q, electric potential Φ and entropy S. We see that this is the usual thermodynamic first law if we interpret M as the internal energy of the black hole. Putting

back fundamental constants for the moment, we have

$$T = \frac{\hbar\kappa}{2\pi c k_B}\,, \quad S = \frac{c^3 A}{4G\hbar}\,, \tag{1.3}$$

where the appearance of $\hbar$ in these formulae indicates a quantum origin for these quantities. The anti-deSitter/conformal field theory (AdS/CFT) correspondence [17, 37, 18] conjectures a duality between a bulk quantum gravity theory in AdS and a CFT residing on the boundary of the AdS spacetime. According to the AdS/CFT "dictionary", the temperature and entropy of the black hole in the bulk is dual to the corresponding properties of the field on the boundary. Using this correspondence it was shown that the Hawking-Page transition between AdS black holes and thermal radiation in the bulk is dual to a phase transition in the boundary, being the confinement/deconfinement [18] transition of the gauge theory. The possibility that various bulk black hole transitions can find dual microscopic quantum descriptions on the boundary has ignited much interests in studying thermodynamics of AdS black holes. Comparing the critical phenomenology of black holes to common thermodynamic systems provides insights on the dof of quantum gravity and conversely, black hole phase transitions without analogies to common thermodynamic systems could indicate novel behaviours of strong coupled gauge theories.

The thermodynamic phase space of AdS black holes was extended in [38], where the authors considered the cosmological constant Λ as a thermodynamic variable. Since the contribution of Λ to the Einstein's field equation is equivalent to a fluid stress-energy whose pressure is given by

$$P = -\frac{\Lambda}{8\pi},$$

the authors proposed to view Λ as a thermodynamic pressure. By considering variations in Λ, the first law now becomes [38]

$$\delta M = T\delta S + \Omega\delta J + \Phi\delta Q + V\delta P\,, \tag{1.4}$$

where the conjugate quantity to P is defined as $V \equiv \partial M/\partial P|_{S,J,Q}$, called the thermodynamic volume of the black hole (which in general differs from the geometric volume of the black hole).

The addition of this new pressure-volume term makes the first law look even more like that of common fluids studied in thermodynamics. Note that the mass of the black hole should now be interpreted as the enthalpy of the black hole. For a thermodynamic system having internal energy E, pressure P and volume V, the enthalpy is given by $H = E - PV$. As with usual thermodynamic systems, the various black hole variables can be collected

into an equation of state, expressing $P = P(T, V, Q, J)$. It was shown in [39] that the equation of state of a charged AdS black hole is similar in many aspects to the equation of state of a Van der Waals fluid. If we believe fully in the analogy between black holes and thermodynamic systems, it then follows that charged AdS black holes can undergo first and second order phase transitions in analogy to the liquid-gas transition of Van der Waals fluids. Since then, various possible phase behaviours of AdS black holes have been found (see [40] for a review and more complete references), including reentrant phase transitions [41, 42], triple points [43] and zeroth order phase transitions [41].

Specific directions

In Part I of this thesis, we will look at how global spacetime features can be picked up by UDW detectors. To set up notation, we will begin with two introductory chapters, Chapter 2 on QFT in curved spacetimes and Chapter 3 on UDW detectors. In particular, we will see how to compute the transition probability of the UDW detector using first order perturbation theory as well as how to quantify the amount of entanglement between two detectors. A main observation in these calculations is the dependence of the response of the detector on the two point correlator of the field, which in turn depends on the background geometry. This is the source of the detector's ability to detect spacetime features.

In the following three chapters, we will look at situations in which the UDW detector is placed in the quantum vacuum of a locally Minkowski environment, achieved by surrounding it with massive spherical or cylindrical shells. However outside the shell there may be non-trivial curvature or topological defect. A classical detector placed inside the shell will thus not be able to sense what is outside the shell, or even the presence of the shell, if it is switched on only for a short duration within which no light signal can be transmitted between the detector and the shell. The first consideration of this scenario appeared in [44], which investigated if a UDW can detect the presence of a spherical shell. However, the investigation there stopped at detectors having a *Gaussian* switching profile located at the center of the shell. The Gaussian switching allows the detector to interact with the field for an infinitely long time, even though the interaction is exponentially suppressed at early and late times. One may thus suspect that a detection of the shell is due to signalling. We shall see in Chapter 4 that this is not true by considering *compact* switchings. In addition, by displacing the detector from the center of the shell, we will see that there is an optimal position for shell detection.

In Chapter 5, we spice up the problem by adding rotation to the shell. This will drag inertial frames inside the shell into co-rotation (albeit at a different angular velocity from the shell) with respect to an inertial observer at infinity. This is the Lense-Thirring frame

dragging effect, present whenever there is a rotating massive object. This effect is hard to detect, with the Gravity Probe B experiment taking almost fifty years from its initial conception to final detection of the frame-dragging of the Earth [45]. It is thus interesting to investigate whether the UDW detector can be a better detector of this effect with the help of the quantum field.

The last topic in this series is the detection of a conical deficit present outside a cylindrical shell. If we cut out a wedge (like a pizza slice) from a 2 dimensional (2D) circular disk and paste the two edges together, the resulting 2D manifold will have a conical deficit. In 4D spacetimes, conical deficits are usually used to model cosmic strings, but can also be sourced by cylindrical shells. We will study whether this can be detected by a UDW detector in Chapter 6. The physical difference between this and the previous scenarios is the flatness of the exterior spacetime. Can the detector detect the conical deficit without non-trivial curvature effects?

The last chapter of Part I, Chapter 7, studies how the entanglement between two detectors is affected by moving Dirichlet boundaries. Physically a moving Dirichlet boundary creates particles in what is called the dynamical Casimir effect [46]. This radiation might be expected to create noise, disrupting the entanglement between the detectors. We shall see however that this is not the full story. These boundaries can also mimic radiation from eternal black holes and collapsing shells. In particular, asymptotically null boundaries result in some kind of information loss analogous to the black hole scenario. How will this affect entanglement?

We then begin Part II in Chapter 8 with a quick introduction to black hole thermodynamics in AdS spacetimes. In particular, we review how phase transitions can be inferred from the free energy against temperature diagrams of a system, as well as recall some previously observed phase behaviours of black holes. This sets up the stage for studying the phase transitions of slowly accelerating black holes in Chapter 9. These black holes belong to a constrained set of the C-metric family. Their accelerations can be thought of as being due to the pull coming from cosmic strings attached to either the North or South poles of the black holes. As a result, a new work term $\lambda d\mu$ is added to the first law with μ being the tension of the string and λ its conjugate quantity called the thermodynamic length. We shall see what this new addition harbours for the phase transition of slowly accelerating black holes.

Part I

Probing the Quantum Vacuum

Chapter 2

Quantum Vacuum in Curved Spacetimes

Quantum field theory is a unifying computational technique that offers theoretical predictions for experimental measurements involving matter interacting via three of the four fundamental forces of nature. These are the electromagnetic, weak and strong interactions. On the other hand gravity, the last of these forces, is geometrical, encoded in the curvature of spacetime itself. To describe how classical gravity interacts with the other three quantum forces, one is led to study quantum field theory in curved spacetimes. In this chapter, some concepts of this theory that are relevant for the later chapters will be introduced. These include (i) the classical scalar wave equation, (ii) the Klein-Gordon inner product, (iii) definition of a vacuum state via canonical quantization and (iv) the two point correlator or, the Wightman function, of the field. The description here mainly follows the book [47] in which more details can be found.

2.1 Classical Scalar Field

As the name suggests, quantum field theory deals with quantization of classical fields and therefore we start by introducing a classical field on a curved spacetime. In this thesis, we will only be concerned with a real, free, massless scalar field, which is a simple toy model for more realistic fields such as fermionic fields involved in quantum electrodynamics.

Let $\mathcal{M}$ denote our $(3+1)$-dimensional globally hyperbolic spacetime and let g_{ab} denote the Lorentzian metric tensor. The scalar field that we are interested in is a function

$\Phi : \mathcal{M} \to \mathbb{R}$ satisfying the equation of motion

$$\nabla^a \nabla_a \Phi = 0, \tag{2.1}$$

where ∇ is the covariant derivative associated with g_{ab}. In a coordinate basis x^μ, the equation of motion is written as

$$\frac{1}{\sqrt{-g}} \partial_\mu (\sqrt{-g} g^{\mu\nu} \partial_\nu \Phi), \tag{2.2}$$

where g is the determinant of the metric in this basis.

The equation of motion above can be derived by varying the action,

$$S[\Phi] = -\int_{\mathcal{M}} dt\, d^3\mathbf{x} \sqrt{-g} \frac{1}{2} g^{ab} \partial_a \Phi \partial_b \Phi, \tag{2.3}$$

and requiring $\frac{\delta S}{\delta \Phi} = 0$. In writing down the action $S[\Phi]$, we have specialised to a coordinate $(t, \mathbf{x})$, with $\mathbf{x} = (x^1, x^2, x^3)$, such that the hypersurfaces Σ_t of constant t are Cauchy surfaces. This choice is possible due to global hyperbolicity. From the action, we define the canonical momentum conjugate to the field to be the function $\Pi := \frac{\delta S}{\delta(\partial_t \Phi)}$. We are now ready to quantize the theory.

2.2 Canonical quantization

Canonical quantization proceeds by promoting the field and its conjugate momentum to operators-valued fields $\hat{\Phi}(x)$ and $\hat{\Pi}(x)$, $x \in \mathcal{M}$, acting on some Hilbert space $\mathcal{H}_\Phi$, and satisfying the canonical commutation relations,

$$[\hat{\Phi}(t, \mathbf{x}), \hat{\Pi}(t, \mathbf{x}')] = i\delta^3(\mathbf{x} - \mathbf{x}')\,, \quad [\hat{\Phi}(t, \mathbf{x}), \hat{\Phi}(t, \mathbf{x}')] = 0\,, \quad [\hat{\Pi}(t, \mathbf{x}), \hat{\Pi}(t, \mathbf{x}')] = 0. \tag{2.4}$$

To define the Hilbert space $\mathcal{H}_\Phi$ on which these operators act, let $\mathcal{S}$ denote the space of complex solutions to the scalar wave equation. Further, for any two $\phi_1, \phi_2 \in \mathcal{S}$, define the Klein-Gordon inner product between these two solutions to be

$$(\phi_1, \phi_2) := i \int_{\Sigma_t} d^3x \sqrt{h}\, n^a (\phi_1^* \partial_a \phi_2 - \phi_2 \partial_a \phi_1^*), \tag{2.5}$$

where n^a is the unit normal to Σ_t, h is the determinant of the metric induced on Σ_t and * denotes complex conjugation. This definition is independent of which time slice Σ_t is chosen.

Notice that if $(\phi, \phi) > 0$ then $(\phi^*, \phi^*) = -(\phi, \phi) < 0$ and furthermore, $(\phi, \phi^*) = 0$ i.e., the inner product is not positive definite, and a solution is orthogonal to its complex conjugate. We can thus find orthonormal bases of the form $\{u_k, u_k^*\}$, where k is the index (may be continuous) enumerating the complete basis, such that $(u_k, u_k) > 0$ i.e., the modes u_k have positive definite Klein-Gordon inner product. Given such a basis, we define the creation and annihilation operators $\hat{a}_k^\dagger$, $\hat{a}_k$ associated with these field modes to be the "expansion coefficients" of the field operator in terms of these modes:

$$\hat{\Phi} = \sum_k \hat{a}_k u_k + \hat{a}_k^\dagger u_k^* \,. \tag{2.6}$$

The canonical commutation relations in Eq. (2.4) then implies the following commutation relations for these operators:

$$[\hat{a}_k, a_{k'}^\dagger] = \delta_{kk'} \,, \quad [\hat{a}_k, a_{k'}] = [\hat{a}_k^\dagger, a_{k'}^\dagger] = 0 \,. \tag{2.7}$$

We can then define a vacuum state $|0\rangle$ of the field to be the normalised state annihilated by all the annihilation operators:

$$\hat{a}_k|0\rangle = 0 \quad \forall k \,, \quad \langle 0|0\rangle = 1. \tag{2.8}$$

A state of the form

$$\hat{a}_{k_1}^\dagger a_{k_2}^\dagger ... a_{k_N}^\dagger |0\rangle \,, \tag{2.9}$$

is called an N-particle state. The Hilbert space is then chosen to be the space spanned by $|0\rangle$ and the N-particle states, for $N \in \mathbb{N}$. The condition $(u_k, u_k) > 0$ ensures that the states in this Hilbert space has positive definite inner product, for example,

$$||\hat{a}_k^\dagger|0\rangle||^2 = \langle 0|\hat{a}_k \hat{a}_k^\dagger|0\rangle = \langle 0|[\hat{a}_k, \hat{a}_k^\dagger]|0\rangle = 1 \,. \tag{2.10}$$

We thus have a free massless scalar field quantum theory. We note in passing that the above definition of the vacuum state is not unique since one is free to choose another basis to expand the field operator, giving rise to a different set of annihilation and creation operators.

2.3 Wightman Function

The final quantity to introduce in this chapter is the two-point correlator of the field, which is also known as the Wightman function,

$$W(t, \mathbf{x}; t', \mathbf{x}') := \langle 0|\hat{\Phi}(t, \mathbf{x})\hat{\Phi}(t', \mathbf{x}')|0\rangle \,. \tag{2.11}$$

By substituting expression (2.6) for the expansion of the field into the above, we see that the Wightman function can be written as a sum over the product of the field modes and their complex conjugates:

$$\begin{aligned}\langle 0|\hat{\Phi}(x)\hat{\Phi}(x')|0\rangle &= \sum_{i,j}\langle 0|\big(\hat{a}_i u_i(x) + \hat{a}_i^\dagger u_i^*(x)\big)\big(\hat{a}_j u_j(x') + \hat{a}_j^\dagger u_j^*(x')\big)|0\rangle \\ &= \sum_{i,j}\langle 0|\hat{a}_i u_i(x)\hat{a}_j^\dagger u_j^*(x')|0\rangle \\ &= \sum_{i,j} u_i(x)u_j^*(x')\langle 0|[\hat{a}_i, \hat{a}_j^\dagger]|0\rangle \\ &= \sum_i u_i(x)u_i^*(x')\,. \end{aligned} \tag{2.12}$$

These are all the tools we need from quantum field theory in curved spacetime. In the next chapter, we will be making use of these as we study Unruh-DeWitt detectors.

Chapter 3

Unruh-DeWitt Detectors

3.1 Operational meaning to particle detection

We have briefly mentioned in the previous chapter that the definition of vacuum states of a quantum field in curved spacetimes is not unique. This is due to the fact that in general curved spacetimes, there is no preferred way to choose the basis $\{u_k, u_k^*\}$ with which to expand the field operator. As a result, two vacua $|0\rangle_a$ and $|0\rangle_b$ defined with respect to two different set of creation and annihilation operators $\{\hat{a}_k, \hat{a}_k^\dagger\}$ and $\{\hat{b}_k, \hat{b}_k^\dagger\}$ will in general not agree on the expectation value of number operators, for example, ${}_a\langle 0|\hat{a}_k^\dagger \hat{a}_k|0\rangle_a = 0$, but ${}_a\langle 0|\hat{b}_k^\dagger \hat{b}_k|0\rangle_a \neq 0$ in general. This makes the question "what is the total number of particles in the vacuum $|0\rangle_a$?" ambiguous, since $\sum_k {}_a\langle 0|\hat{a}_k^\dagger \hat{a}_k|0\rangle_a \neq \sum_k {}_a\langle 0|\hat{b}_k^\dagger \hat{b}_k|0\rangle_a$.

An operational way of detecting particles is by using a particle detector model first introduced by Unruh [14] and later simplified by DeWitt [48]. This Unruh-DeWitt (UDW) detector is a quantum mechanical system with two energy states, moving through $\mathcal{M}$ with some trajectory $x(\tau)$ parametrised by the detector's proper time τ. As it moves along this trajectory, the detector interacts with the field via a monopole coupling (see below). If the detector, starting from its initial ground state $|0\rangle_D$ of energy $E_0 = 0$, makes a transition to the excited state $|1\rangle_D$ of energy $E_1 = \Omega > 0$ after interacting with the field, we say that a quantum of energy $E_1 - E_0 = \Omega$ has been detected. This simple model has most famously been used by Unruh to demonstrate the Unruh effect in which the transition probability per unit time of a detector uniformly accelerating through the Minkowski vacuum at proper acceleration a has the same functional dependence on Ω as a detector immersed in a thermal state of the field at temperature $T = 2\pi/a$. In layman's terms, a uniformly accelerating

detector through vacuum sees thermal radiation. We shall also see other applications of the model in the subsequent chapters.

In this chapter we will review the UDW detector with a "switching function" (see for example [49, 29, 30]). The switching function allows us to switch on and off the detector in a smooth manner, avoiding possible divergences in the detector response arising from sharp cut-offs [49, 29, 30]. We will be looking at how the transition probability of a single detector can be computed using first order perturbation theory and also at the entanglement that can be generated when we have two detectors.

3.2 Transition probability of a single UDW detector

Let $\hat{m}(\tau) := e^{i\hat{H}_0\tau}\hat{m}\, e^{-i\hat{H}_0\tau}$ denote the monopole moment of the UDW detector in the interaction picture, where $\hat{m}$ is the Schrodinger picture monopole moment operator and $\hat{H}_0 = \Omega|1\rangle_D\langle 1|_D$ is the free Hamiltonian of the detector. The interaction between the detector and the quantum field is described by the following interaction Hamiltonian:

$$\hat{H}_I(\tau) = \lambda\, \chi(\tau)\, \hat{m}(\tau)\, \hat{\Phi}(x(\tau)). \tag{3.1}$$

In this expression λ is a small coupling constant, $\hat{\Phi}(x(\tau))$ is the field operator evaluated at the spacetime point of interaction with the detector and $0 \leq \chi(\tau) \leq 1$ is a continuous switching function that allows us to the vary the strength of the interaction in time.

Let us initialize the detector-field system at $\tau = -\infty$ in the state $|0\rangle_D|0\rangle$. The final state of the system, which we denote as $|f\rangle$, can be obtained using the unitary time evolution operator $\hat{U}$:

$$\hat{U} = \mathcal{T} \exp\{-i \int_{-\infty}^{\infty} d\tau \hat{H}_I(\tau)\}\,, \tag{3.2}$$

$$|f\rangle = \hat{U}|0\rangle_D|0\rangle\,. \tag{3.3}$$

We have used the symbol $\mathcal{T}$ to represent time ordering of operators, defined as

$$\mathcal{T}\hat{O}_1(t_1)\hat{O}_2(t_2) := \begin{cases} \hat{O}_1(t_1)\hat{O}_2(t_2)\,, \text{if } t_2 < t_1\,, \\ \hat{O}_2(t_2)\hat{O}_1(t_1)\,, \text{if } t_1 < t_2\,, \end{cases} \tag{3.4}$$

for any two time dependent linear operators $\hat{O}_1$ and $\hat{O}_2$.

Assuming that the interaction between the detector and the field is weak so that $\lambda \ll 1$, we can expand the exponential in Eq. (3.2) as,

$$\hat{U} = \hat{I} - i\int_{-\infty}^{\infty} \hat{H}_I(\tau)d\tau + \frac{(-i)^2}{2}\int_{-\infty}^{\infty}\int_{-\infty}^{\infty} \mathcal{T}\hat{H}_I(\tau_1)\hat{H}_I(\tau_2)d\tau_1 d\tau_2 + \mathcal{O}(\lambda^3)\,. \tag{3.5}$$

Substituting this into Eq. (3.3), we can compute the final state $|f\rangle$ to any order in λ. However, we shall only do this to leading order and care only about the final state of the detector by tracing over the field Φ. After a straightforward computation, the final reduced state of the detector $\hat{\rho}_D = \mathrm{Tr}_\Phi(|f\rangle\langle f|)$ is of the form,

$$\hat{\rho}_D = \begin{pmatrix} 1-P_D & 0 \\ 0 & P_D \end{pmatrix} + \mathcal{O}(\lambda^4)\,, \tag{3.6}$$

in the ordered basis $\{|0\rangle_D, |1\rangle_D\}$. A measurement of the detector in this basis will find the detector in the excited state $|1\rangle_D$ with probability P_D. This *excitation probability* takes the form,

$$P_D = \lambda^2\, |{}_D\langle 0|\hat{m}(0)|1\rangle_D|^2 \mathcal{F}(\Omega)\,. \tag{3.7}$$

The factor $\lambda^2\, |{}_D\langle 0|\hat{m}(0)|1\rangle_D|^2$ in front depends only on the internal structure of the detector and neither on the trajectory nor on the field. For this thesis, we shall take

$$\hat{m}(\tau) = e^{-i\Omega\tau}|0\rangle_D\langle 1|_D + e^{i\Omega\tau}|1\rangle_D\langle 0|_D\,, \tag{3.8}$$

which conveniently gives $|{}_D\langle 0|\hat{m}(0)|1\rangle_D|^2 = 1$. The non-trivial part of the transition probability is the second term,

$$\mathcal{F}(\Omega) = \int_{-\infty}^{\infty} d\tau \int_{-\infty}^{\infty} d\tau' \chi(\tau)\chi(\tau') e^{-i\Omega(\tau-\tau')} W(x(\tau); x(\tau'))\,, \tag{3.9}$$

which is called the *response function* of the detector. It depends on the switching of the detector through $\chi(\tau)$, the energy gap of the detector through Ω and the spacetime background through $W(x(\tau); x(\tau'))$, which is the Wightman function evaluated along the detector trajectory. When studying the dependence of $\mathcal{F}$ on Ω it is customary to consider both $\Omega \geq 0$ and $\Omega < 0$. The latter case physically corresponds to initiating the detector in the excited state. We shall be studying how the response function of the UDW depends on Ω and global features of the spacetime in the next chapter.

3.3 Entanglement harvesting with a pair of UDW detectors

3.3.1 Final reduced state

The above results can be generalized easily to the case of two UDW detectors, labeled A and B respectively, interacting independently with the quantum vacuum. In this case our Hilbert space becomes $\mathcal{H}_A \otimes \mathcal{H}_B \otimes \mathcal{H}_\Phi$, where $\mathcal{H}_j$ denotes the Hilbert space of detector $j \in \{A, B\}$. Detectors A and B do not interact directly with each other and the interaction Hamiltonian $\mathcal{H}_{S,I}$ of the full system is given by,

$$\hat{H}_{I,S}(t) = \hat{H}_{I,A}(\tau_A(t))\frac{d\tau_A}{dt} + \hat{H}_{I,B}(\tau_B(t))\frac{d\tau_B}{dt}\,, \tag{3.10}$$

$$\hat{H}_{I,j}(\tau_j) = \lambda_j \chi_j(\tau_j)\hat{u}_j(\tau_j)\hat{\Phi}(x_j(\tau_j))\,. \tag{3.11}$$

The terms λ_j, χ_j, $\hat{m}_j$, x_j and τ_j in the above have the obvious interpretation of being the coupling constant, the switching function, the monopole moment operator, the spacetime trajectory and the proper time respectively, of detector j, while t is an arbitrary time coordinate. For this thesis, we will consider only the case $\lambda_A = \lambda_B$ and $|{}_A\langle 0|\hat{m}_A(0)|1\rangle_A|^2 = |{}_B\langle 0|\hat{m}_B(0)|1\rangle_B|^2 = 1$, that is, the detectors couple to the field with the same strength, and have the same internal structures given by Eq. (3.8).

Initializing the total system in the overall ground state $|0\rangle_S := |0\rangle_A|0\rangle_B|0\rangle$, we can compute the final reduced state $\hat{\rho}_{AB}$ of two detectors using the same procedure as before:

$$\hat{\rho}_{AB} = \mathrm{Tr}_\Phi\left(\hat{U}_S|0\rangle_S\langle 0|_S\hat{U}_S^\dagger\right), \tag{3.12}$$

$$\hat{U}_S = e^{-i\mathcal{T}\int_{-\infty}^{\infty}\left\{\hat{H}_{I,A}(\tau_A(t))\frac{d\tau_A}{dt} + H_{I,B}(\tau_B(t))\frac{d\tau_B}{dt}\right\}dt}, \tag{3.13}$$

where the dummy integration variable t in the second expression above is a common time variable used to parametrize both detectors. This can once again be computed using perturbation theory.

The resulting $\hat{\rho}_{AB}$ when written in the canonical basis $\{|0\rangle_A|0\rangle_B, |0\rangle_A|1\rangle_B, |1\rangle_A|0\rangle_B, |1\rangle_A|1\rangle_B\}$ takes the following form:

$$\hat{\rho}_{AB} = \begin{pmatrix} 1-P_A-P_B & 0 & 0 & X \\ 0 & P_B & C & 0 \\ 0 & C^* & P_A & 0 \\ X^* & 0 & 0 & 0 \end{pmatrix} + \mathcal{O}(\lambda^4)\,. \tag{3.14}$$

As the notation suggests, the terms P_j are the excitation probabilities of the two detectors, given by

$$P_j = \lambda^2 \int_{-\infty}^{\infty} d\tau \int_{-\infty}^{\infty} d\tau' \chi_j(\tau)\chi_j(\tau') e^{-i\Omega(\tau-\tau')} W(x_j(\tau); x_j(\tau')) \,. \tag{3.15}$$

Meanwhile, the term X is related to the *quantum* correlation between the two detectors and it reads

$$\begin{aligned} X = -\lambda^2 \int_{-\infty}^{\infty} \frac{d\tau_A}{dt}\, dt \frac{d\tau'_B}{dt'}\, dt' \chi_A(\tau_A)\, \chi_B(\tau'_B) e^{-i(\Omega_A \tau_A + \Omega_B \tau'_B)} \\ \times \left[\theta(t'-t) W(x_A(\tau_A); x_B(\tau'_B))) + \theta(t-t') W(x_B(\tau'_B); x_A(\tau_A)))\right] , \end{aligned} \tag{3.16}$$

where $\theta(x)$ is the Heaviside step function, and to reduce clutter, we have written $\tau_A(t)$ as τ_A and $\tau'_B(t')$ as τ'_B.

Finally, the last term C is related to the *classical* correlation between the detectors (see for example [50]). We will not be using this term in this thesis but for completeness, it is given by,

$$C = \lambda^2 \int_{-\infty}^{\infty} d\tau_A\, d\tau_B\, \chi_A(\tau_A)\, \chi_B(\tau_B) e^{-i(\Omega_A \tau_A - \Omega_B \tau_B)} W(x_A(\tau_A); x_B(\tau_B))) \,. \tag{3.17}$$

3.3.2 Measuring entanglement

The addition of a second detector into the picture allows us to indirectly probe the entanglement present in the quantum vacuum. Quantum entanglement is what sets quantum and classical systems apart. It enables quantum systems to exhibit measurement statistics that are impossible for what we perceive as classical systems, such as those admitting a local hidden variable model (see for example [51]). While the theory of entanglement is well understood in quantum mechanics, it is harder to describe in the case of quantum fields. As a start, it is already a non-trivial task to to define the parties that are entangled, at least using the rudimentary materials presented in the previous chapter, since we apparently only have the Hilbert space of the single system Φ. Moreover, when we try to generalize usual entanglement measures, such as the von Neumann entropy, to quantum fields, we find that they are usually divergent and requires additional regularization techniques to give useful results [15].

However, two causally separated UDW detectors can become entangled through their interaction with the quantum field. This is due to the entanglement present between the spacetime regions where the two detectors were switched on with the entanglement in the

field being picked up by the detectors. Treating the amount of entanglement between the detectors as a measure of the entanglement in the field brings us back to the familiar realm of studying entanglement between two qubits.

In this realm, we have ready measures to quantify the amount of entanglement present in a state. Formally, an entanglement measure is a non-negative, real-valued function on a density operator, which does not increase under local operations on, and classical communication between, subsystems; it is zero if the state is separable. In our specific case where $\mathcal{H}_A \otimes \mathcal{H}_B = \mathbb{C}^2 \otimes \mathbb{C}^2$, a convenient entanglement measure to use is the *concurrence* $\mathcal{C}$, which is in fact zero if and only if the state is not entangled [52].

Given a density operator $\hat{\rho}$ acting on $\mathbb{C}^2 \otimes \mathbb{C}^2$, its concurrence is defined as

$$\mathcal{C}(\hat{\rho}) := \max[0, \lambda_1 - \lambda_2 - \lambda_3 - \lambda_4] \,, \tag{3.18}$$

where $\lambda_1 \geq \lambda_2 \geq \lambda_3 \geq \lambda_4$ are the square roots of the eigenvalues of $\hat{\rho}\hat{\tilde{\rho}}$ with $\hat{\tilde{\rho}} := (\hat{\sigma}_y \otimes \hat{\sigma}_y) \circ \hat{\rho}^* \circ (\hat{\sigma}_y \otimes \hat{\sigma}_y)$, $\hat{\sigma}_y$ being the Pauli-y operator and $\hat{\rho}^*$ being the adjoint to $\hat{\rho}$.

Despite this complicated definition, computing the concurrence for the resultant state of the two detectors gives a simple expression,

$$\mathcal{C}(\hat{\rho}_{AB}) = 2\max[0, |X| - \sqrt{P_A P_B}] \,. \tag{3.19}$$

Therefore, we see that the state is entangled if and only if $|X| > \sqrt{P_A P_B}$. A mnemonic for remembering this result is: the detectors are entangled if and only if correlation ($|X|$) beats noise ($\sqrt{P_A P_B}$).

In summary, a UDW detector is a qubit that interacts with the quantum field via a monopole coupling. The excitation probability P_D of the detector depends on the spacetime and the trajectory of the detector through the Wightman function of the field. When we have a pair of detectors, we can heuristically view the resultant entanglement between them as being a measure of the amount of entanglement in the field. For our bipartite qubit system, the concurrence $\mathcal{C}$ provides a measure of entanglement. The detectors are entangled if and only if $\mathcal{C} \geq 0$. The generation of entanglement between initially unentangled detectors through interacting with the quantum field has come to be known as entanglement harvesting [53]. We shall look at how entanglement harvesting is affected by moving Dirichlet boundaries in a later chapter.

Chapter 4

Detection of Spherical Shell

We have briefly discussed in the previous chapter how the response of UDW detectors has been used to demonstrate the Unruh effect. Since then, UDW response has been studied in a variety of contexts. These include for example, studying the response in black hole spacetime [54], illustrating the sensitivity to spacetime topology [55, 56, 57, 58] and energy densities [59]. More examples and references can be found in the review [35].

We shall see in this chapter and the subsequent two chapters that a detector interacting locally with the quantum field for a finite amount of time can discern "global features" of $\mathcal{M}$ by extracting information from the quantum field. For example, we know from first year courses that the net gravitational field inside a spherical shell is identically zero. In the language of general relativity, the spacetime inside the shell of radius R is described by the Minkowski metric and is locally flat. However, the spacetime is not globally flat as it is described by the Schwarzchild metric outside the shell. In this chapter, we will demonstrate how the presence or absence of the shell affects the response of a UDW detector placed at the center of the shell. This problem was first considered in [44]. We will mostly follow the set-up there, but instead of using a Gaussian switching function as in [44], we will use a compact switching to ensure that the detector does not communicate with the shell.

This chapter is based on the work done in [1].

4.1 Junction conditions

In each of the scenarios to be considered in this and the next two chapters, the spacetime considered will consist of a timelike hypersurface $\Sigma \subset M$ such that the metric on either

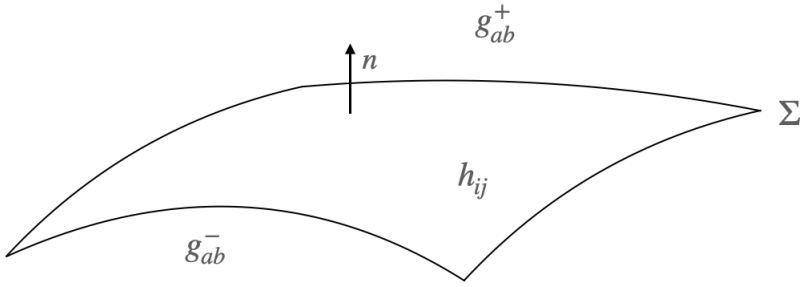

Figure 4.1: Describing junction conditions. Spacetimes comprising of two distinct regions joined at a hypersurface Σ need to satisfy the two junction conditions in the main text. The two distinct regions are associated with metrics g^+_{ab} and g^-_{ab} respectively and n is the unit normal to Σ pointing from $-$ to $+$. The first junction condition says that the induced metric h_{ij} on Σ from both g^+_{ab} and g^-_{ab} must agree.

sides of Σ belong to different families (see Fig. 4.1). Let us denote the two sides of Σ with the $\pm$ sign and use a superscript $\pm$ to represent tensors in either sides of Σ. For example, metric on the $+$ side of Σ will be denoted as g^+_{ab}. In order for these spacetimes to satisfy the Einstein equations in a distributional sense, the following two junction conditions need to be satisfied on Σ (see e.g. [60]).

The first junction condition states that the metrics induced on either side of Σ have to agree:

$$[h_{ij}] = 0\,, \tag{4.1}$$

where h_{ij} is the three dimensional metric induced on Σ by g_{ab}, and $[T] := T^+|_\Sigma - T^-|_\Sigma$ for any tensor T. We are also using $\{i, j, ...\}$ as tensor indices on Σ and $\{a, b, ...\}$ as tensor indices on $\mathcal{M}$.

The second junction condition specifies the stress-energy tensor S_{ij} on Σ:

$$S_{ij} = -\frac{1}{8\pi}\big([K_{ij}] - [K]h_{ij}\big)\,, \tag{4.2}$$

where K_{ij} is the pull back of the extrinsic curvature of Σ to Σ and K is its trace.

In addition to these two junction conditions on the metric and the extrinsic curvature, we will also require two physical boundary conditions on a solution $\Phi(x)$ to the classical scalar field equation. These are the continuity of $\Phi(x)$ and its normal derivative across Σ,

$$[\Phi(x)] = 0 \tag{4.3}$$

$$[\nabla_n \Phi(x)] = 0\,, \tag{4.4}$$

where n is the unit normal to Σ oriented as in Fig. 4.1.

4.2 Scalar field modes

The spacetime describing a spherical shell is obtained by "gluing" together the Schwarzchild spacetime outside the shell with the flat spacetime inside the shell. Using (t, r, θ, ϕ) as our coordinates, the surface Σ where the two metrics are matched is the $r = R$ surface. The metric inside the shell, i.e., $r \leq R$, is the flat Minkowski metric,

$$ds^{2,-} = -f(R)dt^2 + dr^2 + r^2(d\theta^2 + \sin^2\theta d\phi^2), \tag{4.5}$$

while

$$ds^{2,+} = -f(r)dt^2 + \frac{1}{f(r)}dr^2 + r^2(d\theta^2 + \sin^2\theta d\phi^2), \tag{4.6}$$

for $r \geq R$. In addition, we have $f(r) = 1 - 2M/r$, with M being the mass and R the radius of the shell. Clearly, this metric satisfies the first junction condition Eq. (4.1) since both $ds^{2,\pm}$ induces the metric $ds^2_\Sigma = -f(R)dt^2 + R^2(d\theta^2 + \sin^2\theta d\phi^2)$ on Σ. The second junction condition determines the stress-energy tensor of the shell. We will not make use of the stress-energy of the shell but we review it briefly in Appendix A.

Using this metric the massless scalar field Eq. (2.2) admits separable solutions of the form

$$\Phi_{\omega\ell m}(t, r, \theta, \phi) = \frac{1}{\sqrt{4\pi\omega}} e^{-i\omega t} Y_{m\ell}(\theta, \phi)\psi_{\omega\ell}(r)\,. \tag{4.7}$$

These modes are indexed by (ω, ℓ, m), with $\omega \in (0, \infty)$, $\ell \in \mathbb{Z}$ and $m = -\ell, -\ell+1, ..., \ell-1, \ell$. The functions $Y_{m\ell}$ are the spherical harmonics normalized as

$$\int_{S^2} Y^*_{m_1\ell_1} Y_{m_2\ell_2} dA = \delta_{m_1,m_2}\delta_{\ell_1,\ell_2}\,.$$

Substituting the ansatz Eq. (4.7) into the field equation gives an ODE that $\psi_{\omega\ell}(r)$ needs to satisfy:

$$\omega^2\psi_{\omega\ell}(r) + \frac{\alpha}{\beta\, r^2}\frac{d}{dr}\left(\frac{\alpha r^2}{\beta}\frac{d}{dr}\psi_{\omega\ell}(r)\right) - \left(\frac{\alpha^2\ell(\ell+1)}{r^2}\right)\psi_{\omega\ell}(r) = 0, \tag{4.8}$$

where the functions $\alpha(r)$ and $\beta(r)$ are,

$$\alpha(r) = \begin{cases} \sqrt{f(R)}, & r \leq R \\ \sqrt{f(r)}, & r > R \end{cases},$$
$$\beta(r) = \begin{cases} 1, & r \leq R \\ 1/\sqrt{f(r)}, & r > R \,. \end{cases} \tag{4.9}$$

In other words, $\psi_{\omega\ell}(r)$ is governed by two different ODEs on either sides of the shell. Inside the shell the equation explicitly reads

$$\frac{\omega^2}{f(R)} r^2 \psi_{\omega\ell} + 2r \frac{d}{dr}\psi_{\omega\ell} + r^2 \frac{d^2}{dr^2}\psi_{\omega\ell} - \ell(\ell+1)\psi = 0, \tag{4.10}$$

whose solutions are spherical Bessel functions of the first kind, $j_\ell(\tilde{\omega} r)$, where $\tilde{\omega} = \frac{\omega}{\sqrt{f(R)}}$. Meanwhile, the equation outside the shell is more complicated and has to be determined numerically.

In order to find the numerical solution to the second order ODE, we impose the two boundary conditions (4.3) and (4.4) at $r = R$. The first of these, continuity of the radial solution, gives

$$\psi_{\omega\ell}(R^+) = j_\ell(\tilde{\omega} R).$$

Meanwhile the second condition gives

$$\left[\frac{\alpha(r)}{\beta(r)} \frac{d}{dr}\psi_{\omega\ell}\right] = 0\,, \tag{4.11}$$

where we note that the discontinuity in the coefficient $\beta(r)$ across the shell implies a jump discontinuity in $\frac{d}{dr}\psi_{\omega\ell}$. These two boundary conditions then uniquely determine the radial solution outside the shell for each $\{\omega, \ell\}$.

Finally, to normalize the solution, we will follow the scheme presented in [44]. First, the radial equation (4.8) for $r > R$ can be rewritten in terms of a new coordinate $r^\star$ such that $d/dr^\star = \frac{\alpha}{\beta} d/dr$. Further, defining $\rho_{\omega\ell} = r\psi_{\omega\ell}$, the radial equation takes the familiar form,

$$\frac{d^2}{dr^{\star 2}}\rho_{\omega\ell} + (\omega^2 - V(r))\rho_{\omega\ell} = 0\,, \tag{4.12}$$

where

$$V(r) = \frac{\alpha^2 \ell(\ell+1)}{r^2} + \frac{1}{r}\frac{\alpha}{\beta}\frac{d}{dr}\left(\frac{\alpha}{\beta}\right). \tag{4.13}$$

Asymptotically, $V(r) \to 0$ as $r \to \infty$ and hence $\psi_{\omega\ell} \sim \sin(\omega r^\star)/r^\star$. Next, let the normalized radial solution be written as $\psi_{\omega\ell}(r^\star) = A_{\omega\ell}\tilde{\psi}_{\omega\ell}(r^\star)$. The solution (4.7) will be normalized with respect to the Klein-Gordon inner product if we choose the normalization constant $A_{\omega\ell}$ such that $A_{\omega\ell}\tilde{\psi}_{\omega\ell}(r^\star) \to 2\sin(\omega r^\star)/r^\star$ as $r^\star \to \infty$ [44]. This fixes the boundary condition at infinity for the determination of $A_{\omega\ell}$.

We have thus determined the necessary mode solutions, from which the Wightman function of the field can be obtained. Note that the mode solution in the region $r < R$ differs from the Minkowski modes only through the normalization constant $A_{\omega\ell}$. This difference will allow a UDW detector placed inside the shell to detect the presence of the shell. We remind the reader that the normalization constant in the Minkowski case is 2ω, giving the full normalized solution, $\Phi^M_{\omega\ell m}(t, r, \theta, \phi) = \sqrt{\frac{\omega}{\pi}} e^{-i\omega t} Y_{m\ell}(\theta, \phi) j_\ell(\omega r)$ [44].

4.3 Response function

A classical observer feeling no gravitational field can find out if he is in empty space or in a large spherical shell by sending out a laser beam – a reflected signal will indicate the presence of a shell. Can a UDW detect the shell faster? We can answer this by choosing a compact switching function

$$\chi_c(\tau) = \begin{cases} \cos^4(\eta\tau), & -\frac{\pi}{2\eta} \leq \tau \leq \frac{\pi}{2\eta} \\ 0, & \text{otherwise} \end{cases} \tag{4.14}$$

Thus the interaction switches on and off continuously and takes place between the finite time interval $\tau \in (-\frac{\pi}{2\eta}, \frac{\pi}{2\eta})$ for some $\eta > 0$. We denote this duration as $\Delta\tau = \pi/\eta$. We have chosen this particular form of the switching because it has a shape similar to the Gaussian switching function χ_G used in [44] (see Fig. 4.2),

$$\chi_G(t) = e^{-\frac{t^2}{2\sigma^2}} . \tag{4.15}$$

However, χ_G has an infinite support, even though it is exponentially suppressed away from $t = 0$. As a result, one may suspect a detection of the shell as being a result of (never ending) signalling between the detector and the shell if χ_G were used. We shall see below that the UDW detector can detect the shell before a light signal can bounce from the shell back to the detector by using the compact χ_c.

Let $|0\rangle$ denote the field vacuum such that $\hat{a}_{\omega\ell m}|0\rangle = 0$, where the annhilation operators

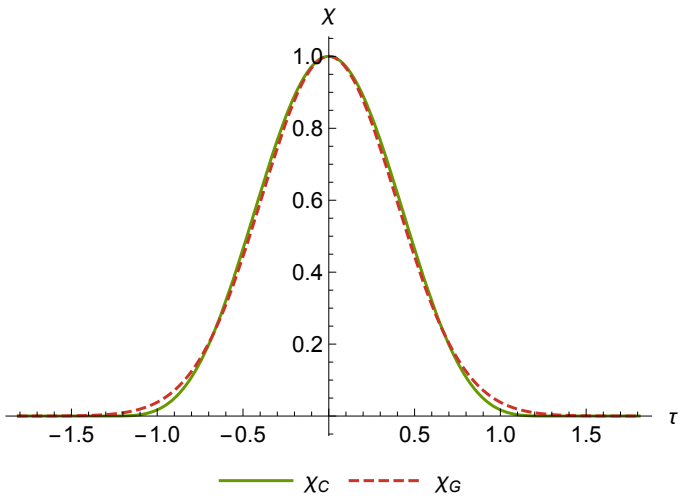

Figure 4.2: **Plot of Gaussian χ_G and χ_c switching.** Here, the parameters used are $\eta = 1.2$, $\sigma = \frac{3}{8\eta}\sqrt{\frac{\pi}{2}}$. These parameters give the same area under the graph for the two switching profiles. Although both look similar, χ_c is compactly supported. The interaction duration between the detector and the quantum field can thus be made truly shorter than the light-crossing time of the shell.

are associated with the mode solutions in Eq. (4.7)[1]. The Wightman function evaluated along the detector trajectory is given by the mode sum,

$$W(x(\tau_1); x(\tau_2)) = \sum_{\ell,m} \int_0^\infty d\omega \, \Phi_{\omega\ell m}(x(\tau_1)) \Phi^*_{\omega\ell m}(x(\tau_2)) \, . \tag{4.16}$$

From the previous section, we have seen that the normalized mode solutions are given by

$$\Phi_{\omega\ell m} = \frac{1}{\sqrt{4\pi\omega}} e^{-i\omega t} Y_{\ell m}(\theta, \phi) A_{\omega\ell} j_\ell(\tilde{\omega} r)$$

inside the shell.

We are interested in studying how the response of the detector differs when placed respectively in a spherical shell and globally flat Minkowski spacetime. A simple choice

[1]This corresponds to the vacuum with respect to an observer located at infinity. We note that this vacuum also corresponds to that of an inertial observer inside the shell, since the mode solutions in Eq. (4.7) are positive frequency with respect to the proper times of both these observers – the Bogoliubov transformation between the inside and outside modes does not mix creation and annihilation operators.

for the trajectory $x(\tau)$ of the detector that will allow us to do this is the static trajectory with $r = r_d$, $\theta = \pi/2$, $\phi = 0$. In this case, noting that $t = \tau/\sqrt{f(R)}$, we have

$$\begin{aligned}
\mathcal{F} &= \int_{-\infty}^{\infty} d\tau_1 \int_{-\infty}^{\infty} d\tau_2\, \chi_c(\tau_1)\chi_c(\tau_2) e^{-i\Omega(\tau_1-\tau_2)} \sum_{\ell m} \int_0^{\infty} d\omega \Phi_{\omega\ell m}(x(\tau_1))\Phi^*_{\omega\ell m}(x(\tau_2)) \\
&= \int_{-\infty}^{\infty} d\tau_1 \int_{-\infty}^{\infty} d\tau_2\, \chi_c(\tau_1)\chi_c(\tau_2) e^{-i\Omega(\tau_1-\tau_2)} \sum_{\ell m} \int_0^{\infty} \frac{d\omega}{4\pi\omega} e^{-i\tilde{\omega}(\tau_1-\tau_2)} |Y_{\ell m}(\frac{\pi}{2}, 0)|^2 |A_{\omega\ell}|^2 |j_\ell(\tilde{\omega}\, r_d)|^2 \\
&= \sum_{\ell m} \int_0^{\infty} \frac{d\omega}{4\pi\omega} \int_{-\infty}^{\infty} d\tau_1 \int_{-\infty}^{\infty} d\tau_2\, \chi_c(\tau_1)\chi_c(\tau_2) e^{-i(\Omega+\tilde{\omega})(\tau_1-\tau_2)} |Y_{\ell m}(\frac{\pi}{2}, 0)|^2 |A_{\omega\ell}|^2 |j_\ell(\tilde{\omega}\, r_d)|^2 \,,
\end{aligned} \tag{4.17}$$

for the response function of the detector. This expression can be further simplified by integrating over the τ_1 and τ_2 variables, which amounts to performing Fourier transforms on the switching functions. Denoting the Fourier transform of the switching function as

$$\hat{\chi}_c(k) = \frac{1}{\sqrt{2\pi}} \int_{-\infty}^{\infty} d\tau \chi_c(\tau) e^{-ik\tau} \,, \tag{4.18}$$

the response function (4.17) simplifies to

$$\mathcal{F} = \sum_{\ell m} \int_0^{\infty} \frac{d\omega}{2\omega} \left|\hat{\chi}_c\left(\Omega + \tilde{\omega}\right)\right|^2 |A_{\omega\ell}|^2 |Y_{\ell m}(\frac{\pi}{2}, 0)|^2 |j_\ell(\tilde{\omega} r_d)|^2 \,, \tag{4.19}$$

upon using the fact that $\hat{\chi}_c(-k) = \hat{\chi}_c(k)$ for a real switching function. Explicitly, we have

$$\hat{\chi}_c(k) = \sqrt{\frac{2}{\pi}} \frac{24\eta^4 \sin\frac{\pi k}{2\eta}}{64\eta^4 k - 20\eta^2 k^3 + k^5} \,. \tag{4.20}$$

4.4 Results

Let us now look at how the presence of the shell affects the response of a UdW detector. We will use $\mathcal{F}_S$ to denote the response of a detector placed in a spherical shell, and $\mathcal{F}_M$ to denote its response in global Minkowski space.

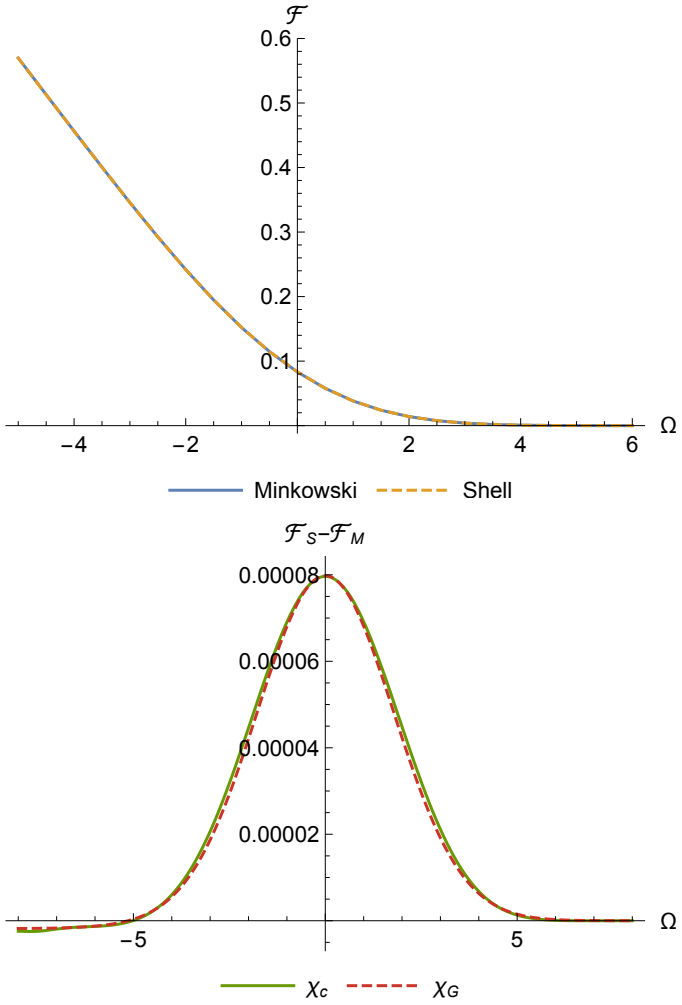

Figure 4.3: **Detector response against** Ω**.** *Top:* Plot of $\mathcal{F}$ against Ω for both the shell (yellow) and globally flat Minkowksi spacetime (blue) for $M = 0.5$, $R = 3\,, \eta = 1.2$, $r_d = 0$. The two cases are indistinguishable on the scale of this figure, but the differences can be studied by looking at the bottom figure. *Below:* Plot of the difference $\mathcal{F}_S - \mathcal{F}_M$ against Ω. The results obtained using χ_c and χ_G ($\sigma = \frac{3}{8\eta}\sqrt{\frac{\pi}{2}}$) are qualitatively similar.

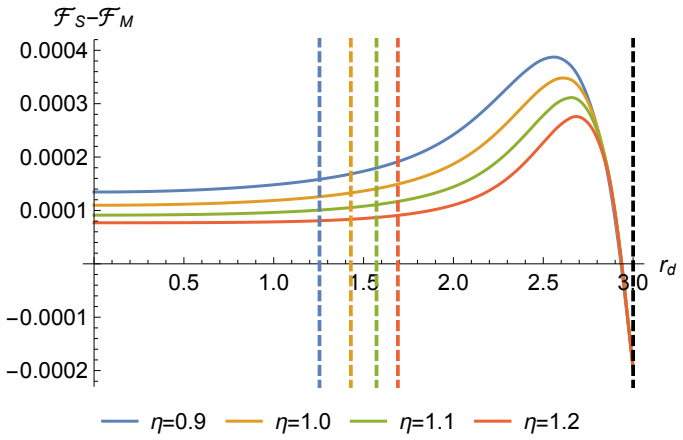

Figure 4.4: **Plot of $\mathcal{F}_S - \mathcal{F}_M$ against r_d.** This plot is obtained by setting $\Omega = 0.5\,, M = 0.5$, $R = 3$ (black, dashed) and $\eta = 0.9$, 1, 1.1, 1.2. The peaks indicate the optimal r_d inside the shell at which the detector, for a given η, can best detect the presence of the shell. The vertical dashed lines indicate, for a given η, the causal boundary of the interaction duration: to the left of these lines this duration is less than the light-travel time across the shell.

Dependence on Ω

Fig. 4.3 shows a plot of $\mathcal{F}$ against Ω. In the figure, Ω is allowed to take on negative values. Recall from the previous chapter that this represents a detector starting from the state $|1\rangle_D$ with $\mathcal{F}$ indicating de-excitation probability. From the figure, we see that the detector is indeed sensitive to the presence of the shell. This is most apparent when we plot the difference $\mathcal{F}_S - \mathcal{F}_M$. We have chosen the parameter η such that interaction duration $\Delta\tau \approx 2.6$ between the field and detector is less than $2R = 6$, the time needed for a light signal to travel from the detector at the center to the shell and back. This is in contrast to the classical case, where the fastest way a detector inside the shell can detect its presence is by sending and waiting for a light signal to come back from the shell. We thus ~~strengthen the claim made in [44].~~ conclude that a UdW detector interacting with the quantum vacuum can detect the shell faster than a classical detector even if its interaction time is causally disconnected from the shell, a result already established in [44] using Gaussian switching.

Dependence on r_d

We next consider the response of the detector as we vary its location r_d within the shell. Fig. 4.4 shows a plot of $\mathcal{F}_S - \mathcal{F}_M$ against r_d with $\Omega = 0.5$ and various choices of the interaction duration $\Delta\tau$. For each η, as r_d increases, the difference in response first decreases very slightly, before increasing to a peak lying between the left and right dashed lines in the figure. This can be interpreted as the existence of an optimal position at which the UdW detector can best detect the presence of the shell. However, at this position, the detector is switched on for a time longer than the light-crossing time. The largest r_d beyond which this happens is indicated by the vertical dashed lines for each η.

Numerical convergence

We close this section by commenting on the stability of our results, which were computed by evaluating expression (4.19) numerically. In doing so, we have chosen upper cut-offs for the summation over ℓ and for the integral over ω. Both the integral and summation exhibit clear numerical convergence, as shown in Fig. 4.5, with

$$S_L = \sum_{\ell=0}^{L} \sum_{m=-\ell}^{\ell} \mathcal{I}_{\ell m}\,, \tag{4.21}$$

$$\mathcal{I}_{\ell m} = \int_0^b \frac{d\omega}{2\omega} \left|\hat{\chi}_c\left(\Omega + \tilde{\omega}\right)\right|^2 |A_{\omega\ell}|^2 |Y_{\ell m}(\frac{\pi}{2}, 0)|^2 |j_\ell(\tilde{\omega} r_d)|^2\,. \tag{4.22}$$

For the results presented in this chapter, we have chosen the cut-offs L and b such that the contribution of the next term in the summation or the next integral interval is less than 10^{-7}.

4.5 Summary

In this chapter, we have built on the work done in [44], confirming again the result that a UdW detector that is causally disconnected from the external environment of the shell can still detect its presence relative to globally flat spacetime. In so doing we have demonstrated a 'quantum detection of local frame' phenomenon, in which non-local information about the global structure of spacetime contained in the vacuum state of a quantum field can be read locally by a detector.

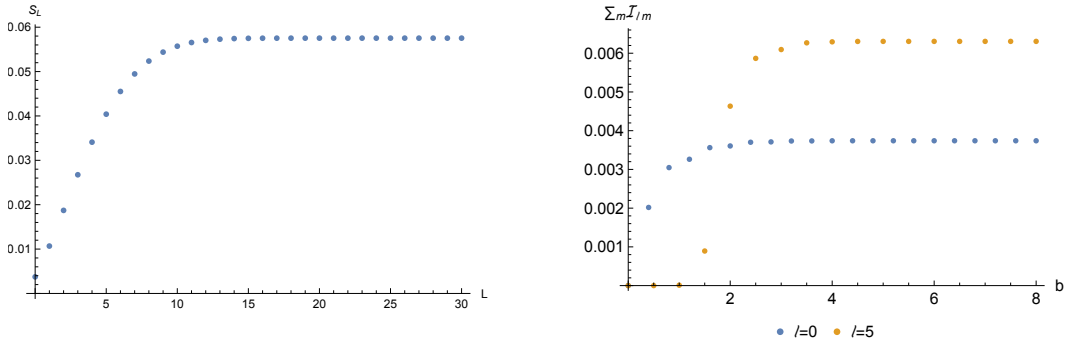

Figure 4.5: **Numerical convergence.** In evaluating (4.19) numerically, an upper cut-off for the sum in ℓ has to be chosen. *Left:* Plot of the partial sum $\mathcal{S}_L$ against L. We see that the summation over ℓ is clearly convergent. The parameters used here are the same as those in Fig. 4.4, with $r_d = 3$. *Right:* Plot of $\sum_m \mathcal{I}_{\ell m}$ against the upper cut-off b. For each ℓ (two examples are shown here), the integral over ω is also clearly convergent.

We carried the investigation further than that in [44] and shown that the detector can be placed within the shell in different locations to optimally distinguish the local/global cases; however this optimal placement is not causally disconnected from the shell boundary.

We note that, although our work was carried out in the context of general relativity, its implications are considerably broader. The $A_{\omega\ell}$ quantities depend on the form of the effective potential (4.13), and thus upon the theory of gravity that governs the dynamics of spacetime. In this sense a UdW detector is a non-local probe of the local dynamics of gravity outside of the shell. A more complete study of this would be an interesting subject for future investigation. We can likewise ask if a detector could be used to discern other effects, such as the dragging of inertial frames. We shall do this in the next chapter.

Chapter 5

Detection of Inertial Frame Dragging

5.1 Inertial frame dragging

Frame-dragging, also known as the Lense–Thirring effect [61, 62], is a general-relativistic effect that arises due to moving, in particular rotating, matter [63] and "rotating" gravitational waves [64, 65]. If a gyroscope is located in the vicinity of a rotating body, it will keep its direction with respect to the axes of a local inertial frame at the same place but both the inertial axes and the gyroscope will be rotating with respect to static distant observers ("fixed stars" at asymptotically flat infinity). Its profound explicit manifestation can be seen for a rotating black hole, which drags particles into co-rotation, the dragging becoming so strong inside the ergosphere that no particle there can remain at rest with respect to fixed stars [66]. Frame-dragging is also behind various astrophysical phenomena such as relativistic jets and the Bardeen-Petterson effect [67], which aligns accretion disks perpendicular to the axis of a rotating black hole.

In addition, frame-dragging *inside* a rotating shell was taken by Einstein to be in support of Mach's principle. For a nice discussion on Mach's principle, dragging effects and their impact on astrophysics and cosmology, see [68] (also [69, 63]). Consider a slowly rotating material shell [70, 71]. Observers inside the shell who are at rest with respect to distant fixed stars will find that a particle moving inside the shell experiences a Coriolis acceleration (the centrifugal acceleration is of the second order in the shell's angular velocity). These observers are *not inertial*, therefore fictitious forces arise.

For *inertial observers*, without looking at or outside the rotating shell, there is no way of determining, by employing classical physics, whether they are surrounded by a rotating

shell. They can in principle determine its rotation by, for example, sending out a spherical pulse which, upon reflection, will experience a differential Doppler effect, with different shell latitudes Doppler shifting differently. Meanwhile, frame-dragging *outside* a rotating body, the Earth, has taken the Gravity Probe B satellite mission [45, 72] almost a half-century since its inception to detect.

In this chapter, we will show that frame-dragging inside a slowly rotating shell can be observed by an inertial UDW detector. Moreover, as in the previous chapter, it can do so in a time shorter than the light crossing time of the shell. The transition from the previous chapter to the current one is much like the transition from electrostatics to electromagnetism, or the transition from Schwarzchild to Kerr; it demonstrates that a fundamentally relativistic (non-Newtonian) effect of dragging of inertial frames, namely the existence of gravitomagnetism, can in principle be observed by a quantum detector in settings that are not classically possible.

This chapter is based on [2].

5.2 Scalar field modes

5.2.1 Metric

We begin as before by describing the spacetime metric, this time of a slowly rotating shell. The metric outside the shell can be written as

$$ds^{2,+} = -f(r)dt^2 + r^2\sin^2\theta(d\phi - \frac{2Ma}{r^3}dt)^2 + f(r)^{-1}dr^2 + r^2d\theta^2\,, \tag{5.1}$$

where $f(r) = 1-2M/r$, M is the mass of the shell and $a = J/M$ is the angular momentum per unit mass. The r-coordinate ranges from $[R, \infty)$, R being the radius of the shell. To first order in a, the above metric agrees with the Kerr metric and satisfies the vacuum Einstein's equations.

Inertial frame-dragging is characterized by the function $\varpi(r) = g_{\phi t}/g_{\phi\phi} = 2J/r^3$, where $J = Ma$ is the fixed total angular momentum as measured at infinity. The gradients of $\varpi(r)$ determine the precession of gyroscopes relative to the orthonormal frame of locally non-rotating observers [66]. On the shell itself, $r = R$, and $\varpi_s = 2J/R^3$.

For an inertial observer inside the shell (who rotates as seen from infinity) spacelike geodesics (for example, $\phi = 0, \theta = \pi/2, r = \text{constant}, t \in \mathbb{R}$) connected to fixed points at infinity rotate backwards; the shell is rotating forward (the dragging of the inertial frame

becomes complete i.e., inertial observers rotate at the same angular velocity as the shell, only if the shell is at its Schwarzschild radius); the fixed stars are rotating backwards. In [73] these effects are expressed quantitatively[1].

The metric (5.1) is joined at Σ, given by $r = R$, to the metric

$$ds^{2,-} = -f(R)dt^2 + r^2 \sin^2\theta \left(d\phi - \frac{2Ma}{R^3}dt\right)^2 + dr^2 + r^2 d\theta^2 \,, \tag{5.2}$$

where now $r \in [0, R]$. It is easy to see that the first junction condition is satisfied since both $ds^{2,\pm}$ induce the same intrinsic metric on Σ. In the coordinates (t, θ, ϕ), this is,

$$ds^2_\Sigma = -f(R)dt^2 + R^2 \sin^2\theta \left(d\phi - \frac{2Ma}{R^3}dt\right)^2 + R^2 d\theta^2 \,. \tag{5.3}$$

The stress energy tensor of the shell giving rise to this spacetime can be found using the second junction condition and has been well-studied in the literature (see, e.g., [60]). We review the results briefly in Appendix A.

The metric (5.2) inside the shell is flat – consider the coordinate transformation,

$$\varphi = \phi - \frac{2Ma}{R^3}t \,. \tag{5.4}$$

This transforms the metric (5.2) to the flat metric in standard coordinates

$$ds^2_\Sigma = -f(R)dt^2 + dr^2 + r^2(d\theta^2 + \sin^2\theta d\varphi^2) \,. \tag{5.5}$$

The coordinates used in Eq. (5.1) are (spherical) Lorentzian at infinity and are naturally associated with stationary observers at infinity. All observers at fixed (r, θ, φ) inside the shell rotate rigidly at the rate $d\phi/dt = 2Ma/R^3$ with respect to observers at rest at infinity (ϕ =constant). This effect is called the dragging of inertial frames, first discovered in 1918 by Thirring and Lense [61] as discussed in the introduction of this chapter.

5.2.2 Normalized mode solutions

To leading order in a, we can employ the same form of mode expansion as that in the previous chapter for the scalar field,

$$\Phi_{\omega\ell m}(t, r, \theta, \phi) = \frac{1}{\sqrt{4\pi\omega}} e^{-i\omega t} Y_{m\ell}(\theta, \phi)\psi(r) \,. \tag{5.6}$$

[1] In [73] the shell is in general considered to be collapsing but the results can be immediately specialized if it is just rotating.

As before, the modes are indexed by (ω, ℓ, m), with $\omega > 0$, $\ell \in \mathbb{Z}$ and $m = -\ell, -\ell+1, ...\ell$. However, the radial equation for $\psi(r)$ now takes a more complicated form. For each (ω, ℓ, m), it reads,

$$\frac{\alpha}{\beta\, r^2}\frac{d}{dr}\Big(\frac{\alpha}{\beta} r^2 \frac{d\psi}{dr}\Big) - \left(\frac{\alpha^2 \ell(\ell+1)}{r^2} + \gamma + \omega^2\right)\psi = 0\,. \tag{5.7}$$

The functions α, β and γ are

$$\begin{aligned}
\alpha(r) &= \begin{cases} \sqrt{f(R)}, & r \le R, \\ \sqrt{f(r)}, & r > R, \end{cases} \\
\beta(r) &= \begin{cases} 1, & r \le R \\ 1/\sqrt{f(r)}, & r > R, \end{cases} \\
\gamma(r) &= \begin{cases} \frac{4Mam\omega}{R^3} - \left(\frac{2Mam}{R^3}\right)^2, & r \le R, \\ \frac{4Mam\omega}{r^3} - \left(\frac{2Mam}{r^3}\right)^2, & r > R\,, \end{cases}
\end{aligned} \tag{5.8}$$

which reduces to eq. (4.9) of the previous chapter upon setting $a = 0$.

For $r \le R$, the radial equation reduces to the spherical Bessel equation, with the solution being

$$\psi(r) = j_\ell(\sqrt{b(\omega)}r)\,, \quad b(\omega) = \frac{\omega^2}{f(R)}\Big(1 - \frac{2Mam}{R^3\omega}\Big)^2\,. \tag{5.9}$$

The solution outside the shell has to be determined numerically and matched to the solution on the shell. The two boundary conditions on $\psi(r)$ at the shell are:

$$\psi(R) = j_\ell(\sqrt{b(\omega)}R)\,, \tag{5.10}$$

$$\left[\frac{\alpha(r)}{\beta(r)}\frac{d}{dr}\psi\right] = 0\,. \tag{5.11}$$

Noting from (5.8) the discontinuity in $\beta(r)$, this yields the required initial conditions $\psi(R^+)$ and $\psi'(R^+)$ for numerically solving the radial equation outside the shell.

Finally, we have to normalize the solution. The approach follows that of the previous chapter. Defining $r^\star$ such that $d/dr^\star = \frac{\alpha}{\beta} d/dr$ and $\rho = r\psi$, the radial equation (5.7) reads

$$\frac{d^2}{dr^{\star 2}}\rho + (\omega^2 - V(r))\rho = 0\,, \tag{5.12}$$

for $r > R$, where

$$V(r) = \frac{\alpha^2 \ell(\ell+1)}{r^2} + \gamma + \frac{1}{r}\frac{\alpha}{\beta}\frac{d}{dr}\left(\frac{\alpha}{\beta}\right). \tag{5.13}$$

Once again, we have $V(r) \to 0$ as $r \to \infty$ and hence $\psi \sim \sin(\omega r^\star)/r^\star$. Let the normalized radial solution be denoted as $\tilde{\psi}_{\omega\ell m}(r^\star) = A_{\omega\ell m}\psi(r^\star)$ where, unlike the non-rotating case, now the normalization constant depends on the azimuthal number m. A solution will be normalized with respect to the Klein-Gordon inner product if we choose the normalization constant $A_{\omega\ell m}$ such that $A_{\omega\ell m}\psi(r^*) \to 2\sin(\omega r^\star)/r^\star$ as $r^\star \to \infty$ [44].

In summary, the normalized mode solution inside the shell is,

$$\Phi_{\omega\ell m} = \frac{1}{\sqrt{4\pi\omega}} e^{-i\omega t} Y_{m\ell}(\theta,\phi) A_{\omega\ell m} j_\ell(\sqrt{b(\omega)}r)\,. \tag{5.14}$$

We will use this for the computation of the response function of a UDW detector placed inside a slowly rotating shell in the next section.

5.3 Response function

Let us now consider an inertial UDW detector situated at $r = r_d < R$, $\theta = \pi/2$, $\varphi = 0$ i.e., $\phi = \frac{2Ma}{R^3}t$. Noting that $t = \tau/h$, where $h = \sqrt{f(R)}$, we can compute the response function of the detector to be,

$$\begin{aligned}
\mathcal{F} &= \int_{-\infty}^{\infty} d\tau_1 \int_{-\infty}^{\infty} d\tau_2\, \chi_c(\tau_1)\chi_c(\tau_2) e^{-i\Omega(\tau_1-\tau_2)} \sum_{\ell m} \int_0^\infty d\omega \Phi_{\omega\ell m}(x(\tau_1))\Phi^*_{\omega\ell m}(x(\tau_2)) \\
&= \sum_{\ell m} \int_0^\infty \frac{d\omega}{4\pi\omega} \int_{-\infty}^{\infty} d\tau_1 \int_{-\infty}^{\infty} d\tau_2\, \chi_c(\tau_1)\chi_c(\tau_2) e^{-i(\Omega+\frac{\omega}{h}-\frac{2Mam}{R^3 h})(\tau_1-\tau_2)} |Y_{\ell m}(\frac{\pi}{2},0)|^2 \qquad (5.15) \\
&\quad \times |A_{\omega\ell m}|^2 |j_\ell(\sqrt{b(\omega)}\, r_d)|^2 \\
&= \sum_{\ell m} \int_0^\infty \frac{d\omega}{2\omega} \left|\hat{\chi}_c\left(\Omega + \frac{\omega}{h} - \frac{2Mam}{R^3 h}\right)\right|^2 |A_{\omega\ell m}|^2 |Y_{\ell m}(\frac{\pi}{2},0)|^2 |j_\ell(\sqrt{b(\omega)} r_d)|^2\,. \qquad (5.16)
\end{aligned}$$

The rotation parameter a enters the response function $\mathcal{F}$ in three positions above: in the Fourier transform of the switching function, in the normalization constant $A_{\omega\ell m}$, and in the $b(\omega)$ of the spherical Bessel function. Denoting the detector response in the static and rotating case as $\mathcal{F}_{stat}$ and $\mathcal{F}_{rot}$ respectively, we shall see that the net effect of these dependence is an increase in $|\mathcal{F}_{rot} - \mathcal{F}_{stat}|$ with a.

We pause to comment that even though the metric (5.1) is a valid solution of the Einstein equations only to first order in a, we have computed the modes (5.6) from the radial equation (5.7) exactly (i.e., to all orders in a). This is because the Wightman function is an even function[2] in a and the leading corrections to it are of order a^2. For sufficiently small Ma/R^2, terms of order above $O(a^2)$ will not significantly affect our quantitative results, and so we work with (5.16) in what follows.

5.4 Results

We are now ready to look at how rotation of the shell affects the response of UDW detectors. We do this by computing the expression (5.16) numerically, terminating the sum over ℓ at sufficiently large ℓ, chosen to give resultant errors not larger than 1%.

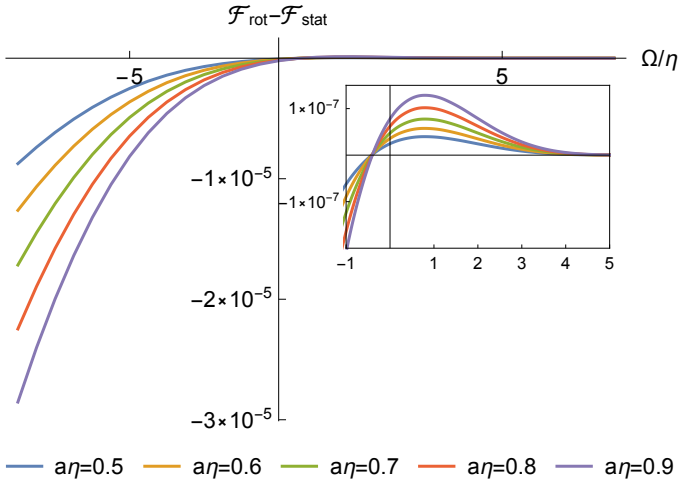

Figure 5.1: Detector response against Ω/η. Shown here is the plot of the difference $\mathcal{F}_{rot} - \mathcal{F}_{stat}$ against Ω/η for different (dimensionless) rotation parameters $a\eta$ with $M\eta = 1$, $R\eta = 3$, $r_d\eta = 0.5$. The inset shows a zoom-in of the plot around $\Omega/\eta = 0$. The difference $\mathcal{F}_{rot} - \mathcal{F}_{stat}$ is small but non-zero, and is more sensitive to the rotation for negative Ω.

[2]Intuitively, the Wightman function is an even function in a as it is neutral to the direction of rotation. We can also see this explicitly by noting that a and m always appear together in the radial equation (5.7) as ma. Thus as a function of a, the Wightman function is of the form $W(a) = \sum_{\omega\ell}\sum_{m=-\ell}^{\ell} g(ma) = \sum_{\omega\ell}\sum_{m=\ell}^{-\ell} g((-m)a) = \sum_{\omega\ell}\sum_{m=\ell}^{-\ell} g(m(-a)) = W(-a)$

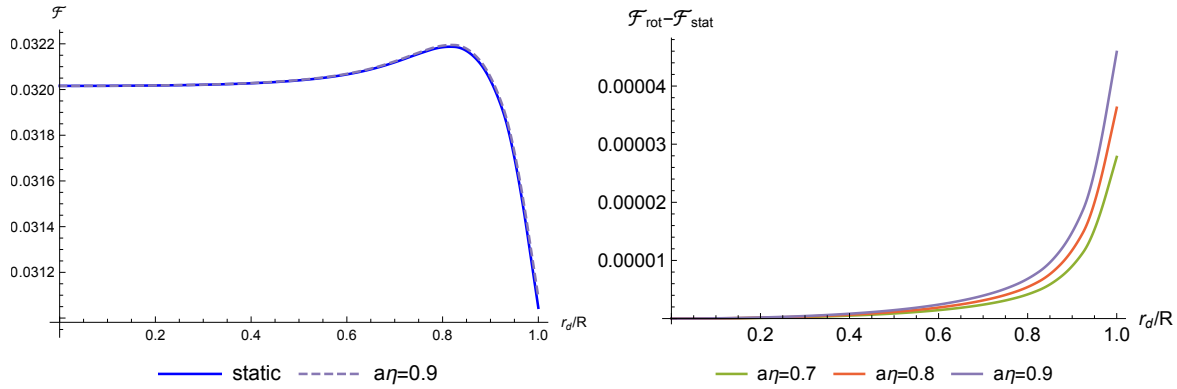

Figure 5.2: Dependence on radial distance r_d/R. These plots are obtained for $M\eta = 1$, and $R\eta = 3$. **Left:** Plot of detector response against r_d/R for static and rotating ($a\eta = 0.9$) shells, $\Omega/\eta = 0.5$. **Right:** $\mathcal{F}_{rot} - \mathcal{F}_{stat}$ plots for different $a\eta$ settings with $\Omega/\eta = 0.5$.

Dependence on a

Fig. 5.1 shows a plot of $\mathcal{F}_{rot} - \mathcal{F}_{stat}$ (refer to fig.4.3 for the response of a detector in a static shell) against Ω/η for various (dimensionless) rotation parameters $a\eta$. The difference between the response of a detector placed in a slowly rotating shell and that placed in a static shell, though small, is clearly *non-zero*. The difference is more pronounced when the energy gap $\Omega/\eta < 0$.

We emphasize that the interaction duration $\Delta\tau\,\eta = \pi$ between the field and detector is less than $2(R - r_d)\eta = 5$, the time needed for a light signal to travel from the detector to the shell and back. This is in striking contrast to the classical case, where the fastest way a detector inside the shell (with all possible classical fields in their vacuum states) can detect the presence of rotation is by sending and waiting for a light signal to come back from the shell.

Dependence on r_d and θ

Next, let us study the effect of moving the detector radially outwards by looking at Fig. 5.2. The three main observations from this are:

i. from the left figure (plot of $\mathcal{F}_{rot}(a\eta = 0.9)$ and $\mathcal{F}_{stat}$ against r_d/R) we see that the responses peak at some intermediate r_d, in agreement with the results of fig. 4.4 from the previous chapter,

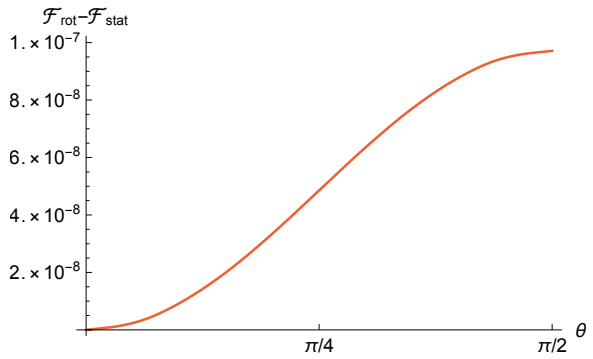

Figure 5.3: Plot of $\mathcal{F}_{rot} - \mathcal{F}_{stat}$ against θ for $M\eta = 1$, $R\eta = 3$, $a\eta = 0.8$ and $r_d\eta = 0.5$.

ii. from the right figure, we see that as as $r_d/R \to 1$, the difference in response increases by more than an order of magnitude as compared to the small r_d scenario in Fig. 5.1. Hence, a detector can be made more sensitive to the rotation as r_d/R increases, though the interaction duration will eventually exceed the light crossing time,

iii. a detector placed at the origin $r_d = 0$ cannot distinguish between a rotating and a static shell since $\mathcal{F}_{rot} - \mathcal{F}_{stat} = 0$ there.

We can understand the last point explicitly by noting that the rotation parameter a appears in the radial equation (5.7) through the term γ, where it is multiplied with the azimuthal number m. Hence, it has only nontrivial effects when $m \neq 0$. However since $\theta = 0$ along the axis of rotation and $Y_{\ell m}(0, 0)$ is non-zero only when $m = 0$, the mode solutions and hence the response function are insensitive to effects of rotation along this axis. As another illustration of this, we plot in Fig. 5.3 $\mathcal{F}_{rot} - \mathcal{F}_{stat}$ against θ. From this, we see that the sensitivity to rotation of detectors placed at the same r_d increases monotonically as θ increases from 0 to $\pi/2$.

5.5 Summary

Classically, the physical effect of a slowly rotating shell is the dragging of inertial frames. We have shown that this effect can be discerned from local measurements of a quantum particle detector inside the shell, on timescales much shorter than the light travel time from the detector to the edge of the shell and back.

We note that the gravitational effects inside a rotating material shell are analogous to the electromagnetic effects inside a rotating charged shell; but there are also fundamental

differences. For a rotating charged shell, a dipolar magnetic field will be formed inside. Such a field can be observed without the need of quantum detectors, for example as the Larmor precession of charged particles.

By solving the scalar field equation numerically, we have obtained the response function of the detector and seen how it depends on the rotation parameter a. Corrections to the metric (5.1) to higher orders in a will quantitatively modify (5.16) but will not qualitatively affect our results. Alternatively, we can regard (5.1) as a 'kinematic spacetime' that could be employed in analogue gravity laboratory simulations, in which case our results would hold exactly. Whether or not such effects can be directly detected remains a challenge for future experiments.

Chapter 6

Detection of Conical Deficit

6.1 Conical deficits

In this chapter, we will focus on quantum detection of spacetime conicity. Specifically, we are interested in studying the sensitivity of a UDW detector to the global features of a deficit angle when its quasilocal manifestation is absent. We do this by placing the detector inside an infinite thin hollow cylinder (cylindrical shell), described by a special case of the Levi-Civita metric [74], whose spacetime is flat everywhere (except at the shell itself), but has a deficit angle *outside* the cylinder. Being induced by the energy-momentum of the cylinder, the deficit angle is *not present inside* the cylinder (where the detector is situated) and the axis is regular. This is in contrast to the usual idealized (distributional) cosmic string spacetime [75, 76], where the conical deficit is present throughout[1]. The absence of a deficit angle inside the cylinder provides an interesting set-up to study the response of a UDW detector since an observer with access only to classical measuring devices in a finite-sized quasilocal region within the cylinder could not detect its presence.

The effects of a "global conical deficit" on the vacua of quantum fields have been studied in the literature, such as the vacuum polarisation of the field [82, 83, 84] and particle creation in these spacetimes [85, 86]. UDW detectors and other quantum particles in cosmic string spacetimes have also been studied in the literature and it has been demonstrated that the detectors or particles are in general sensitive to the presence of a cosmic string

[1]The distributional cosmic string spacetime [77] is recovered upon the limit of the vanishing radius of the cylinder. More elaborate models of cosmic strings where the distributional character is smoothed out include, for example, constant density models [78], the abelian Higgs model [79, 80], or the recent model [81], which takes into account a non-local description of the gravitomagnetism.

[87, 88, 89, 90, 91, 92, 93, 94]. Contrary to all these studies, in our setup the UDW detector is not situated in the region with the conical deficit and such a deficit is only present outside the cylinder.

This chapter is based on [3].

6.2 Scalar field modes

6.2.1 Cylinder spacetime

Just as spherically symmetric massive shells are sources for the Schwarzschild spacetime, cylinders are sources for the Levi-Civita metric. However, constructing physical cylinders and relating their properties (such as mass) to the parameters of the Levi-Civita metric is more involved than in the spherical case, see, e.g., [95, 96, 97]. As before, we will not be using the stress-energy tensor of the cylindrical shell and hence we only briefly recall its form in Appendix B.

The specific metric we shall employ is a specific case studied by Bičák and Žofka in [95] where the mass parameter has been set to zero, giving a flat exterior with conical deficit. Inside the cylinder we have the usual Minkowski spacetime, with the metric written in cylindrical coordinates (t, z, ρ_-, ϕ) as:

$$ds^{2,-} = -dt^2 + dz^2 + d\rho_-^2 + \rho_-^2 d\phi^2\,, \quad 0 \leq \rho_- \leq R_1 \tag{6.1}$$

The surface Σ given by $\rho_- = R_1 \in \mathbb{R}^+$ is where joining to the exterior metric takes place. This exterior metric is given in terms of a new radial coordinate ρ_+ by,

$$ds^{2,+} = -dt^2 + dz^2 + d\rho_+^2 + \frac{\rho_+^2}{c^2} d\phi^2\,, \quad cR_1 \leq \rho_+ < cR_2\,, \tag{6.2}$$

where $c \geq 1$ is the conicity (see below). In these coordinates, the surface Σ is $\rho_+ = cR_1$. Using (t, z, ϕ) as our coordinates on Σ, we see that both $ds^{2,\pm}$ induces the metric,

$$ds^2|_\Sigma = -dt^2 + dz^2 + R_1^2 d\phi^2\,, \tag{6.3}$$

on Σ and thus the first junction condition is satisfied. The overall spacetime describes a cylinder of proper radius R_1.

The parameter c in Eq. (6.2) describes the "conicity" of the spacetime [95, 97]. Specifically, we can define a new angular coordinate $\varphi = \phi/c$, for which the metric in (6.2) reduces

to the usual Minkowski metric in cylindrical coordinates (i.e., of the form (6.1)) but with $\varphi \in [0, 2\pi/c]$. In other words, the spacetime described by (6.2) has a conical deficit of $\delta = 2\pi(1 - 1/c)$, which is greater than zero provided $c > 1$. We shall restrict attention to this case. The conical deficit gives rise to a non-zero mass per unit length of the cylinder μ given by,

$$\mu = \frac{1}{4}\Big(1 - \frac{1}{c}\Big)\,, \tag{6.4}$$

which is obtained from the second junction condition at Σ.

In order to avoid dealing with asymptotics of infinite cylindrical systems, in what follows we will impose Dirichlet boundary conditions for the scalar field on the surface $\rho_+ = cR_2$. This can be interpreted as a second infinitely long, perfectly reflecting cylinder, concentric to the first and having a proper radius of R_2 (see also [98]). We will not concern ourselves with the metric outside this second cylinder as the Dirichlet boundary condition ensures that the field will not respond to this part of the spacetime.

6.2.2 Scalar field modes

The massless scalar field equation in the above spacetime admits the mode decomposition:

$$\Phi_{kmq} = N_{kmq} e^{-i\omega t} e^{ikz} e^{im\phi} \psi_{mq}(\rho_\pm), \tag{6.5}$$

with $\omega^2 \equiv q^2 + k^2$ and N_{kmq} a normalisation constant. Inside the cylinder, $\rho_- < R_1$, substituting this ansatz into the wave equation (2.2) leads to a radial ODE governing $\psi_{mq}(\rho_-)$. This is given by,

$$\Big(q^2 - \frac{m^2}{\rho_-^2}\Big)\psi_{mq}(\rho_-) + \frac{\psi'_{mq}(\rho_-)}{\rho_-} + \psi''_{mq}(\rho_-) = 0\,, \tag{6.6}$$

which admits the general solution

$$\psi_{mq}(\rho_-) = a_1 J_{|m|}(q\rho_-) + a_2 Y_{|m|}(q\rho_-), \tag{6.7}$$

where J_m and Y_m are the Bessel functions of the first and second kind, respectively. To impose regularity at $\rho_- = 0$, we set $a_2 = 0$, and to impose periodicity in ϕ, we have $m \in \mathbb{Z}$. We can take $a_1 = 1$ without loss of generality by absorbing it into the normalisation constant N_{kmq}.

Meanwhile, the radial equation outside the cylinder reads:

$$\Big(q^2 - \frac{c^2 m^2}{\rho_+^2}\Big)\psi_{mq}(\rho_+) + \frac{\psi'_{mq}(\rho_+)}{\rho_+} + \psi''_{mq}(\rho_+) = 0\,. \tag{6.8}$$

This admits the general solution

$$\psi_{mq}(\rho_+) = c_1 J_{|cm|}(q\rho_+) + c_2 Y_{|cm|}(q\rho_+)\,. \tag{6.9}$$

The arbitrary constants c_1 and c_2 are determined by the continuity of ψ_{mq} and its derivative on the cylinder:

$$\psi_{mq}(\rho_- = R_1) = \psi_{mq}(\rho_+ = cR_1)\,, \tag{6.10}$$

$$\partial_{\rho_-}\psi_{mq}(\rho_- = R_1) = \partial_{\rho_+}\psi_{mq}(\rho_+ = cR_1)\,, \tag{6.11}$$

which follows from the conditions (4.3) and (4.4) with $n^+ = \partial_{\rho^+}$ and $n^- = \partial_{\rho^-}$. Substituting the general solutions (6.7) and (6.7) gives

$$\begin{aligned} c_1(q) &= \frac{1}{2}\pi qcR_1\Big(J_{|m|}(qR_1)Y_{|cm|-1}(qcR_1) - J_{|m|-1}(qR_1)Y_{|cm|}(qcR_1)\Big)\,, \\ c_2(q) &= \frac{1}{2}\pi qcR_1\Big(J_{|m|-1}(qR_1)J_{|cm|}(qcR_1) - J_{|m|}(qR_1)J_{|cm|-1}(qcR_1)\Big)\,. \end{aligned} \tag{6.12}$$

Next, to impose the Dirichlet boundary condition at $\rho^+ = cR_2$, we restrict the radial quantum number q to the discrete set $\{q : \psi_{mq}(\rho_+ = cR_2) = 0\}$ for each m.

Finally, the N_{kmq}'s are chosen such that the solutions are normalised with respect to the Klein-Gordon (KG) inner product. Let us choose a constant t surface to evaluate the inner product. This gives,

$$\begin{aligned} (\Phi_{kmq}, \Phi_{k'm'q'}) &= i\int dA\,(\Phi^*_{kmq}\partial_t\Phi_{k'm'q'} - \partial_t(\Phi^*_{kmq})\Phi_{kmq}) \\ &= iN_{kmq}N_{k'm'q'}\int dA\,(-i\omega' - i\omega)e^{-i(\omega'-\omega)t}e^{i(k'-k)z}e^{i(m'-m)\phi}\psi_{qm}\psi_{q'm'} \\ &= N_{kmq}N_{k'm'q'}(\omega'+\omega)e^{-i(\omega'-\omega)t}\int_{-\infty}^{\infty}dz\,e^{i(k'-k)z}\int_0^{2\pi}d\phi\,e^{i(m'-m)\phi}\times \\ &\Big(\int_0^{R_1}\big(\rho_- d\rho_-\,\psi_{qm}(\rho_-)\psi_{q'm'}(\rho_-)\big) + \int_{cR_1}^{cR_2}\big(\frac{\rho_+}{c}d\rho_+\,\psi_{qm}(\rho_+)\psi_{q'm'}(\rho_+)\big)\Big) \\ &= N_{kmq}N_{k'm'q'}(\omega+\omega')e^{-i(\omega'-\omega)t}\,2\pi\delta(k-k')\,2\pi\delta_{mm'}\times \\ &\Big(\int_0^{R_1}\big(\rho_- d\rho_-\,\psi_{qm}(\rho_-)\psi_{q'm'}(\rho_-)\big) + \int_{cR_1}^{cR_2}\big(\frac{\rho_+}{c}d\rho_+\,\psi_{qm}(\rho_+)\psi_{q'm'}(\rho_+)\big)\Big)\,. \end{aligned} \tag{6.13}$$

It can be checked easily that the last line of the above involving the sum of two radial integrals evaluate to zero if $q \neq q'$. Therefore, requiring $(\Phi_{kmq}, \Phi_{k'm'q'}) = \delta_{mm'}\delta_{qq'}\delta(k-k')$

gives,

$$N_{kmq} = \frac{1}{2\pi\sqrt{2\sqrt{k^2+q^2}}||\psi_{mq}||}\,, \tag{6.14}$$

with

$$||\psi_{mq}||^2 = \int_0^{R_1} [J_{|m|}(q\rho)]^2 \rho d\rho + \int_{cR_1}^{cR_2} [c_1 J_{|cm|}(q\rho) + c_2 Y_{|cm|}(q\rho)]^2 \rho/c\, d\rho\,.$$

It can be checked that the solutions defined above are orthogonal with respect to the KG inner product.

We can then proceed with canonical quantisation of the field by defining the field operator as

$$\hat{\Phi}(x) = \sum_{m,q} \int_{-\infty}^{\infty} dk \Big(\hat{a}_{kmq} \Phi_{kmq}(x) + \hat{a}^\dagger_{kmq} \Phi^\dagger_{kmq}(x) \Big)\,, \tag{6.15}$$

where $\hat{a}_{kmq}$ and $\hat{a}^\dagger_{kmq}$ are annihilation and creation operators respectively satisfying the usual commutation relations. We will choose the vacuum state of the field $|0\rangle$ to be the state such that $\hat{a}_{kmq}|0\rangle = 0$ for all $\hat{a}_{kmq}$.

6.3 Response function

We now derive the response function of a UDW detector placed inside the cylinder. For our purposes it is enough to consider simple stationary trajectories where the detector stays at a fixed spatial position. In terms of the proper time τ of the detector, these trajectories are given by:

$$x(\tau) = (\tau, \rho_d, z_d, \phi_d), \tag{6.16}$$

for $\rho_d \in [0, R_1]$, $z_d \in (-\infty, \infty)$ and $\phi_d \in (0, 2\pi]$.

Substituting this trajectory and the mode sum expansion of the Wightman function into (3.9) gives,

$$\begin{aligned} \mathcal{F} &= \int_{-\infty}^{\infty}\int_{-\infty}^{\infty} dt\, dt' \chi_c(t)\chi_c(t') e^{-i\Omega(t-t')} \sum_{m,q} \int_{-\infty}^{\infty} dk N^2_{kmq} |J_{|m|}(q\,\rho_d)|^2 e^{-i\omega(t-t')} \\ &= \sum_{mq} \frac{|J_{|m|}(q\rho_d)|^2}{||\psi_{mq}||^2 4\pi} \int \frac{|\hat{\chi}_c(\Omega + \sqrt{k^2+q^2})|^2}{\sqrt{k^2+q^2}} dk\,. \end{aligned} \tag{6.17}$$

Note that the response of the detector depends, as expected, only on radial coordinate of the detector, and not on its ϕ and z coordinates due to the symmetry of the set-up. In addition, the response does have an implicit dependence on the conicity parameter c coming from the normalisation term $||\psi_{mq}||^2$, see Eq. (6.15). The results of the next section will illustrate this dependence.

6.4 Results

We are now ready to look at how the response $\mathcal{F}_c$ depends on the conicity c. The response of a detector placed in a spacetime with no conical deficit (corresponding to $c = 1$) will be denoted as $\mathcal{F}_{c=1}$.

Dependence on Ω and c

The top diagram in Fig. 6.1 shows a plot of $\mathcal{F}_c - \mathcal{F}_{c=1}$ against Ω for $c \in \{1, 2, 3, 4\}$. From this we see that the difference is indeed non-zero, peaks around $\Omega = 0$, and increases as c increases. In this plot, we have set $\Delta\tau = R_1 = 1$, so that the detectors are switched on only for a short duration, during which no signal could have travelled from the detector to the shell and back to convey information about c. Intuitively, the dependence of the response on c conveys the fact that the local vacuum fluctuations around the detector carry non-local information about the spacetime. The dependence of $\mathcal{F}$ on c can be seen more clearly in Fig. 6.2, which gives a plot of $\mathcal{F}_c$ against c for $\Omega = 0$. This graph shows a logarithmic increase in the response of the detector as c increases.

Dependence on ρ_d

The results shown in Fig. 6.1 were for $\rho_d = 0$, with the detector placed on the axis of symmetry. This greatly reduces the computational effort since $J_m(0) = \delta_{m,0}$ and only the $m = 0$ term in Eq. (6.17) contributes. Fig. 6.3 shows that the difference in response increases as the detector is moved closer to the cylindrical shell. Hence, it is easier for the detector to measure c as it moves closer to the shell.

Dependence on R_2

Recall that we have discretised the integral over q into a discrete sum by introducing a Dirichlet boundary condition at $\rho_+ = cR_2$. Fig. 6.4 shows what happens as we push this

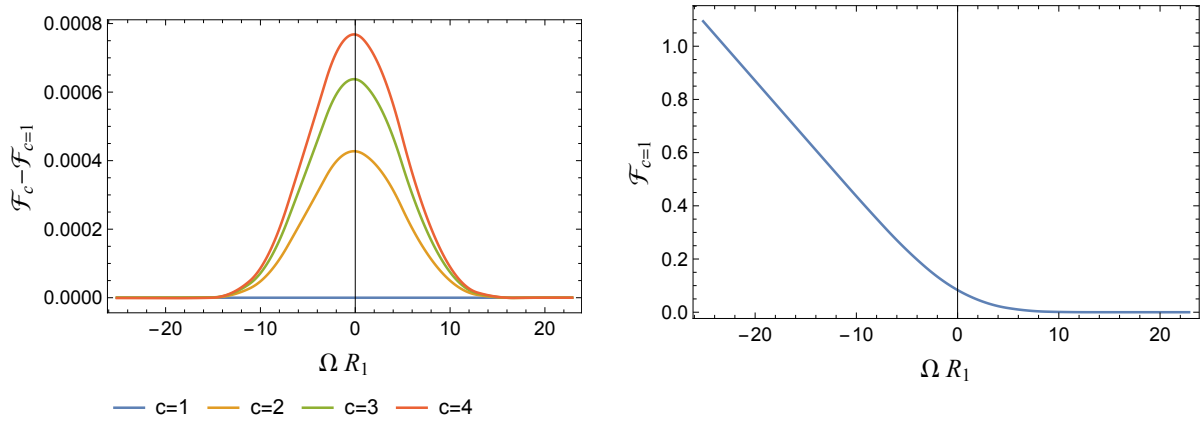

Figure 6.1: Response against detector energy gap. **Left:** This figure shows how the difference $\mathcal{F}_c - \mathcal{F}_{c=1}$ varies with c and the detector energy gap Ω. The difference appears to be symmetric in Ω, and peaks at $\Omega = 0$. The magnitude of the difference also increases with c. **Right:** This figure shows the general shape of $\mathcal{F}$ as a function of Ω. The value of c used here was $c = 1$; the corresponding curves for the other c values in the top plot will simply overlap with the existing curve due to scale of the figure. The other parameters used here are $R_1 = 1$, $R_2 = 5$, $\rho_d = 0$ and $\Delta\tau = 1$.

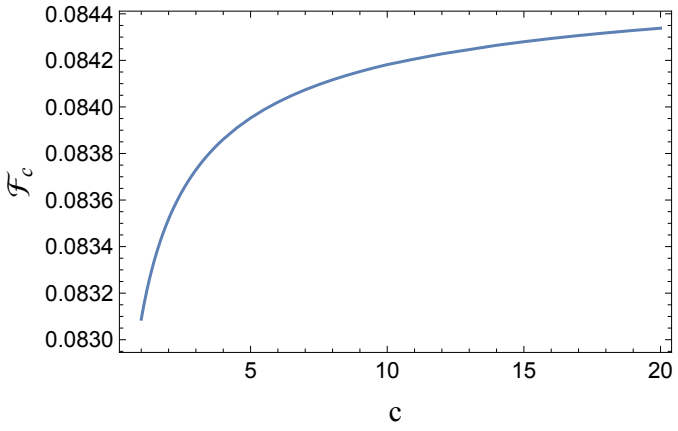

Figure 6.2: Dependence of response on c. This figure gives a plot of $\mathcal{F}_c$ against c for $R_1 = 1$, $R_2 = 5$, $\Omega = 0$, $\rho_d = 0$ and $\Delta\tau = 1$.

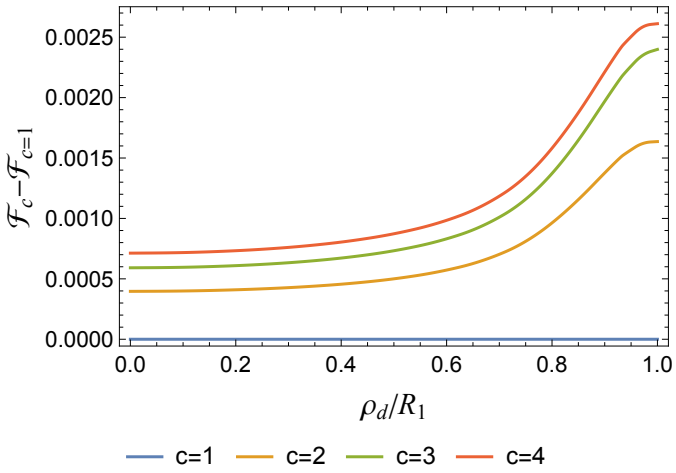

Figure 6.3: Dependence of response on detector radial distance. The figure here shows that the difference $\mathcal{F}_c - \mathcal{F}_{c=1}$ increases as ρ_d increases i.e., the detector gets closer to the cylindrical shell. The parameters used here are $R_1 = 1$, $R_2 = 5$ and $\Omega = 2$.

boundary outwards. From the top figure, we see that the difference in response asymptotes to some finite value as R_2 increases. Meanwhile, plotting the difference in response against Ω at $R_2 = 50$ displays the same trends as Fig. 6.1 but with slightly decreased magnitude. However, based on the top figure, we can expect non-zero differences even when the Dirichlet boundary is pushed out towards infinity.

6.5 Summary

We have shown that a conical deficit exerts a detectable influence on the response of a UDW detector even if that detector is in a flat spacetime region without access to the region of spacetime where the deficit is manifest. An observer restricted to the same region with access only to classical measuring devices would not be able to detect the presence of the deficit outside the cylinder. However the UDW detector can discern the presence of the deficit.

This situation is similar to that for a detector located inside a spherical shell considered in chapter 4: it can read out information about the non-local structure of spacetime even when switched on for scales much shorter than the characteristic scale of the non-locality [44]. As with the spherical shell, we find the sensitivity to the deficit is strongest at

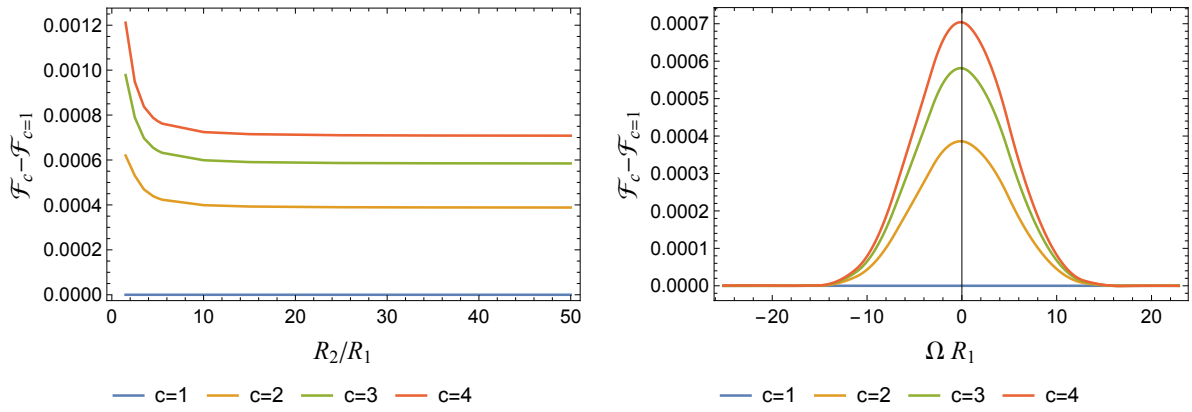

Figure 6.4: Dependence of response on R_2. **Left:** The figure shows a plot of $\mathcal{F}_c - \mathcal{F}_{c=1}$ against R_2, the position of the Dirichlet boundary, for various c values. The difference asymptotes to some non-zero value at large R_2. **Right:** Plot of $\mathcal{F}_c - \mathcal{F}_{c=1}$ against Ω (cp Fig. 6.1) for $R_2 = 50$. The other parameters used here are $R_1 = 1$ and $\rho_d = 0$.

vanishing energy gap for a detector located on the axis of the cylinder, and increases as the detector is located further from the axis.

Finally, we note that one may also consider placing the UDW detector outside the first cylinder. In this case, the $R_1 \to 0$ limit will correspond to a cosmic string placed inside a reflective concentric cylinder. We can see this by noting that $c_2(q) \to 0$ in this limit and the solution $\psi_{mq}(\rho_+)$ in Eq. (6.12) reduces to that in the cosmic string spacetime after normalisation. The model can then be used to compare, for example, the difference between the cases when the string is modelled as a Dirac delta source or as a finite cylinder.

Chapter 7

Entanglement Harvesting in Presence of Dirichlet BC

In the previous three chapters, we have seen how the response of a single UDW detector can be used to discern global features of the spacetime. It turns out that for the purpose of probing global features, having two detectors is sometimes better than one. For example, while a *single* detector displays the same response in the de-Sitter vacuum and a (Minkowski) thermal bath at temperature $\frac{\kappa}{2\pi}$, with κ being the surface gravity of the cosmological horizon [99], the entanglement between *two* detectors can tell the two situations apart [100]. Besides serving as a probe of spacetime structure, entanglement harvesting is an interesting phenomenon in its own right. It tells us how much entanglement can be extracted from the vacuum and has been studied in a variety of contexts [101, 50, 53, 57, 102, 103, 104, 105, 106, 107, 108]. In this chapter, we will study how the presence of a Dirichlet boundary in the spacetime affects entanglement harvesting.

This chapter is based on [4, 5].

7.1 1+1D mirror spacetimes

We will restrict our attention to the simple setting of $1+1$ dimensional Minkowski spacetime, $ds^2 = -dt^2 + dx^2$, where the study of detector response in the presence of Dirichlet boundaries was initiated in [109, 110]. In this case, the boundary, or the "mirror" as it is known, is a point having some arbitrary timelike trajectory at where the scalar field is set

to vanish. Specifically, let us define the usual null coordinates as,

$$u = t - x\,, \quad v = t + x\,, \tag{7.1}$$

and let the path of the mirror be described by,

$$v = p(u)\,. \tag{7.2}$$

Then the field equation and the Dirichlet boundary condition on $\Phi(u, v)$ are

$$\frac{\partial}{\partial u}\frac{\partial}{\partial v}\Phi(u, v) = 0\,, \quad \Phi(u, p(u)) = 0\,. \tag{7.3}$$

Some example trajectories of the mirror considered in this chapter are shown in Fig. 7.2.

A complete set of solutions to Eq. (7.3) is given by $\{u^{in}_\omega, (u^{in}_\omega)^*\}_{\omega\in\mathbb{R}^+}$, where

$$u^{in}_\omega(u, v) = \frac{i}{\sqrt{4\pi\omega}}\big(e^{-i\omega v} - e^{-i\omega p(u)}\big)\,. \tag{7.4}$$

Each of these "in"-modes consists of an incoming plane wave $e^{-i\omega v}$ and an outgoing part $e^{-i\omega p(u)}$ whose dependence on u depends on the mirror trajectory. The vacuum $|0\rangle_{in}$ defined using these modes is called the in-vacuum and is the state that appears to be void of particles to an inertial observer located near past null infinity, $\mathcal{I}^-$. The corresponding Wightman function is [47],

$$W(x; x') = -\frac{1}{4\pi}\ln\left(\frac{\big(p(u) - p(u') - i\epsilon\big)\big(v - v' - i\epsilon\big)}{\big(v - p(u') - i\epsilon\big)\big(p(u) - v' - i\epsilon\big)}\right), \tag{7.5}$$

where ϵ is an UV regulator which is to be taken to zero at the end of computation of physical quantities.

Mirror spacetimes started off as simple toy models for studying Hawking radiation when Fulling and Davies showed [109, 110] that a thermal flux of radiation can be received at future null infinity, $\mathcal{I}^+$, if a suitable trajectory for the mirror is chosen. The computation of this flux is completely analogous to that done in the case of Hawking radiation from black holes. Since then, different mirror trajectories have been constructed that give radiation analogous to various situations, such as eternal black holes [111], black hole collapse [112, 113, 114] and collapse to remnants [115], see also [116] for a collection of different trajectories. Analogies aside, these studies are also a demonstration of particle creation by moving mirrors, an effect now called the dynamical Casimir effect. Experimental demonstration of the dynamical Casimir effect [46] has elevated the status of mirror spacetimes from a theoretical toy model to a physically significant effect in its own right.

Below, we shall see a number of effects that mirrors have on entanglement harvesting, namely, (i) enhancement and suppression of entanglement as compared to global Minkowski spacetime, (ii) a zero entanglement region close to moving mirror which we call the *entanglement shadow* region, and (iii) the effect of an asymptotically null trajectory on harvesting.

In this chapter, we will use either χ_G or χ_c as our switching functions depending on the situation. As in the introductory chapter, we will denote the two detectors using $j = A, B$ and use subscripts to refer to quantities associated to each detectors: X_j denote the x coordinate of detector j, t_j denote the time coordinate of the peak of the switching function of detector j, d_A denotes the distance of the detector closer to the mirror, A from the mirror at $t = t_A$ and finally $\Delta x = X_B - X_A$ for the detector separation. In addition, we shall only be considering static detectors, which are sufficient to illustrate the named effects. As such, the proper times of the detectors agree with the coordinate time t.

7.2 Effects of mirrors on harvesting

7.2.1 Static mirror and entanglement enhancement/suppression

Let us begin by considering the simplest mirror, one having a static trajectory located at $x = 0$. This trajectory is described by

$$p_{static}(u) = u\,. \tag{7.6}$$

We show in Fig. 7.1 the concurrence $C[\rho_{AB}]$ plotted against d_A/σ for detectors placed to the right of this mirror. We use the Gaussian switching (4.15) here. Somewhat surprisingly, for fixed detector separation $\Delta x/\sigma$, we find that the presence of a mirror can actually *enhance* entanglement.

Let us analyse the results in greater detail. First, observe that for all parameter choices, the entanglement starts from zero at the mirror due to Dirichlet boundary condition in Eq. (7.3) and then increases as the detectors move away from the mirror. Far from the mirror, concurrence vanishes for large Δx and small $\Omega\sigma$ (the blue and orange curves in the right figure). When the detector separation Δx is decreased it becomes easier to harvest entanglement as we expect. Indeed, for small Δx (Fig. 7.1, left), the region of entanglement extraction is very large (possibly everywhere $d_A > 0$). Conversely, for sufficiently large Δx the concurrence vanishes and so entanglement cannot be extracted anywhere.

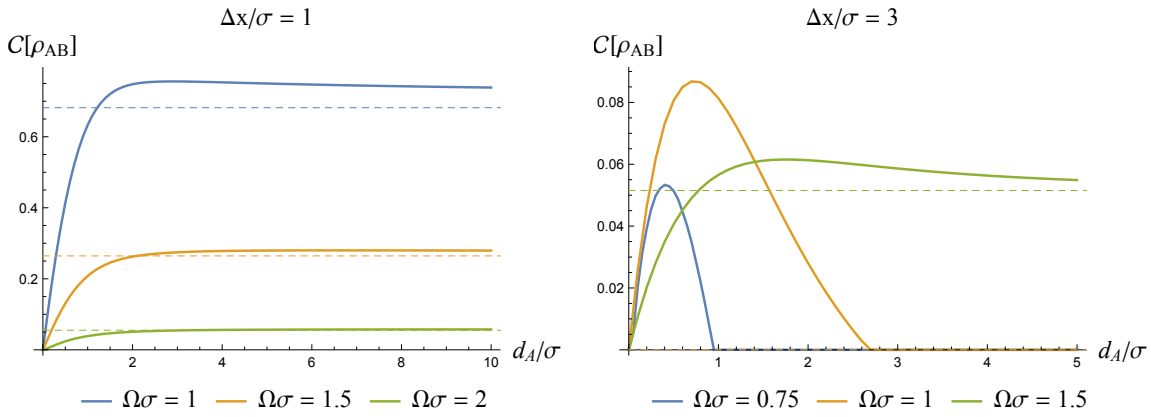

Figure 7.1: Concurrence as a function of distance from mirror d_A with $\sigma = 1$ and for various energy gaps. The left and right plots are obtained for different detector separations $\Delta x/\sigma$ as indicated in the plots. The corresponding free space results are shown as dashed lines in each plot. We observe entanglement enhancement relative to that of free-space in some regions. For $\Delta x/\sigma = 3$ (right plot) and $\Omega\sigma = 0.75, 1$, the free space cases (computed by choosing $\Lambda = 10^{-12}$) have zero concurrence (dashed lines on d_A/σ axis).

Let us now compare the results to free-space (i.e., no mirror). For the comparison, we use the usual Minkowski vacuum, whose Wightman function is given by

$$W_{\mathcal{M}}(x; x') = -\frac{1}{4\pi} \ln \left[\Lambda^2 (u - u' - i\epsilon)(v - v' - i\epsilon)\right], \tag{7.7}$$

where Λ is an IR cutoff. In free space, the IR regulator cannot be removed, which is a peculiarity of $(1+1)$ dimensions alone [108]. This leads to the well-known IR ambiguity in the response of a detector coupled linearly to $(1+1)$ massless scalar field[1].

The interesting observation from Fig. 7.1 is that concurrence in the presence of a mirror can overtake the free-space result (dashed lines on the figure) at large enough d_A/σ and small enough detector separation $\Delta x/\sigma$. As a representative example, consider $\Delta x/\sigma = 3, \Omega\sigma = 1$. Noting that the free space case (dashed line) has zero concurrence, we see that entanglement harvesting would not have been possible at all if not for the presence of the mirror. Heuristically, this can be understood as a reflection effect in which information from one detector can reach the other detector after reflecting off the mirror. The trade off between this reflection effect and the vanishing of the Wightman function close to the

[1]Note that the mirror "regulates" the IR ambiguity in the Wightman function (7.5) as the Λ^2's which should be present in both the numerator and denominator inside the ln cancel each other.

mirror leads to a peak in the concurrence at some optimal d_A away from the mirror. This qualitative behaviour is also present for the other mirror trajectories to be considered below. The main feature displayed here is that of *entanglement enhancement*: mirrors can amplify entanglement extraction relative to the free-space scenario.

Accelerating mirrors contain richer entanglement dynamics than the static one. Furthermore, the field operator along the (static) detector trajectory will not be identically zero during the switched on time of the detector. Hence naively we do not expect entanglement to completely vanish even if the detector coincides with the mirror at some single instant in t. We will see that the dynamics of entanglement is indeed quite non-trivial, as we explicitly demonstrate next for the so called Carlitz-Willey (CW) trajectory.

7.2.2 Carlitz-Willey mirror and shadow region

The CW mirror follows the trajectory given by,

$$p_{CW}(u) = -\frac{1}{\kappa_c} e^{-\kappa_c u}\,, \tag{7.8}$$

where $\kappa_c \in \mathbb{R}^+$ parametrises the acceleration of the mirror. It corresponds to a mirror that emits thermal radiation just like that of an eternal black hole [111] of surface gravity κ_c. Fig. 7.2 shows some example trajectories having different κ_c values.

The concurrence results for CW mirrors are shown in Fig. 7.3. We focus on one particular choice – $\kappa_c\sigma = 0.5, \Omega\sigma = 1$ – which captures all the qualitative features we hope to highlight.

The CW mirror scenario contains more interesting physics compared to its static counterpart. In contrast to the static mirror case, where entanglement vanishes only at the mirror due to the boundary condition (cf. Fig. 7.1), we see from the first graph of Fig. 7.3 that there can be a small finite region of *entanglement shadow* near the mirror, i.e., a region deprived of entanglement. However, this depends on the other detector parameters as well. In the example shown, the shadow region is present for $\Delta x/\sigma = 3$ and is absent for $\Delta x/\sigma = 2$. The possibility of a shadow region is reminiscent of the situation when detectors are placed too close to a black hole event horizon [102], but the physical origin is different since there is no black hole in our case. For the black hole, the origin of the entanglement shadow is due to a redshift factor diminishing the non-local correlations relative to the local noise terms [102]. In the present case, superficially there is a (nonlinear) competition between the local noise term $\sqrt{P_A P_B}$ and the nonlocal term $|X|$ due to the

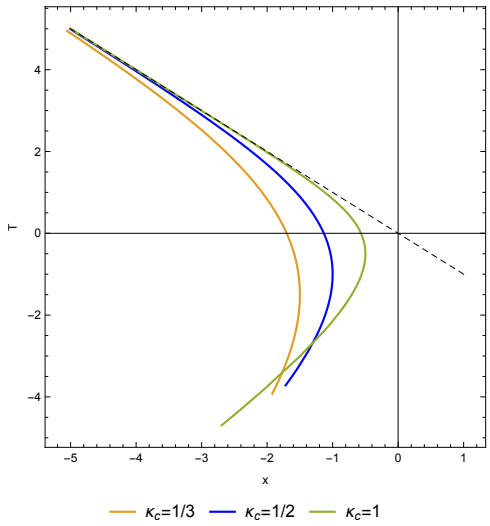

Figure 7.2: Carlitz-Willey (CW) mirror trajectories. CW mirrors are asympotically null, approaching the $v = 0$ line (dashed) at late times.

logarithmic behaviour of the Wightman function since they each grow at a different pace with distance from mirror at some fixed time t, as shown in the third plot of Fig. 7.3.

CW mirrors can also enhance entanglement. The size of the region of entanglement enhancement depends on the relative separation of the two detectors, as the left plot of Fig. 7.3 shows.

To summarize, we see that the main effect a non-trivial mirror trajectory has on entanglement harvesting is the generic presence of an *entanglement shadow* near the mirror. The strip where this occurs may increase or decrease in size depending on the proximity of the detectors.

7.2.3 Digression: Derivative coupling

Upon closer scrutiny, two subtleties in the above sections may cause one to question the validity of the results. The first is the ambiguity in the free-space concurrence results due to the infrared cut-off and the second is the spurious effect of an unbounded growth in the excitation probability of a detector in the mirror spacetime (see Fig. 7.3).

However, these two subtleties can be bypassed altogether by considering a derivative type coupling (see for example [28]) between the detector and the field. In this subsection,

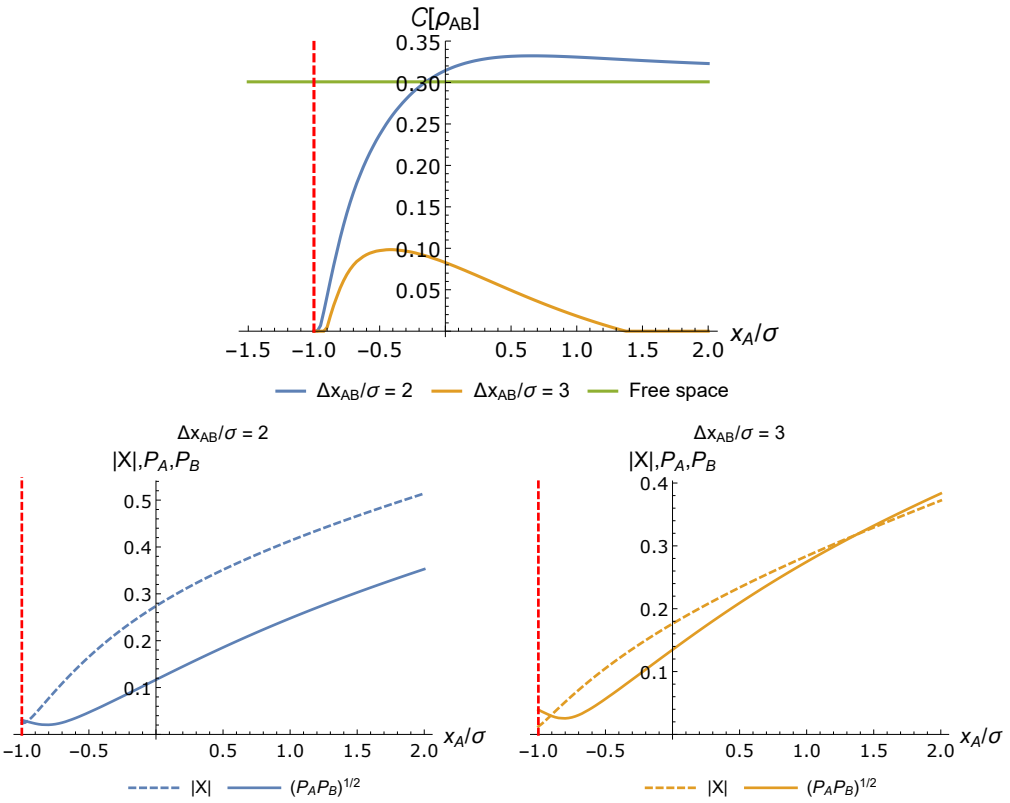

Figure 7.3: **Top:** A plot of concurrence for the CW mirror (in red at time $t = -1$), as a function of the position of detector A for various fixed detector separations Δx, with $\kappa_c = 0.5, \Omega = 1, \sigma = 1$. **Bottom Left:** The nonlocal term $|X|$ and local noise $\sqrt{P_A P_B}$ terms for the $\Delta x = 2\sigma$ trajectory in the left figure. **Botton Right:** The nonlocal term $|X|$ and local noise $\sqrt{P_A P_B}$ terms for $\Delta x = 3\sigma$. The small region where the two curves intersect give the finite non-zero entanglement region. Note the small zones of entanglement shadow near the mirror on the left plot for both cases; these appear in the other two plots where we see that $|X| < \sqrt{P_A P_B}$ very close to the mirror.

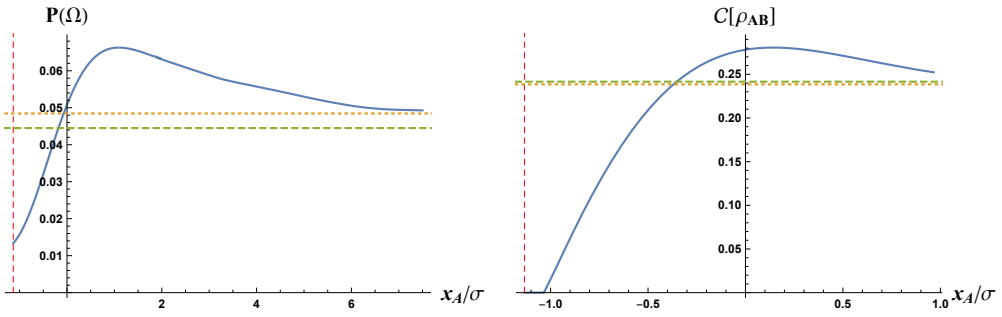

Figure 7.4: Derivative coupling results. **Left**: The use of derivative coupling removes the IR ambiguity in the free-space $P(\Omega)$ (dashed, green). The probability of excitation in the CW mirror spacetime now remains bounded at large x_A/σ. It asymptotes to a value (dotted, yellow) slightly higher than the free-space result. **Right**: The concurrence against x_A/σ plot shows the same qualitative behaviour as linear coupling. Namely, we observe a region of entanglement enhancement and a region of entanglement shadow close to the mirror. The concurrence will asymptote to a value (dotted, yellow) slightly below the free-space result (dashed, green). In this plot, $\kappa\sigma = 0.5$, $\Omega\sigma = 1$, $t_A/\sigma = 0$ and $\Delta x/\sigma = 1$.

we employ this alternative coupling, and show that in the absence of the above two effects, the qualitative results obtained in the previous sections still hold.

Instead of the linear coupling between the detector monopole moment and the field operator $\hat{\Phi}$ in Eq. 3.1, we can replace $\hat{\Phi}(x(\tau))$ with its proper time derivative to obtain the derivative coupling,

$$\tilde{H}_{I,j} = \lambda \chi_j(\tau) \hat{\mu}_j(\tau) \otimes u_j^\mu \nabla_\mu \hat{\phi}(x_j(\tau)) \,,$$

where u_j^μ is the velocity vector along $x_j(\tau)$. For detectors static in the (t, x) coordinates, we have $t = \tau$ and the proper time derivative reduces to partial derivative ∂_t.

As shown in [28], in addition to removing the dependence of the excitation probability on the infrared cut-off, this coupling also results in an expression for the probability that looks more similar to the $(3 + 1)$D case. In the current case, we can see this by the following: the expressions for $P(\Omega)$ and X given in Sec. 3.3.1 can be easily modified to accommodate the change in coupling by making the replacement $W(x_{j_1}(\tau); x_{j_2}(\tau')) \to A(x_{j_1}(\tau); x_{j_2}(\tau')) \equiv \partial_\tau \partial_{\tau'} W(x_{j_1}(\tau); x_{j_2}(\tau'))$ whenever it appears.

In particular, for the static trajectories considered here, we have

$$A_f(x;x') = -\frac{1}{4\pi}\left(\frac{1}{\Delta u - i\epsilon} + \frac{1}{\Delta v - i\epsilon}\right), \tag{7.9}$$

$$A_m(x;x') = -\frac{1}{4\pi}\left(\frac{p'(u)p'(u')}{\big[p(u)-p(u')-i\epsilon\big]^2} + \frac{1}{\big[v-v'-i\epsilon\big]^2} - \frac{p'(u')}{\big[v-p(u')-i\epsilon\big]^2} - \frac{p'(u)}{\big[p(u)-v'-i\epsilon\big]^2}\right) \tag{7.10}$$

respectively for free space and mirror spacetimes. These replace the Wightman functions in (7.7) and (7.5) respectively. Since A_f does not require an IR regulator to be well-behaved, the IR ambiguity in $P(\Omega)$ and $|X|$ is removed. Furthermore, the similarity between A_f and the $(3+1)$D Wightman function also indicates that the results for $P(\Omega)$ and $|X|$ in $(3+1)$D using linear coupling will be similar to that obtained using derivative coupling in $(1+1)$D. In fact, for the free space scenario the function $A_f(x,x')$ in $(1+1)$ dimensions only differs from the linear coupling Wightman function in $(3+1)$D by a constant factor of 2, so the physics is practically identical.

In Fig. 7.4, we show the results obtained using derivative couplings between the detectors and the field. From the $P(\Omega)$ plot, we see that the probability in the CW mirror spacetime remains bounded at large d_A rather than blowing up as in Fig. 7.3. We note also that the free-space value in this case was computed without the need for choosing an IR cut-off. In addition, we see that derivative coupling results in the same qualitative findings as the previous subsections: there is a region of entanglement enhancement over the free-space result and entanglement shadow near the mirror.

7.2.4 Effect of horizon

The CW mirror considered in the above is an example of a trajectory having an "horizon". For the trajectories shown in Fig. 7.2, the horizon is the dashed black line on the figure given by $v = 0$. This is the line beyond which left moving wave modes originating from the right past null infinity, $\mathcal{I}_R^-$, will reach $\mathcal{I}_L^+$ instead of $\mathcal{I}_R^+$ (see Fig. 7.5). The presence of such a horizon results in information loss to an observer located near $\mathcal{I}_R^+$ as he will never see information about the field modes that never get reflected. These field modes are analogous to those that get trapped in a black hole, reaching the singularity, never to return again. Left moving modes that do reflect are analogous to those waves that flow

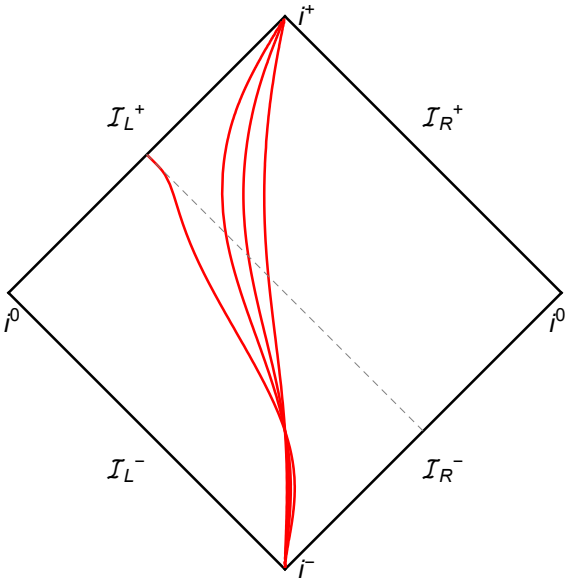

Figure 7.5: The trajectory, Eq. (7.11), plotted in a Penrose conformal diagram. Here $\kappa = 1$, $v_H = 0$ and $\xi = 0.2$, 0.4, 0.6 and 1 respectively. The mirror never forms a strict horizon as long as $\xi < 1$: all left-moving modes ultimately reflect and become right-movers. When $\xi = 1$, the trajectory ends on $\mathcal{I}_L^+$ and light rays from $\mathcal{I}_R^-$ lying after the horizon (dashed) will not get reflected by the mirror.

through the center of the collapsing star to eventually escape, reaching an outside observer. Hence, mirror toy models of black hole evaporation tend to have horizons.

In this subsection, we will demonstrate the qualitative effect of the presence of a horizon on entanglement harvesting using the cosine switching function χ_c. We do so by considering a family of mirror trajectories [117],

$$p_\xi(u) = u + \frac{\xi}{\kappa} \log\left[\frac{1+\xi}{2}\mathbf{W}\Big(\frac{2}{1+\xi}e^{\frac{2\kappa(v_H-u)}{1+\xi}}\Big)\right], \tag{7.11}$$

where $\mathbf{W}(\cdot)$ is the product-log function. The parameter ξ represents the asymptotic final future speed of the mirror, while κ parametrizes how fast this speed is achieved. The trajectory can also be written in terms of the (t, x) coordinates as:

$$x_\xi(t) = \xi(v_H - t) - \frac{\xi}{2\kappa} W\big(2e^{2\kappa(v_H-t)}\big). \tag{7.12}$$

We thus see that the last parameter v_H simply translates the mirror trajectory in time along the t axis. Each mirror in the family drifts at a constant velocity in the far future,

with $\lim_{t\to\infty}|\frac{dx_\xi}{dt}| = \xi$. Some exemplary trajectories are shown in the Penrose diagram Fig. 7.5. From this diagram, we see that trajectories with $\xi < 1$ end at future timelike infinity while the $\xi = 1$ mirror ends on $\mathcal{I}_L^+$. The latter leads to the presence of a horizon, given by the dashed line.

We note that when $\xi = 1$, the trajectory is also known as the "black hole collapse trajectory" (BHC) trajectory,

$$p_{BHC}(u) = v_H - \frac{1}{\kappa}W(e^{-\kappa(u-v_H)}). \tag{7.13}$$

This trajectory has a one-to-one correspondence with the canonical case of time dependent particle creation from a collapsing star (null shell) [114]. Let us now look at entanglement harvesting in these mirror spacetimes.

Shadow region

We begin by looking at how the $\mathcal{C}$ against d_A curves change with increasing ξ in Fig. 7.6. In the previous section, we have seen that for a fixed η, T, Δx and Ω, there is a minimal d_A below which it is impossible to entangle the detectors. This region is the entanglement shadow zone. The dashed purple curve in the top plot of Fig. 7.6 illustrates this for $\xi = 1$. However, the shadow zone is not unique to this BHC mirror. For example, when $\xi = 0.7$ (blue), a shadow zone also exists. In fact we have checked that such entanglement shadow zones are present even when the mirror is moving with constant, non-zero velocity, and therefore is generally a characteristic of non-static mirrors (as opposed to mirrors with horizons).

These results are commensurate with previous studies on entanglement harvesting. While the presence of horizons certainly plays a role [102], other factors are also at play, including the state of motion of the detectors [118, 119], local vs. global considerations [120], and sensitivity of the detector to particular parameterizations [105, 121]. In particular, higher dimensional effects on entanglement shadow will be an interesting question to address, since the evidence we present here is limited to (1+1)-dimensions.

In addition, we observe an emergence of entanglement close to the mirror at later times. This is illustrated in the $T = 1$ plot (bottom) of Fig. 7.6: at $T = 1$, the shadow zone disappears for near-null mirrors. However, this emergence is again not unique to the BHC mirror. At this T, we have checked numerically that entanglement harvesting at $d_A = 0$ becomes possible, i.e. $\mathcal{C} > 0$, when $\xi \gtrsim 0.9997$.

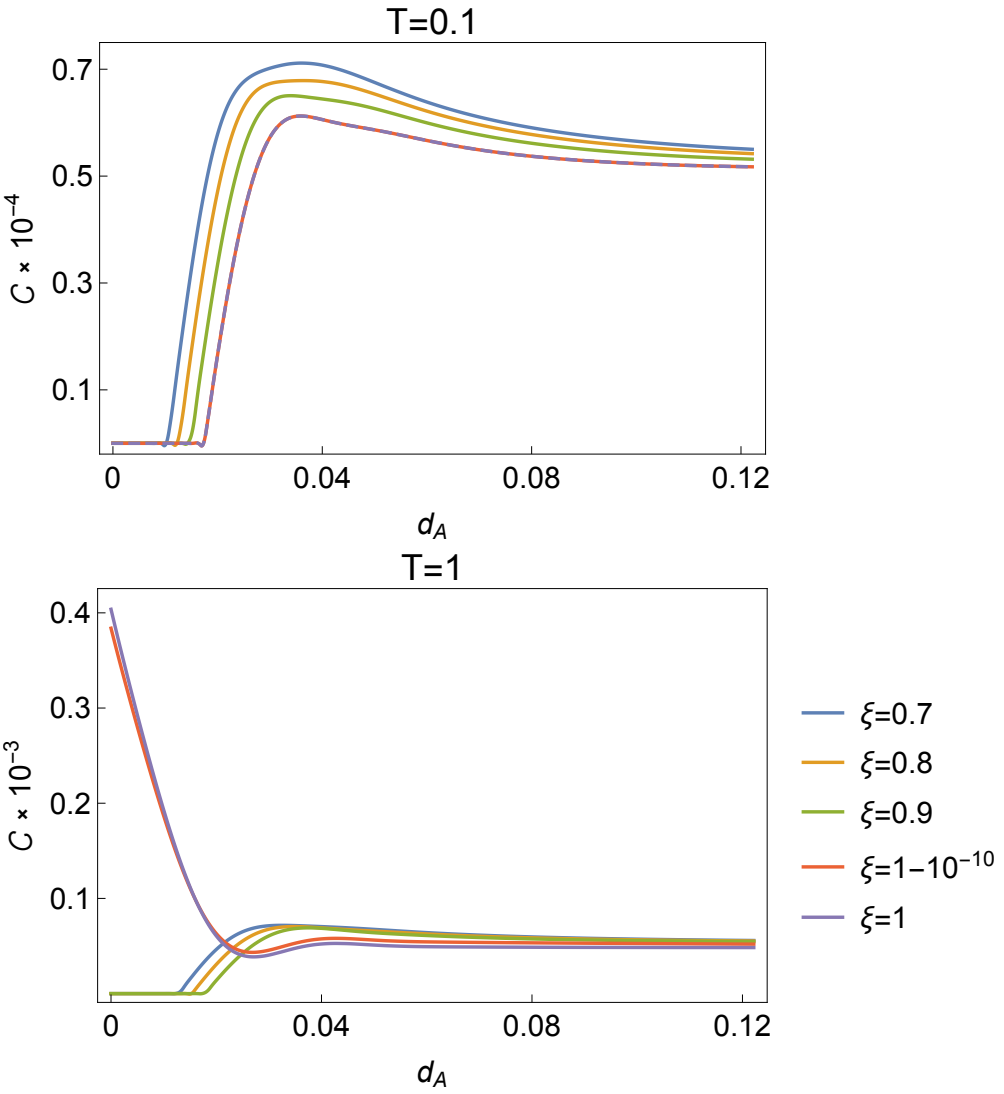

Figure 7.6: Plots of concurrence against d_A. The curves for $T = 0.1$ (top) are similar to that in Fig 7.3, namely at small d_A, there is a zone of entanglement shadow with zero concurrence, while the concurrence increases to some peak before asymptoting to some constant value at large d_A. We note that entanglement shadow is present even for the $\xi < 1$ mirrors, indicating that it is not a feature unique to mirrors with horizons. At a later time $T = 1$, we see an emergence of concurrence near the mirror when $\xi \lesssim 1$ and the shadow zone disappears.

Late time linear growth in $\mathcal{C}$

A distinct difference in behaviour arises when we consider a second scenario: once again, the detector separation Δx is fixed but instead of varying d_A, we fix this and consider the effect of varying T. Some representative cases are shown in Fig. 7.7. From these plots we see that while the concurrences for $\xi < 1$ mirrors asymptote to finite values at large T, an asymptote does not seem to be present for the BHC mirror. In all cases, the $\mathcal{C}$ in the BHC mirror spacetime seems to increase linearly at late times[2].

At late times, the mirrors approximately move at constant speeds. It is thus natural to expect the late time asymptotes for the $\xi < 1$ cases to be equal to the concurrence of detectors situated in spacetimes with mirrors moving (eternally) at the corresponding constant speeds. In fact, the dashed lines representing the asymptotic values of the different mirrors in Fig. 7.7 are obtained precisely in this way. Roughly speaking, when $\xi < 1$, both the P and X terms have finite large T limits, corresponding to the constant speed mirror P and X values. This thus gives an asymptotic value for the concurrence. However corresponding values for $\xi = 1$, do not exist.

Computing the asymptotic values

Let us now look explicitly at how this is done for P_A. There are two ways to measure the probability "at time $t = T$": we can either directly include T in the switching function, setting $\chi(t) = \cos^4(\eta(t - T))$, or we can shift the trajectory down by T units by setting $v_H = -T$ in the $p_\xi(u)$ terms of the Wightman function Eq. (7.5). These two methods are physically equivalent and yield the same results, but we will use the latter to explain the asymptotic behaviour observed in Fig. 7.7.

Let us consider the first piece of the Wightman function given by $\ln\left[p_\xi(t-X_A)-p_\xi(t'-X_A)-i\epsilon\right]$, where we have written X_A to indicate that this is evaluated along detector A's trajectory (the analysis for detector B is similar and will be skipped). Recall that detector A is being placed $X_A = x_\xi(T) + d_A$, where $x_\xi(t)$ is the mirror trajectory Eq. (7.12) with

[2]Due to computational constraint, we checked this up to $T \approx 30$, where the UV regulator ϵ in the Wightman function needs to be $\sim 10^{-320}$ for convergence.

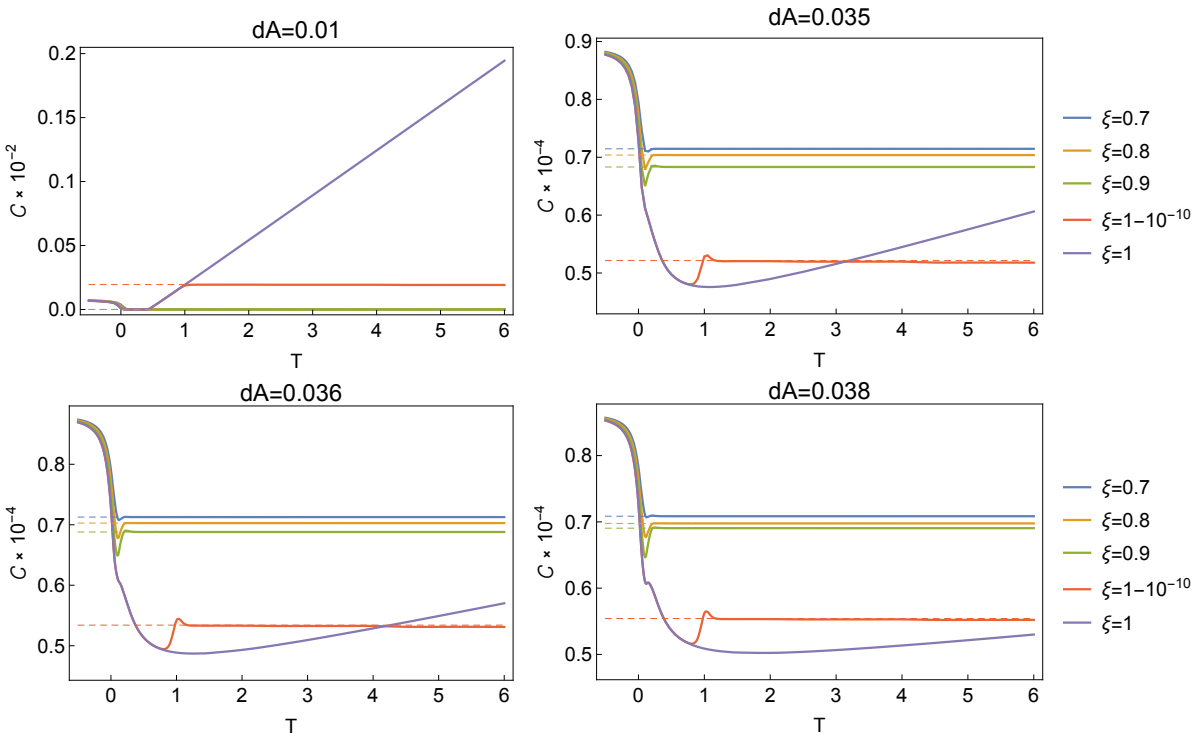

Figure 7.7: Plots of concurrence against T for various d_A. Note that the curves for $\xi = 0.7, 0.8, 0.9$ in the first plot overlaps on the T-axis, corresponding to the fact that $d_A = 0.01$ lies within the entanglement shadow zone for these mirrors. The parameters used here are $\kappa = \sqrt{48\pi}$, $\eta = 23$, $\Omega = 50$ and $\Delta x = 0.05$.

$v_H = 0$. Substituting this into the expression for p_ξ (with $v_H = -T$) we have

$$\begin{aligned}
&p_\xi(t - X_A) - p_\xi(t' - X_A) \\
=&u + \frac{\xi}{\kappa}\log\left[\frac{1+\xi}{2}\mathbf{W}\big(\frac{2}{1+\xi}e^{\frac{2\kappa(-T-u)}{1+\xi}}\big)\right] - u' - \frac{\xi}{\kappa}\log\left[\frac{1+\xi}{2}\mathbf{W}\big(\frac{2}{1+\xi}e^{\frac{2\kappa(-T-u')}{1+\xi}}\big)\right] \\
=&t - t' + \frac{\xi}{\kappa}\log\left[\mathbf{W}\big(\frac{2}{1+\xi}e^{\frac{2\kappa(-T-u)}{1+\xi}}\big)\right] - \frac{\xi}{\kappa}\log\left[\mathbf{W}\big(\frac{2}{1+\xi}e^{\frac{2\kappa(-T-u')}{1+\xi}}\big)\right] \\
=&t - t' + \frac{\xi}{\kappa}\log\left[\frac{2}{1+\xi}e^{\frac{2\kappa(-T-u)}{1+\xi}}\right] - \frac{\xi}{\kappa}\mathbf{W}\big(\frac{2}{1+\xi}e^{\frac{2\kappa(-T-u)}{1+\xi}}\big) \\
&\quad - \frac{\xi}{\kappa}\log\left[\frac{2}{1+\xi}e^{\frac{2\kappa(-T-u')}{1+\xi}}\right] + \frac{\xi}{\kappa}\mathbf{W}\big(\frac{2}{1+\xi}e^{\frac{2\kappa(-T-u')}{1+\xi}}\big) \\
=&t - t' - \frac{2\xi(T+u)}{1+\xi} - \frac{\xi}{\kappa}\mathbf{W}\big(\frac{2}{1+\xi}e^{\frac{2\kappa(-T-u)}{1+\xi}}\big) + \frac{2\xi(T+u')}{1+\xi} + \frac{\xi}{\kappa}\mathbf{W}\big(\frac{2}{1+\xi}e^{\frac{2\kappa(-T-u')}{1+\xi}}\big)\,,
\end{aligned} \tag{7.14}$$

where in going from the second to the third equality we used the identity $\log[\mathbf{W}(x)] = \log[x] - \mathbf{W}(x)$. Next, we would like to take the $T \to \infty$ limit. First, note that $u = t - X_A = t - x_m(T) + d_A$. Meanwhile,

$$x_\xi(T) = -\xi T - \frac{\xi}{2\kappa}W\big(2e^{-2\kappa T}\big) \to -\xi T \tag{7.15}$$

since $\mathbf{W}(0) = 0$. Making use of this fact again for the terms involving $\mathbf{W}(\cdot)$ in the previous equation, we have

$$\begin{aligned}
p_\xi(t - X_A) - p_\xi(t' - X_A) &\to t - t' - \frac{2\xi(T+u)}{1+\xi} + \frac{2\xi(T+u')}{1+\xi} \\
&= t - t' - \frac{2\xi(u-u')}{1+\xi} \\
&= \left(1 - \frac{2\xi}{1+\xi}\right)(t - t')\,.
\end{aligned} \tag{7.16}$$

Hence,

$$\ln\left[p_\xi(t - X_A) - p_\xi(t' - X_A) - i\epsilon\right] \to \ln[\big(1 - \frac{2\xi}{1+\xi}\big)(t - t') - i\epsilon]\,. \tag{7.17}$$

This asymptotic form coincides with the piece contained in the Wightman function of a mirror moving to the left at constant time-like speed $\xi < 1$ passing through the origin.

The trajectory of such a mirror is $t = -x/\xi$, or equivalently,

$$v = (1 - \frac{2\xi}{1+\xi})u \equiv p_c(u)\,. \tag{7.18}$$

Therefore as promised, we have $\ln\left[p_c(t-X_A) - p_c(t'-X_A) - i\epsilon\right] = \ln[\left(1-\frac{2\xi}{1+\xi}\right)(t-t') - i\epsilon]$ which is the right hand side of Eq. (7.17). Repeating this for each of the three remaining pieces in eq. (7.5), we will find that *at large T, the Wightman function approaches that of the constant speed mirror*. Clearly, repeating this analysis for P_B and X will demonstrate that they too asymptote to the constant speed mirror value at large T. We have thus successfully explained the asymptotic value of concurrence of the time-like mirrors in Fig. 7.7.

Finally, we attempt to investigate whether the concurrence with a $\xi = 1$ mirror asymptotes to a finite, non-zero value. For any $\xi < 1$, the expression in eq. (7.16) tends to a finite value whenever $t \neq t'$. This gives a finite P when the UV-regulator is taken to $\epsilon \to 0$ at the end. However when $\xi = 1$, the expression in eq. (7.16) is identically zero for all $t\,, t'$ values, giving $\ln\left[p(t-x_d) - p(t'-x_d) - i\epsilon\right] \to \ln(-i\epsilon)$ which diverges in the limit $\epsilon \to 0$. Due to this behavior of the Wightman function, an asymptotic value of P for large T does not exist for $\xi = 1$. To investigate how the divergence occurs at large T, we expand the terms involving the $\mathbf{W}(\cdot)$ functions in eq. (7.14) to subleading order in $e^{-\kappa T}$:

$$\begin{aligned}
&-\frac{1}{\kappa}\mathbf{W}\left(e^{\kappa(-T-u)}\right) + \frac{1}{\kappa}\mathbf{W}\left(e^{\kappa(-T-u')}\right) \\
&= -\frac{1}{\kappa}\mathbf{W}\left(e^{-\kappa T-\kappa(t+d_A+T+\frac{1}{2\kappa}\mathbf{W}\left(2e^{-2\kappa T}\right)}\right) + \frac{1}{\kappa}\mathbf{W}\left(e^{-\kappa T-\kappa(t'+d_A+T+\frac{1}{2\kappa}\mathbf{W}\left(2e^{-2\kappa T}\right)}\right) \\
&\to \frac{e^{-2T\kappa}}{\kappa}(e^{\kappa(d_A-t')} - e^{\kappa(d_A-t)}) + O(e^{-4T\kappa})\,.
\end{aligned} \tag{7.19}$$

Hence for the BHC mirror, we have $\ln\left[p_\xi(t-X_A) - p_\xi(t'-X_A) - i\epsilon\right] \to \ln(\frac{e^{-2T\kappa}}{\kappa}(e^{\kappa(d_A-t')} - e^{\kappa(d_A-t)}) - i\epsilon) = -2\kappa T + \log(\frac{1}{\kappa}(e^{\kappa(d_A-t')} - e^{\kappa(d_A-t)}) - i\epsilon)$ after a rescaling of the small parameter ϵ. An example of the plot of P_A and $|X|$ against T is shown in Fig. 7.8.

We thus have P and $X \to \infty$ at large T when $\xi = 1$. We note that the results obtained are only valid to leading order in perturbation. In particular, the apparent linear increase in P, $|X|$, and $\mathcal{C}$ in T for the $\xi = 1$ mirror at late times will not continue indefinitely in the real world — perturbations of higher orders will eventually be needed to accurately describe the large T behaviour.

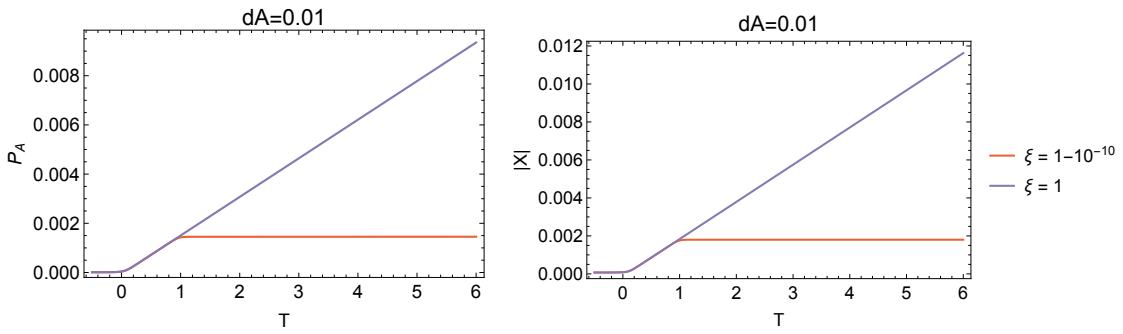

Figure 7.8: Linear increase in P and $|X|$ for $\xi = 1$. The parameters used here are $\kappa = \sqrt{48\pi}$, $\eta = 23$, $\Omega = 50$, $d_A = 0.01$ and $\Delta x = 0.05$.

Comparison with entropy

Interestingly, such a linear late time growth is also observed for the regularised von Neumann entanglement entropy, $S(u)$, of the state $|0\rangle_{in}$. This is given by $S(u) = -(1/12)\log p'(u)$ [115] for mirror spacetimes. Roughly speaking, this measures the amount of entanglement between the two spacetime regions lying respectively before and after the null-line u. A plot of $S(u)$ for the different trajectories is given in Fig. 7.9 (see also [122]). For the $\xi = 1$ trajectory, there is information loss that can be characterized by a divergent entanglement. A diverging entanglement entropy has also been observed in null-shell collapse to a black hole in [123]. There, the linear increase was interpreted as being due to a constant rate of entanglement entropy production by the black hole. As mentioned in the introduction, the UDW model serves as an operational way of measuring the amount of entanglement present in the vacuum. It is thus satisfying to see an agreement in the qualitative behaviour between the concurrence of the detectors and the entanglement entropy between different spacetime regions. This correspondence at least suggests that the ever-increasing concurrence that appears for the horizon mirror can be intuitively thought of as a direct result of loss of information in the system. Of course, further case studies are necessary to see if this agreement is a mere coincidence.

7.3 Summary

We have performed in (1+1) dimensions investigations of entanglement harvesting between two detectors in the presence of mirrors using linear and derivative couplings between the detectors and the quantum field. We looked at both static and non-inertial trajectories.

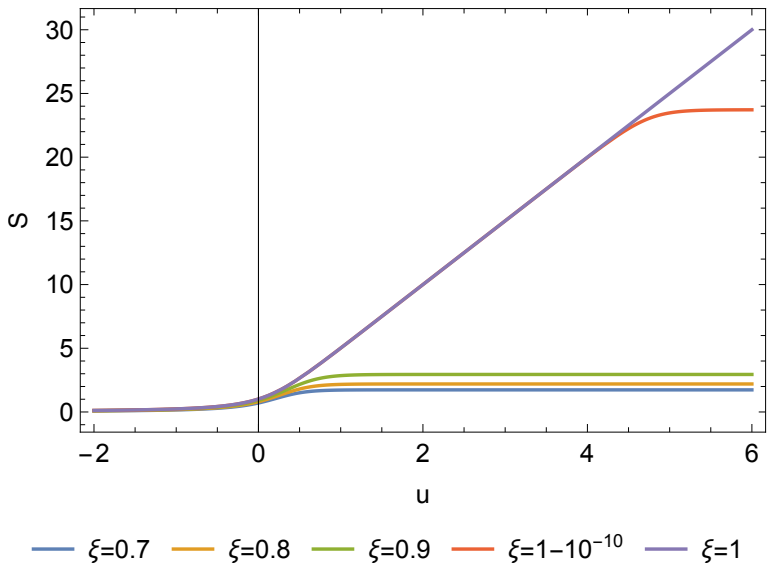

Figure 7.9: Plot of von Neumann entanglement entropy, $S(u) = -(1/12)\log p'(u)$, for the class of mirror trajectories Eq. (7.11) with final drifting speeds ξ. Notice the asymptotic divergent entropy for the horizon case $\xi = 1$, which is in qualitative agreement with results of Fig. 7.7, suggesting non-unitary evolution -information loss in the horizon system is responsible for the divergence in concurrence.

We find that in both cases mirrors can enhance entanglement: entanglement harvested between two detectors can be greater in the presence of a mirror as compared to free space. However for non-inertial trajectories we find a region of entanglement shadow close to the mirror, similar to what is observed close to black holes in [102]. Physically, our results provide a theoretical prediction of what to expect of the entanglement detection in the presence of the DCE.

We also found that concurrence can distinguish between the global property of a dynamic spacetime containing a horizon and one without. However, the effect is subtle and harvesting without horizons does not dramatically affect entanglement. Entanglement shadow regions can exist for both horizon mirrors and horizonless mirrors, as we depict in $\mathcal{C} - d_A$ plots of Fig. 7.6. However for horizon mirrors concurrence at small d_A "revives" as time increases. The most striking difference is illustrated in Fig. 7.7: concurrence for horizonless mirrors asymptotes to finite values at large T, but for horizon mirrors concurrence evidently has no asymptote.

It will be interesting for further studies to find out why concurrence in the presence of horizons exhibits a shadow zone that can "revive" at large T, which may depend on properties of the horizon. Likewise, it will be even more interesting to see what features of this study are preserved in actual gravitational collapse.

Part II

Black Hole Thermodynamics

Chapter 8

Black Hole Thermodynamics in Extended Phase Space

The second part of this thesis is devoted to the phase transitions of slowly accelerating black holes in Anti-de Sitter spacetimes. We will begin in this chapter with a general review of black hole thermodynamics, before moving on to the specific thermodynamics of accelerating black holes in the next chapter.

8.1 Black hole as thermodynamic systems

Since Hawking's discovery of black hole radiation [9], black holes have generally been accepted to be thermodynamic systems – systems to which can be attributed thermodynamic variables such as entropy, temperature and energy, and for which the usual laws of thermodynamics apply. In particular, using techniques from quantum field theory in curved spacetime, Hawking found that the particle spectrum coming from a black hole is a Planck spectrum with temperature $\frac{\kappa}{2\pi}$, where κ is the surface gravity (definition below) of the black hole. Thus even though a classical black hole is simply a region from which no particles can escape, quantum mechanical considerations helped reveal its radiative properties. In familiar thermodynamic systems such as the Ising model, the entropy is a measure of the number of quantum mechanical microscopic states of the system. Furthermore, the second law, which states that the total entropy of a closed system cannot decrease, is statistical in nature and results from the overwhelming probability of a large number of particles to disorder rather than order themselves. Surprisingly, each of the four laws of

thermodynamics for black holes can be derived directly using general relativity [124]. As a result, even though we do not have a theory of quantum gravity, by matching terms in these laws, we are led to a value of $A/4$ for the entropy of a black hole where A is the area of the event horizon. Let us now recall what these laws are for stationary black holes in 4D Einstein-Maxwell theory. The derivation of these can be found for example in [124, 125].

First, recall that a stationary spacetime is one admitting a Killing vector field that is timelike in a neighbourhood of $\mathcal{I}^{\pm}$, expressing the time translation invariance of the spacetime. Stationary black holes are thus equilibrium systems i.e., their physical attributes are not changing in time, analogous to equilibrium thermodynamic systems. The four laws are derived from the Einstein-Maxwell field equations, together with certain energy conditions imposed on the energy-momentum tensor T_{ab}, which are expected to be satisfied by ordinary matter. The energy condition imposed can be either of the following:

Dominant energy condition. $-T^a_b X^b$ is a future directed, causal vector for all timelike, future directed vectors X^b.

Weak energy condition. $T_{ab}X^aX^b \geq 0$ for all causal vectors X^a. Replacing "causal" with "null" gives us the **null energy condition**.

Strong energy condition. $(T_{ab} - 1/2 g_{ab}T^c_c)X^aX^b \geq 0$ for all causal vectors X^a.

Zeroth law

The zeroth law concerns the surface gravity of the black hole. Recall that the surface gravity κ of a black hole is the quantity satisfying,

$$\xi^a \nabla_a \xi^b|_{\mathcal{H}} = \kappa \xi^b \,, \tag{8.1}$$

on the event horizon $\mathcal{H}$ of the black hole, where ξ is the generator of $\mathcal{H}$. It is the force required for an observer at infinity to hold a unit test mass at rest near the horizon. The zeroth law of black hole mechanics states that κ is a constant on the event horizon of a stationary black hole spacetime obeying the dominant energy condition [36]. Since Hawking radiation tells us that the temperature $T = \frac{\kappa}{2\pi}$, this is equivalent to saying that the temperature of equilibrium black holes are constant.

First law

The first law concerns how the change in mass M is related to changes in A, the angular momentum J and the charge Q of a stationary, axisymmetric, charged, electrovacuum black hole under small perturbations. The black hole uniqueness theorems tell us that such a black hole must belong to the Kerr-Neumann family. The first law states that under a linearised perturbation to the Kerr-Neumann solution, the variation of the parameters satisfies,

$$\delta M = \frac{\kappa}{8\pi}\delta A + \Omega\delta J + \Phi\delta Q\,, \tag{8.2}$$

where Ω is the angular velocity of the black hole and Φ is the difference in electrostatic potential between the horizon and infinity. In fact, Wald and Sudarsky [126, 127] have shown that the first law holds also for more general diffeomorphism covariant theories of gravity in which case the quantities such as M and J are the conserved charges of appropriate Killing vector fields of the spacetime.

We note that there are two distinct viewpoints one can take concerning the first law [128]. One is the "physical states" viewpoint, which regards the first law as describing actual tiny physical perturbations to a given physical black hole [129], which subsequently settles down to another physical black hole described by parameters that are small changes from the original ones. The viewpoint in [126] is a more general "equilibrium states" viewpoint, being that the first law describes variations of the parameters characterizing a family of black hole solutions of interest.

To cast the first law in more familiar form, we make the identifications $M \leftrightarrow E$, $\frac{\kappa}{2\pi} \leftrightarrow T$ and $A/4 \leftrightarrow S$ between the black hole variables and their associated thermodynamic quantities. Eqn. (8.2) thus reads,

$$\delta E = T\delta S + \Omega\delta J + \Phi\delta Q\,, \tag{8.3}$$

which is the usual form of the first law, with $\Omega\delta J + \Phi\delta Q$ being the "work terms" for charged, rotating systems.

The first law together with Euler's theorem for homogeneous functions can be used to derive a *Smarr formula*, an expression for M in terms of A, J and Q. Euler's theorem states that if a function $f(x, y, z, ...)$ satisfies the scaling relation $f(\alpha^p x, \alpha^q y, \alpha^r z, ...) = \alpha^s f(x, y, z, ...)$, then the function and its partial derivatives satisfy the relation

$$sf(x, y, z, ...) = p\frac{\partial f}{\partial x}x + q\frac{\partial f}{\partial y}y + r\frac{\partial f}{\partial z}z + \dots\,. \tag{8.4}$$

Since the Kerr-Neumann solution is fully specified by three parameters, we can treat $M = M(A, J, Q)$. Under a change in length scale ℓ, each variable will scale according to their length dimensions, with $M \propto \ell$, $A \propto \ell^2$, $J \propto \ell^2$ and $Q \propto \ell$. Therefore we have a scaling relation for M under $\ell \to \alpha\ell$ given by $M(\alpha^2 A, \alpha^2 J, \alpha Q) = \alpha M(A, J, Q)$. Using the Euler's theorem and the first law then gives us the Smarr formula for Kerr-Neumann black holes:

$$M = 2\frac{\kappa}{8\pi}A + 2\Omega J + \Phi Q\,. \tag{8.5}$$

Second law

The second law is also known as the Hawking area theorem. It states that the area of a black hole can never decrease provided that the null energy condition is satisfied and the spacetime is strongly asymptotically predictable. In thermodynamic terms, this is the statement that the entropy of isolated systems cannot decrease.

Third Law

Finally, the third law states that it is impossible to reduce the temperature of a black hole to zero in any physical processes.

8.2 Extended phase space for AdS black holes

In the previous section, we have reviewed the laws of black hole thermodynamics in the usual Einstein-Maxwell theory. In this section, we consider the addition of a negative cosmological constant Λ and the resulting Anti-deSitter (AdS) black holes.

First law for AdS black holes

By treating Λ as a variable, Kastor, Ray and Traschen [38] derived a first law for static AdS black holes in analogy to the calculation done in [127]. The result they obtained (for uncharged, non-rotating AdS black holes) was

$$\delta M = \frac{\kappa}{8\pi}\delta A + \frac{\Theta}{8\pi}\delta\Lambda\,, \tag{8.6}$$

where Θ is given by a boundary integral of some geometric quantities, which is unimportant for us at the moment. The authors pointed out that since the addition of the cosmological constant into the Einstein's field equations can be interpreted as adding a perfect fluid energy momentum tensor with pressure

$$P = -\frac{\Lambda}{8\pi}\,,$$

we should interpret Λ as being related to the thermodynamic pressure P according to the above equation. The thermodynamic conjugate variable to P, $-\Theta$, which has the dimensions of volume, should thus be interpreted as the thermodynamic volume, $V \leftrightarrow -\Theta$. With these identifications, $\frac{\Theta}{8\pi} d\Lambda = V\delta P$. As a result, Eqn. (8.6) suggests that the mass of the black hole is actually its thermodynamic enthalpy, $H = E + pV$, and the equation itself is once again the enthalpy version of the thermodynamic first law,

$$\delta H = T\delta S + V\delta P\,. \tag{8.7}$$

We have thus extended the thermodynamic phase space of black holes by the (P, V) variables by considering a varying Λ.

In the case of rotating and charged AdS black holes, the first law becomes

$$\delta M = T\delta S + \Omega\delta J + \Phi\delta Q + V\delta P\,. \tag{8.8}$$

Addition of $V\delta P$ term to the first law allows for a scaling derivation of the Smarr formula of these black holes. Noting that $P \propto \Lambda \propto \ell^{-2}$, Euler's formula can be applied as before giving

$$M = 2\frac{\kappa}{8\pi}A + 2\Omega J + \Phi Q - 2PV\,. \tag{8.9}$$

Interpreting the thermodynamic volume

The thermodynamic volume of a black hole is given by its geometric volume in certain simple examples such as the Schwarzchild black hole, but in general, it differs from the geometric volume. In [130], it was conjectured that black holes satisfy the *reverse isoperimetric inequality*

$$\mathcal{R} = \left(\frac{(D-1)V}{\Omega_{D-2}}\right)^{\frac{1}{D-1}} \left(\frac{\Omega_{D-2}}{\mathcal{A}}\right)^{\frac{1}{D-2}} \geq 1 \tag{8.10}$$

for a $D-$dimensional spacetime. In this expression, Ω_{D-2} is the dimensionless surface area of the unit ball in $D-1$ dimensions and $\mathcal{A}$ is the surface area of the black hole horizon.

The conjecture was motivated by the observation at the time that all known black holes seemed to respect the inequality (8.10). Since $\mathcal{A}$ is proportional to the entropy of the black hole, Eq. (8.10) is an inequality between the thermodynamic volume and entropy of the black hole. When the inequality is saturated, a black hole of a given thermodynamic volume is interpreted to have attained its maximal possible entropy.

Since then, the isoperimetric ratio $\mathcal{R}$ of various black hole families have been studied, and some were found to violate this inequality [131, 132, 133, 134, 135, 136, 137, 138, 139]. Such black holes have come to be called *super-entropic*, since they have more entropy than the relation (8.10) would admit. In the next chapter, we shall see that there exists charged, slowly accelerating AdS black holes which are "mini-entropic".

8.2.1 Phase transitions

As mentioned in the beginning of this chapter, the thermodynamic behaviour of black holes is quantum origin, but we do not have a quantum theory to explain the microscopic degrees of freedoms involved. However, if we believe in the above identification of thermodynamic variables of black holes, then we can formally study other thermodynamic properties of the black holes using these identifications. In particular, we can study the possible phase transitions of black holes implied by (the relationship between) their thermodynamic variables.

One way to look for phase transitions of a thermodynamic system is by looking at the (Gibb's) free energy

$$F \equiv M - TS \tag{8.11}$$

of the system. At any fixed T, P, the configuration minimising F is thermodynamically favoured. A phase transition occurs when there is a discontinuity in the system variables (e.g., entropy, volume etc.) of the $F-$minimising configurations. To make things clearer, we illustrate this now for charged AdS black holes.

VDW-like transitions of charged AdS black holes

The hallmark phase transitions of charged and rotating AdS black holes is a small-to-large transition similar to the liquid-to-gas transition of Van der Waals fluids. This was studied in detail in [39]. This phase transition is heralded by the *swallowtail* $F-T$ diagram. Some example swallowtail diagrams are displayed in fig. 8.1 for $Q = 1$ AdS black holes at various pressures.

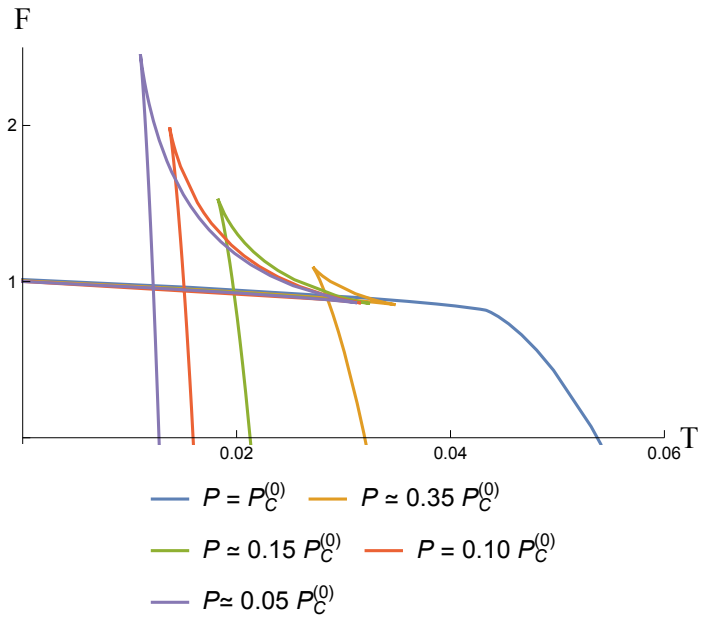

Figure 8.1: **Swallowtails.** This figure shows plots of free energy as a function of temperature for charged ($Q = 1$) AdS black holes at various pressures, measured in terms of the critical pressure $P_c^{(0)}$ (blue). For $P < P_c^{(0)}$ (purple, red, green, yellow), the curves take on a swallowtail shape, signifying first order phase transitions.

For pressures below a critical pressure, $P < P_c^{(0)}$, the free energy of the system exhibits *swallowtail behaviour*, characteristic of first order phase transitions. Let us examine the structures of the curves at different pressures: the curve is smooth for $P > P_c^{(0)}$, develops a kink at $P = P_c^{(0)}$, and then a swallowtail for $P < P_c^{(0)}$, which grows in size as pressure further decreases. Each swallowtail has two cusps and one self-intersection point. As we move along any given swallowtail beginning from the left at $T = 0$ and following the curve rightwards to its first cusp, then left and upwards to its second cusp, and then rightwards again down the steeply negative slope, the radius of the black hole monotonically increases. Hence it has become conventional to call black holes lying on the part of the curve between $T = 0$ and the first cusp *small black holes*, those lying on on the steeply negative slope below the self-intersection point *large black holes* and any black holes in between as *intermediate black holes*. These represent the three thermodynamic phases of charged AdS black holes.

For temperatures between $T = 0$ and the temperature at the intersection, the free energy is minimised by the small black holes, making them the favoured configuration.

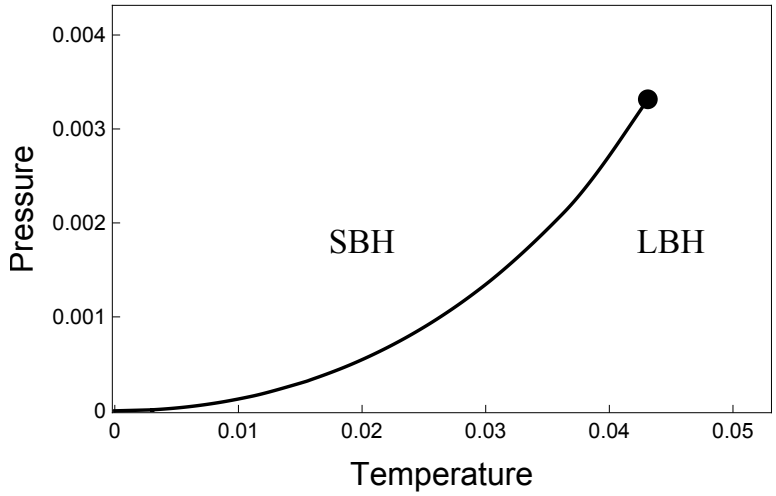

Figure 8.2: **Phase diagram of a charged AdS black hole.** The $P-T$ diagram of a charged AdS black hole is reminiscent of what happens for the liquid/gas phase transition. The coexistence line between small black hole (SBH) phase (analogous to the liquid phase) and large black hole (LBH) phase (analogous to the gas phase) emerges from the origin on one end and terminates at a critical point at $(T_c^{(0)}, P_c^{(0)})$ on the other end. The plot is made for $Q = 1$.

However the global minimum of the free energy experiences a discontinuity at the intersection, at which it is thermodynamically favourable for the small black hole to undergo a *first-order phase transition* to a large black hole.

The phase diagram of the charged AdS black holes is shown in Fig. 8.2. The curve on this $P-T$ plane is the coexistence line corresponding to the family of intersection points of the swallowtails in Fig. 8.1 at each pressure. Above the coexistence line, a small black hole is the preferred phase while below it a large black hole is the preferred phase. The coexistence line emanates from the origin and terminates at a *critical point*, characterized by the critical temperature and pressure

$$T_c^{(0)} = \frac{\sqrt{6}}{18\pi Q}\,, \qquad P_c^{(0)} = \frac{1}{96\pi Q^2}\,. \tag{8.12}$$

At this critical point the phase transition becomes second order and is characterized by the Ising universality class mean field theory critical exponents [39]. This phase transition of charged AdS black holes is reminiscent of the liquid/gas transition of Van der Waals fluids.

Remarkably since [39], Van der Waals-like behaviour has been observed for many rotating and/or charged AdS black holes in various spacetime dimensions and for various gravity theories. Although more complicated phase behaviour may occur (see [40] for a review), Van der Waals behaviour can be regarded as prototypical thermodynamic behaviour for AdS black holes in a canonical ensemble. For this reason it is rather instructive to find a departure from this prototypical behaviour and seek more complicated phase diagrams for AdS black holes. To this end the following features have been identified: reentrant phase transitions (RPT) [42], triple points analogous to that of water [43], isolated critical points [140, 141], and superfluid-like behaviour [142].

In the next chapter, we will find that acceleration of the black hole can bring about RPT. RPT refers to the scenario in which a system undergoes two or more phase transitions under the monotonic variation of a thermodynamic variable such that the final state is macroscopically similar to the initial state. RPT was first observed in a thermodynamic system in 1904 in a nicotine/water mixture and is commonly observed since then in multicomponent fluid systems [143]. In the context of black holes, RPT was first observed for four dimensional Born-Infled black holes in [41] and later examples include [42, 144, 145]. Besides RPT, acceleration also brings about a "snapping" of the swallowtail in the $F - T$ diagram where the branch of small black holes snaps back and joins smoothly to branch of intermediate black holes. This happens at another critical pressure which we denote as P_t. A zeroth order phase transition, where there is a jump in the free energy between the two phases, from small to intermediate black holes arises because of this snap. These novel features will be illustrated in greater details in the next chapter.

Chapter 9

Phase Transitions of Slowly Accelerating AdS Black Holes

In the previous chapter, we have seen that by treating the cosmological constant Λ as a thermodynamic variable, we arrive at a $V\delta P$ term in the first law of black hole thermodynamics. The addition of pressure gave rise to interesting phase behaviours for AdS black holes, with the Van der Waal's like phase transitions of charged AdS black holes being a representative example. In this chapter, we will see how the phase behaviour is altered when the black holes are accelerating.

This chapter is based on [6, 7].

9.1 Accelerating black holes

The history of accelerating black holes goes all the way back to the early days of general relativity to the discovery of the *C-metric* [146, 147]. This metric has played an important role for many developments in general relativity, has been rediscovered many times (see [148] for references), and is understood now to describe accelerating black holes. The C-metric yields an example of an exact radiative spacetime and was exploited to study radiative patterns in spacetimes with various asymptotics e.g. [149]. It has been used to study black hole nucleation in various backgrounds [150, 151], to provide the means for splitting a cosmic string [152, 153], and in a generalized form was used to construct 5-dimensional black rings [154].

Despite these interesting studies, it was only recently that the thermodynamic properties of these accelerating black holes were better understood. The effort had partly been hampered by the cosmic strings attached to the black holes, making them different from the usual *isolated* black holes solutions, and the generic presence of acceleration horizons in the spacetime. The acceleration horizons are usually at different temperatures from the black hole horizons, causing the black holes to *not* be in thermodynamic equilibrium. In addition, C-metric solutions possess unconventional asymptotic structures due in part to the cosmic strings that extend to infinity, making it difficult to correctly identify the asymptotically timelike Killing vector ∂_t with which mass should be defined. This has led to conflicting results in the literature [155, 156, 157, 158, 159, 160] for the thermodynamic mass of the black hole.

Surmounting these difficulties, the authors of [161, 162] described how to correctly normalise ∂_t to obtained a consistent thermodynamic description of *slowly* accelerating AdS black holes. These are black holes that do not possess acceleration horizons and the associated metric describes a single accelerated black hole in AdS space that is suspended on a cosmic string represented by a conical deficit on one of the polar axes. Since there is only one horizon (no acceleration or cosmological horizons are present in the limit of slow acceleration), the system has a unique temperature and its thermodynamics can be defined.

In the absence of charge and rotation, we might expect these slowly accelerating AdS black holes to undergo a Hawking-Page [163] phase transition just as other uncharged and non-rotating AdS black holes. However as already noted in [155, 156], transitions from black holes to pure thermal radiation is impossible in the canonical ensemble since there is a fixed conical deficit in the spacetime. We thus expect interesting phase transitions only when charge or rotation is added.

As we saw in the last chapter, the addition of charge brings about a small-to-large black hole phase transition which was also observed subsequently for rotating AdS black holes [42]. The key observation in [161, 162] is that the tension μ of the string, which causes the black hole to accelerate, can be treated as yet another thermodynamic quantity whose variations add a new work term to the first law which now reads

$$\delta M = T\delta S + \Omega\delta J + \Phi\delta Q + V\delta P - \lambda\delta\mu\,, \tag{9.1}$$

where λ is a conjugate thermodynamic quantity to the string tension μ, known as the thermodynamic length [156]. We shall study in detail in this chapter how the addition of this term affects the small-to-large black hole phase transition.

We begin in sec. 9.1.1 by reviewing the generalised C-metric which describes these black holes and presenting their thermodynamic variables in sec. 9.1.2 as they were derived in

[161, 162]. Next, we will move on to study the phase transitions of two subclasses of slowly accelerating AdS black holes namely, (i) charged, non-rotating black holes, and (ii) rotating, uncharged black holes. The analysis for each case proceeds via a standardised procedure: finding the admissible parameter space, studying the free-energy diagram and plotting the $P-T$ phase diagram. However, the phase transitions of the rotating case is slightly more involved than the charged case. We thus present the charged case first in sec. 9.2, which will lay the groundwork for studying the rotating case in sec. 9.3.

9.1.1 Generalised C-metric

The charged, rotating and accelerating AdS C-metric can be written as follows [164, 165, 166]

$$\begin{aligned} ds^2 &= \frac{1}{\Omega^2}\Bigg\{-\frac{f(r)}{\Sigma}\left[\frac{dt}{\alpha}-a\sin^2\theta\frac{d\phi}{K}\right]^2+\frac{\Sigma}{f(r)}dr^2+\frac{\Sigma\, r^2}{g(\theta)}d\theta^2 \\ &\quad +\frac{g(\theta)\,\sin^2\theta}{\Sigma\, r^2}\left[\frac{a\, dt}{\alpha}-(r^2+a^2)\frac{d\phi}{K}\right]^2\Bigg\}, \end{aligned} \tag{9.2}$$

$$F = dB\,, \quad B = -\frac{e}{\Sigma r}\left[\frac{dt}{\alpha}-asin^2\theta\frac{d\phi}{K}\right]+\Phi dt \tag{9.3}$$

where

$$\Phi = \frac{er_+}{(a^2+r_+^2)\alpha}\,. \tag{9.4}$$

In this gauge, the electrostatic potential vanishes on the black hole horizon. The other metric functions involved are given by

$$\begin{aligned} f &= (1-A^2r^2)\Big(1-\frac{2m}{r}+\frac{a^2+e^2}{r^2}\Big)+\frac{r^2+a^2}{l^2}\,, \\ g(\theta) &= 1+2mA\cos\theta+\Big(A^2(a^2+e^2)-\frac{a^2}{l^2}\Big)\cos^2\theta\,, \\ \Sigma &= 1+\frac{a^2}{r^2}\cos^2\theta\,, \quad \Omega = 1+Ar\cos\theta\,. \end{aligned} \tag{9.5}$$

with A being the acceleration parameter, $\Lambda=-3/l^2$ the cosmological constant, m the mass parameter, a the rotation parameter and e the charge parameter. The time coordinate has been rescaled by the parameter α,

$$\alpha = \frac{\sqrt{(\Xi+a^2/l^2)(1-A^2\ell^2\Xi)}}{1+a^2A^2}\,, \qquad \Xi = 1-\frac{a^2}{l^2}+A^2(e^2+a^2)\,, \tag{9.6}$$

in order to ensure a consistent variational principle and a correct normalization of the time-like Killing vector at infinity [161, 162]. The conformal factor Ω determines the boundary of the AdS spacetime, and the parameter K encodes information about the conical deficit on the south and north poles, so that $\phi \in [0, 2\pi]$.

The metric and gauge potential (9.2) satisfy the Einstein-Maxwell equations everywhere except along the polar axes $\theta = \theta_+ = 0$ and $\theta = \theta_- = \pi$, where there must exist a string of stress-energy in order to offset the conical deficit about these axes. This can be done by introducing cosmic strings whose tensions on the polar axes are

$$\mu_\pm = \frac{1}{4}\Big(1 - \frac{\Xi \pm 2mA}{K}\Big)\,, \tag{9.7}$$

and are related to the conical deficits, $\delta_\pm$ by $\delta_\pm = 8\pi\mu_\pm$. Thus we have the following range for the tensions:

$$\mu_\pm \in [0, 1/4)\,, \tag{9.8}$$

with the upper limit corresponding to a conical deficit of 2π. Defining further

$$K_\pm = g(\theta_\pm) = \Xi \pm 2mA\,, \tag{9.9}$$

we can by an appropriate choice of $K = K_+$ or $K = K_-$ respectively set either of μ_+ or μ_- to zero, but not both.

If the black hole has sufficiently slow acceleration (see discussion below) there will be a single (black hole) horizon. This constrains the parameter space and allows for a single temperature and consistent thermodynamics.

9.1.2 Thermodynamic variables

Let us first present the thermodynamic quantities associated with charged, rotating, slowly accelerating black holes [162]:

$$M = \frac{m(\Xi + a^2/l^2)(1 - A^2 l^2 \Xi)}{K \Xi \alpha (1 + a^2 A^2)}\,, \tag{9.10}$$

$$T = \frac{f'_+ \, r_+^2}{4\pi\alpha(r_+^2 + a^2)}\,, \quad S = \frac{\pi(r_+^2 + a^2)}{K(1 - A^2 r_+^2)}\,, \tag{9.11}$$

$$Q = \frac{e}{K}\,, \quad \Phi = \frac{e r_+}{(r_+^2 + a^2)\alpha}\,, \tag{9.12}$$

$$J = \frac{ma}{K^2}\,, \quad \Omega = \frac{aK}{\alpha(r_+^2 + a^2)} + \frac{aK(1 - A^2 l^2 \Xi)}{l^2 \Xi \alpha (1 + a^2 A^2)}\,, \tag{9.13}$$

$$P = \frac{3}{8\pi l^2}\,, V = \frac{4\pi}{3K\alpha}\Big[\frac{r_+(r_+^2 + a^2)}{(1 - A^2 r_+^2)^2} + \frac{m[a^2(1 - A^2 l^2 \Xi) + A^2 l^4 \Xi(\Xi + \frac{a^2}{l^2})]}{(1 + a^2 A^2)\Xi}\Big]\,, \tag{9.14}$$

$$\lambda_\pm = \frac{r_+}{\alpha(1 \pm A r_+)} - \frac{m}{\alpha}\frac{\big[\Xi + \frac{a^2}{l^2}(2 - A^2 l^2 \Xi)\big]}{(1 + a^2 A^2)\Xi^2} \mp \frac{A l^2 (\Xi + a^2/l^2)}{\alpha(1 + a^2 A^2)}\,. \tag{9.15}$$

They satisfy

$$\begin{aligned} \delta M &= T\delta S + \Phi \delta Q + \Omega \delta J + V \delta P - \lambda_+ \delta \mu_+ - \lambda_- \delta \mu_-\,, \\ M &= 2(TS + \Omega J - PV) + \Phi Q\,, \end{aligned} \tag{9.16}$$

which are respectively the first law and Smarr relation. The first law holds under a linear perturbation of the parameters $q_i \in \{m, l, a, e, A, K\}$ with $\delta M = \sum_i \frac{\partial M}{\partial q_i}\delta q_i$, etc. We note also that the $\lambda_\pm \mu_\pm$ terms do not enter the Smarr relation as $\mu_\pm$ is dimensionless. The necessity for introducing these last two work terms to the first law was first demonstrated in [156]. Examples of where string tensions do vary include "capture of cosmic string by a black hole" and an "axisymmetric merger" of two accelerating black holes, each carrying its own cosmic string.

In what follows we explicitly make the choice $K = K_+$, so that

$$\mu_+ = 0\,, \quad \mu = \mu_- = \frac{mA}{K_+}\,. \tag{9.17}$$

In other words, only one string (located at the south pole) pulls on the black hole, which is completely regular on the north pole. The first law then takes the form (9.1).

9.2 Charged, slowly accelerating AdS black holes

Now let us restrict attention to the charged case, setting $a = 0$ (hence $\Omega, J = 0$).

9.2.1 Parameter space

Before discussing the possible phase transitions, we must determine the admissible space of the parameters appearing in the metric (9.2) that ensure our problem is well-posed. Clearly, we have a number of conditions to impose: i) positivity of the function g over the range $\theta \in [0, \pi]$, ii) existence of a black hole in the bulk, and iii) validity of the derived thermodynamics. The latter entails working in the slow acceleration regime (9.23) and (9.26). This ensures that α is positive and that there is a single horizon whose temperature is given by its surface gravity.

In order to discuss these conditions, we introduce the new coordinates

$$x = \frac{1}{Ar}\,, \quad y = \cos\theta \tag{9.18}$$

so that the conformal boundary is situated at $x = -y$. We also consider the dimensionless quantities

$$\tilde{m} = mA\,, \quad \tilde{e} = eA\,, \quad \tilde{A} = Al\,, \quad \tilde{r} = r/l\,. \tag{9.19}$$

Using these variables, and the definition of μ, K, and Q, we find the following relations:

$$\tilde{A} = \frac{\tilde{e}(1-2\mu)}{(1+\tilde{e}^2)Q/l}\,, \quad \tilde{m} = \frac{\mu(1+\tilde{e}^2)}{1-2\mu}\,. \tag{9.20}$$

Signature of g.

In order to have the right metric signature $(-,+,+,+)$, we require $g > 0$ for $y \in [-1, 1]$. This yields

$$\tilde{m} < \begin{cases} \frac{1}{2}(1+\tilde{e}^2) & \text{for} \quad |\tilde{e}| < 1\,, \\ |\tilde{e}| & \text{for} \quad |\tilde{e}| > 1\,, \end{cases} \tag{9.21}$$

the boundaries of which give the black horizontal lines in Fig. 9.1.

Existence of a bulk black hole.

Demanding that the spacetime admits a black hole and not a naked singularity, we require that an horizon exists in the bulk, that is f has at least one root r_+ in the range $r \in (0, 1/A)$ preserving the signature for $r_+ < r < 1/A$.To find this we can appeal to the condition for an extremal black hole

$$f(\tilde{r}_e) = 0 = f'(\tilde{r}_e)\,, \tag{9.22}$$

or in other words, that f has a double root $r_+ = r_e$, corresponding to the coincidence of the inner and outer black hole horizons. Solving these two equations yields $\tilde{A} = \tilde{A}(\tilde{r}_e, \tilde{e})$ and $\tilde{m} = \tilde{m}(\tilde{r}_e, \tilde{e})$, which can be plotted parametrically in terms of $\tilde{r}_e$ for a fixed $\tilde{e}$. The resultant curve provides a lower bound for the existence of the black hole, and is displayed in Fig. 9.1b by the red line, denoting the extremal limit. Above this line, a black hole (with two horizons) is present, whereas no black hole exists below it.

Validity of thermodynamics.

To ensure that the thermodynamic quantities (9.10) are well defined, it is necessary to have $\alpha > 0$, which in turn imposes

$$1 - A^2\ell^2\Xi > 0\,, \tag{9.23}$$

or

$$\tilde{A} < \frac{1}{\sqrt{1+\tilde{e}^2}}\,. \tag{9.24}$$

The boundary is displayed in Fig. 9.1 by the vertical green lines.

On the other hand, the sufficient condition for the slow acceleration regime is that f does not develop any roots on the boundary (neither acceleration nor cosmological horizons are present [149]). Since the conformal boundary is situated at $x = -y$, the metric function f develops a root on the boundary when

$$f(x = -y) = 0 = f'(x = -y)\,, \tag{9.25}$$

for some $y \in [-1, 1]$. This yields the following relations:

$$\tilde{m} = \frac{y(1 + 2\tilde{e}^2y^2 - \tilde{e}^2)}{1 - 3y^2}\,, \quad \tilde{A} = \pm\frac{\sqrt{(1-\tilde{e}^2y^2)(1-3y^2)}}{(1-y^2)(1-\tilde{e}^2y^2)}\,. \tag{9.26}$$

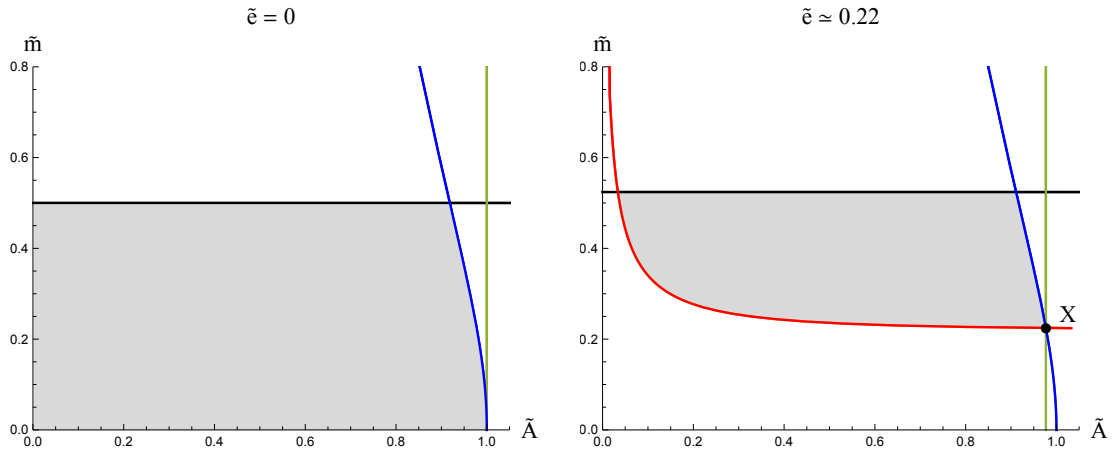

Figure 9.1: **Parameter space.** The admissible parameter space (denoted by shaded areas) is displayed in the $\tilde{m}$ vs. $\tilde{A}$ plane for fixed $\tilde{e} = 0$ (left) and $\tilde{e} \approx 0.22$ (right). Horizontal black curves outline the boundary of positive g. The red curve is the boundary for the existence of black holes in the bulk, with extremal black holes sitting on the curve. The blue curve forming the right boundary of the admissible region gives the no-acceleration horizon condition, and the green vertical line corresponds to $\alpha = 0$. A non-trivial point X is observed for $0 < \tilde{e} \leq \tilde{e}_M$. For $\tilde{e} = 0$ the analogous point is situated at the at $\tilde{A} = 1, \tilde{m} = 0$ corner of the left diagram, which corresponds to pure AdS spacetime.

The corresponding parameter space can be plotted parametrically, for $y \in [-1, 1]$; it corresponds to the blue curves forming the right-hand boundaries of the admissible regions in Fig. 9.1.

Note that the condition $\alpha > 0$, for which the thermodynamic quantities (9.10) are well defined functions, is weaker than the requirement of the slow acceleration regime—the blue curve cuts away an additional piece of the admissible region of the parameter space. One might suspect that the thermodynamic quantities in this removed region would correspond to the characteristics of a rapidly accelerating black hole. Even if so, the phase transition interpretation in this regime would be questionable as there are additional horizons present in the spacetime. We note, however, that a proposal [167] to treat additional horizons (in that case de Sitter) as 'independent thermodynamic systems' that do not apriori affect the phase transitions due to the black hole horizon has been recently put forward.

Point X and a summary of constraints.

The above constraints dictate the admissible parameter space in the dimensionless $(\tilde{A}, \tilde{m}, \tilde{e})$ plane. Two dimensional slices of this three-dimensional parameter space can easily be displayed; see Fig. 9.1 for two examples of $\tilde{e}$: $\tilde{e} = 0$ (left) and $\tilde{e} \approx 0.22$ (right). The full admissible parameter region is a union of such slices.

For a non-trivial $\tilde{e}$ we note the presence of a '*point X*' on each parameter slice, the only point where the $\alpha = 0$ line forms the boundary of the admissible region. As we shall see this point plays a crucial role for the existence of snapping swallowtails. Point X is characterized by the intersection of the following three curves: the $\alpha = 0$ curve, the extremal black hole curve, and the slow acceleration curve. Since the intersection of any two is sufficient for finding X, this point is (for example) given by

$$\alpha = 0\,, \quad f(\tilde{r}_e) = 0 = f'(\tilde{r}_e)\,, \tag{9.27}$$

which yields

$$\begin{aligned} \tilde{A} &= \frac{1}{\sqrt{1+\tilde{e}^2}}\,, \quad \tilde{m} = |\tilde{e}|\sqrt{1+\tilde{e}^2}\,, \\ \tilde{r}_e &= \frac{\sqrt{1+6\tilde{e}^2+5\tilde{e}^4}-1-\tilde{e}^2}{2|\tilde{e}|}\,. \end{aligned} \tag{9.28}$$

From the expressions of Q and μ, a black hole lying on this point must then have

$$Q = \frac{\tilde{e}\sqrt{1+\tilde{e}^2}}{1+\tilde{e}^2+2|\tilde{e}|\sqrt{1+\tilde{e}^2}}\,, \quad \mu = \frac{|Q|}{l}\,, \tag{9.29}$$

with the latter equivalent to a pressure which we call $P_t^{(Q)}$,

$$P_t^{(Q)} = \frac{3\mu^2}{8\pi Q^2}\,. \tag{9.30}$$

We shall see later that $P_t^{(Q)}$ corresponds to a critical pressure giving a novel lower end point to the coexistence line in the $P-T$ phase diagram.

As $\tilde{e}$ increases the point X 'travels upwards' and the admissible parameter region shrinks, until at a maximum value $\tilde{e}_M$ the whole parameter space shrinks to one point. This occurs when all boundary curves intersect, that is for

$$|\tilde{e}_M| = \frac{\sqrt{3}}{3}\,, \qquad \tilde{m}_M = \frac{2}{3} \qquad , \tilde{A} = \frac{\sqrt{3}}{2}\,. \tag{9.31}$$

For larger $\tilde{e}$ there is no physically admissible region. Hence $\tilde{e}$ is constrained to the range $\tilde{e} \in [0, \tilde{e}_M]$, which in turn implies that the mass $\tilde{m} \in [0, \tilde{m}_M]$. We note that these ranges imply that only the upper formula in (9.21) and the plus sign in (9.26) are applicable.

9.2.2 Mini-entropic black holes

The point X, characterized above by (9.27) and (9.28)–(9.30), would correspond, via (9.10)–(9.15), to a black hole of vanishing mass but finite radius and entropy, as well as infinite volume, and potential[1]. Of course, this object cannot actually be physically realized since X lies outside of the admissible region in parameter space (and thence the above stated thermodynamics does not apply). However it is possible to come arbitrarily close to it, for example following the slices of constant charge, pressure, and string tension, as displayed in Fig. 9.4 below.

Computing the isoperimetric ratio $\mathcal{R}$ (8.10),

$$\mathcal{R} = \left(\frac{(D-1)V}{\Omega_{D-2}}\right)^{\frac{1}{D-1}} \left(\frac{\Omega_{D-2}}{\mathcal{A}}\right)^{\frac{1}{D-2}} , \tag{9.32}$$

we see that it diverges as the point X is approached, where we have taken $\Omega_2 = 4\pi/K$ as the dimensionless volume of a 'unit ball', as determined by the r_+-independent metric conformal to the metric of a constant (t, r) hypersurface of Eqn.(9.2). From the perspective of the reverse isoperimetric inequality $\mathcal{R} \geq 1$ [130], black holes in the vicinity of X are *mini-entropic*: their volume diverges and their area is finite. This is in contrast to super-entropic black holes [131], whose entropy exceeds the maximum implied by the black hole volume ($\mathcal{R} < 1$).

9.2.3 Novel phase behaviours

As per usual, to uncover the thermodynamic behaviour of the system, we study the free energy, which is now also a function of the string tension μ,

$$F = M - TS = F(T, P, Q, \mu) . \tag{9.33}$$

Thermodynamic equilibrium corresponds to the global minimum of F. Non-analytic behaviour of this minimum indicates the presence of phase transitions.

[1]Note that the formula (9.28) admits a smooth limit $\tilde{e} \to 0$, in which case we recover $\tilde{A} = 1, \tilde{m} = 0 = \tilde{r}_e$, corresponding to empty AdS space.

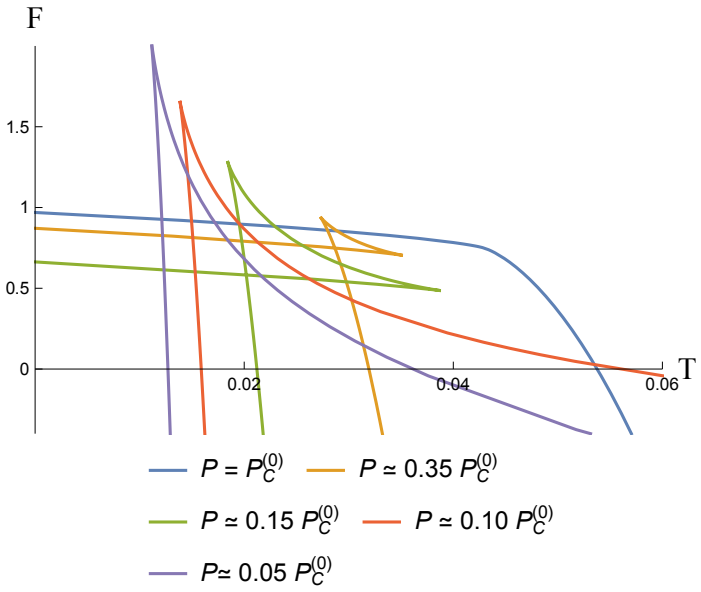

Figure 9.2: $F - T$ **diagram for charged accelerating black holes.** A plot of free energy as a function of temperature for accelerating charged black holes for various values of the pressure, measured in terms of $P_c^{(0)}$, with $\mu = 0.05$ and $Q = 1$; Whereas in the non-accelerating case (Fig.8.1) the swallowtails exist for arbitrary small pressures, the swallowtail disappears here for $P < P_t^{(Q)}$, see e.g. red curve where the swallowtail already snapped.

Snapping swallowtails

As discussed in the previous chapter, charged AdS black holes without acceleration exhibit Van der Waals-like phase behaviour [39]: for pressures $P < P_c^{(0)}$ one observes swallowtail behaviour of the free energy—corresponding to the first order small black hole/large black hole phase transition, as illustrated in Fig. 8.1. In the presence of acceleration the situation is much more interesting. As depicted in Fig. 9.2, for small tensions and pressures below a critical value $P_c \approx P_c^{(0)}$ the swallowtail behaviour is preserved. However, contrary to the non-accelerating case, the swallowtail ceases to exist for $P < P_t^{(Q)}$. Instead, as P decreases through $P_t^{(Q)}$, the swallowtail 'snaps': the small black hole branch disappears together with the extremal black hole, and re-appears as a new branch of unstable high temperature black holes (that are mini-entropic for sufficiently high temperatures). The resultant free energy diagram for $P < P_t^{(Q)}$ is reminiscent of that of the 'Schwarzschild-

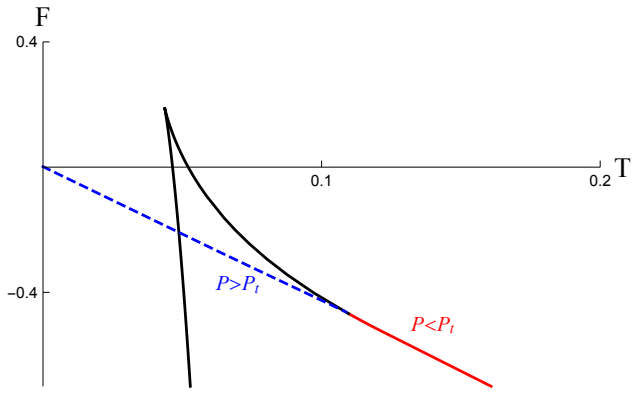

Figure 9.3: **Snapping swallowtail at $P \approx P_t^{(Q)}$.** We display the qualitative change of the behaviour of the free energy around $P \approx P_t^{(Q)}$ for $\mu = 0.1$ and $Q = 1$. The blue dashed curve together with the solid black curve show the behaviour of F for $P \gtrsim P_t^{(Q)}$ where the swallowtail is present. At $P_t^{(Q)}$ the swallowtail snaps, the blue dashed curve disappears and a new branch of black holes displayed by the red curve appears. The black holes on the dashed blue curve map to the black holes on the solid red curve in such a way that the cusp point remains invariant and the extremal black hole located on the blue curve at $T = 0$ maps to the (red curve) mini-entropic black hole at $T \to \infty$. At $P \lesssim P_t^{(Q)}$ we observe the free energy, reminiscent of that of the Schwarzschild-AdS black hole, given by a union of red and black curves.

AdS' black hole (see Fig. 9.3 for more details). We stress, however, that in this case no Hawking–Page transition can exist, as there is no radiation phase with non-trivial charge Q and non-trivial string tension μ.

To get an intuitive feeling as to why the swallowtail snaps, let us study the $P > P_t^{(Q)}$, $P = P_t^{(Q)}$, and $P < P_t^{(Q)}$ 'swallowtails' of the free energy from a perspective of the corresponding parameter space slicing. Each swallowtail is characterized by fixed μ and Q, and of course fixed pressure, and gives rise to a corresponding curve in the parameter space $(\tilde{m}, \tilde{A}, \tilde{e})$. In Fig. 9.4 we display the orthogonal projection of these curves (black arrows) onto a fixed $\tilde{e}$ plane. On one end such curves asymptote to $\tilde{A} = 0$ corresponding to black holes lying at the very bottom of the stable large black hole branch; on the other end they terminate either on an extremal black hole curve (dashed case), at the point X (solid), or on the slow acceleration blue curve (dot-dash). Note that each of these end points happen on a different $\tilde{e}$ slice but they are all projected onto the same plane in Fig. 9.4 for illustration.

When $P = P_t^{(Q)}$ (displayed in Fig. 9.4 by a solid black curve) the swallowtail terminates at the point X and represents the critical case[2]. For $P_t^{(Q)} < P < P_c$ the (dashed black) curve lies to the left of the critical slice and represents a true swallowtail, terminating on an extremal black hole curve at some value of $\tilde{e}$. On the other hand, if $P < P_t^{(Q)}$ the (dot-dash black) curve lies to the right of the critical curve and necessarily terminates on the slow acceleration boundary curve for some $\tilde{e}$. Of course, this corresponds to the already snapped swallowtail.

Summarizing, it is the 'crossing' of the point X in parameter space, together with the existence of the slow acceleration boundary, that is responsible for the swallowtail snapping.

Zeroth order phase transition & bicritical point

The snap of the swallowtail at $P = P_t^{(Q)}$ has the following rather interesting consequence illustrated in Fig. 9.5. As we lower the pressure through $P_t^{(Q)}$, the entire branch of stable small low temperature black holes (blue, dashed) present for $P \gtrsim P_t^{(Q)}$ disappears. Consequently for $P \lesssim P_t^{(Q)}$ there are no longer any black holes below T_0, with T_0 being the temperature of the upper cusp of the critical swallowtail. At the same time the global minimum of the free energy in between T_0 and T_t, 'jumps upwards' from the small black hole branch to the intermediate black hole branch, as schematically illustrated for a single black hole in Fig. 9.5. Here T_t is the temperature of the bottom intersection of the critical swallowtail.

In other words, in between T_0 and T_t we observe a *zeroth-order phase transition*, as the global minimum of the free energy experiences a finite jump across $P_t^{(Q)}$. Increasing the temperature from T_0, this jump gets smaller and smaller and finally disappears at $T = T_t$. Thus, we have a special point, at

$$(T_t, P_t^{(Q)}) \,, \tag{9.34}$$

where the coexistence line (see Fig. 9.6) of the zeroth order phase transition characterized by $P_t^{(Q)}$ and $T \in (T_0, T_t)$ terminates and joins the first order coexistence line of the small black hole/large black hole phase transition. We call this point the bicritical point.

[2]That this slice seems to lie beyond the admissible region is simply an artifact of displaying the 2d projections of the full 3d parameter space. Since these regions get bigger as $\tilde{e}$ decreases, all points on the slice actually belong to the admissible region.

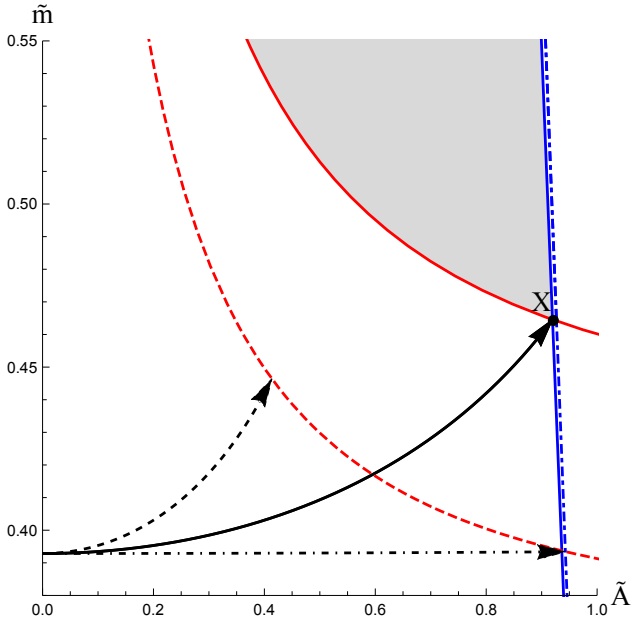

Figure 9.4: **Swallowtail slicing of the parameter space.** We display with black arrows projections of three different free energy "swallowtail" curves in the $(\tilde{m}, \tilde{A})$ parameter space for $\mu = 0.22$ and $Q = 1$, with the associated point X; the shaded region is the admissible region for the slice $\tilde{e} \approx 0.4272$, the plane on which the critical swallowtail intersects X. The solid black curve corresponds to this critical swallowtail which has $P = P_t^{(Q)}$. The dashed curve corresponds to $P > P_t^{(Q)}$: any such curve terminates on an extremal black hole curve denoted by the red dashed curve of some $\tilde{e}$ slice (for pressures $P < P_c$ this is a true swallowtail). The dot-dash curve characterizes $P < P_t^{(Q)}$ and terminates on a slow black hole curve denoted by dot-dash blue curve; such curves, which we call snapped swallowtails, display 'Schwarzschild-AdS'-like behaviours of the free energy.

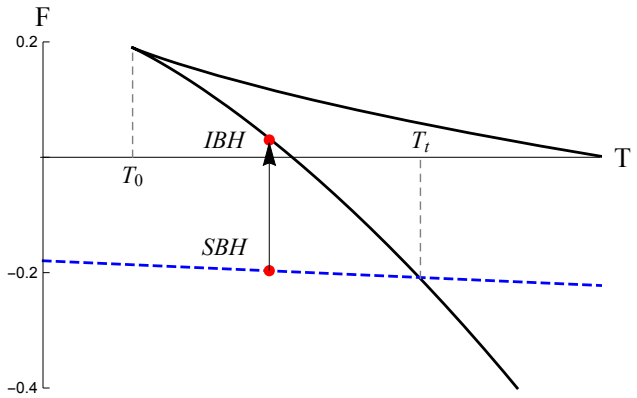

Figure 9.5: **Zeroth order phase transition.** This figure is a zoomed in version of Fig. 9.3. Due to the swallowtail snap at $P = P_t^{(Q)}$, the entire branch of stable low temperature black holes (blue dashed curve) disappears. This gives rise to a no black hole region to the left of $(T_0, P_t^{(Q)})$ on the $P - T$ phase diagram. As we transit from $P > P_t^{(Q)}$ to $P = P_t^{(Q)}$, the dashed blue branch of small black holes disappears; the global minimum of the free energy of black holes lying between T_0 and T_t, 'jumps upwards' from the small black hole branch to the intermediate black hole branch. An example of this jump is displayed in the figure by the red point.

9.2.4 Phase diagrams

Having understood the free energy, we can now plot the phase diagrams, displayed for various tensions in Fig. 9.6. Consider first a small string tension $\mu = 0.05$, Fig. 9.6a. Similar to the non-accelerating case the diagram features the first order phase transition coexistence line (displayed by the blue curve) and the critical point (solid circle) where the first order coexistence line terminates and the transition becomes second order. A novel feature, when compared to Fig. 8.2, is the existence of a bicritical point (empty circle) and the associated zeroth order phase transition (red dashed curve). We also observe the existence of a no black hole region caused by the fact that low temperature, slowly accelerating small black holes no longer exist below $P_t^{(Q)}$. Note that the situation is physically very different from the Hawking–Page transition [163], where the 'no black hole region' is replaced by a radiation phase with lower free energy. In our ensemble of fixed charge and fixed tension of the semi-infinite string, no such radiation phase exists. It remains to be seen whether some novel phase of solutions (preserving the ensemble conditions) may exist in this region and be thermodynamically preferred.

As the string tension μ increases to $\mu = 0.15$ in Fig. 9.6b, a region of RPT emerges.

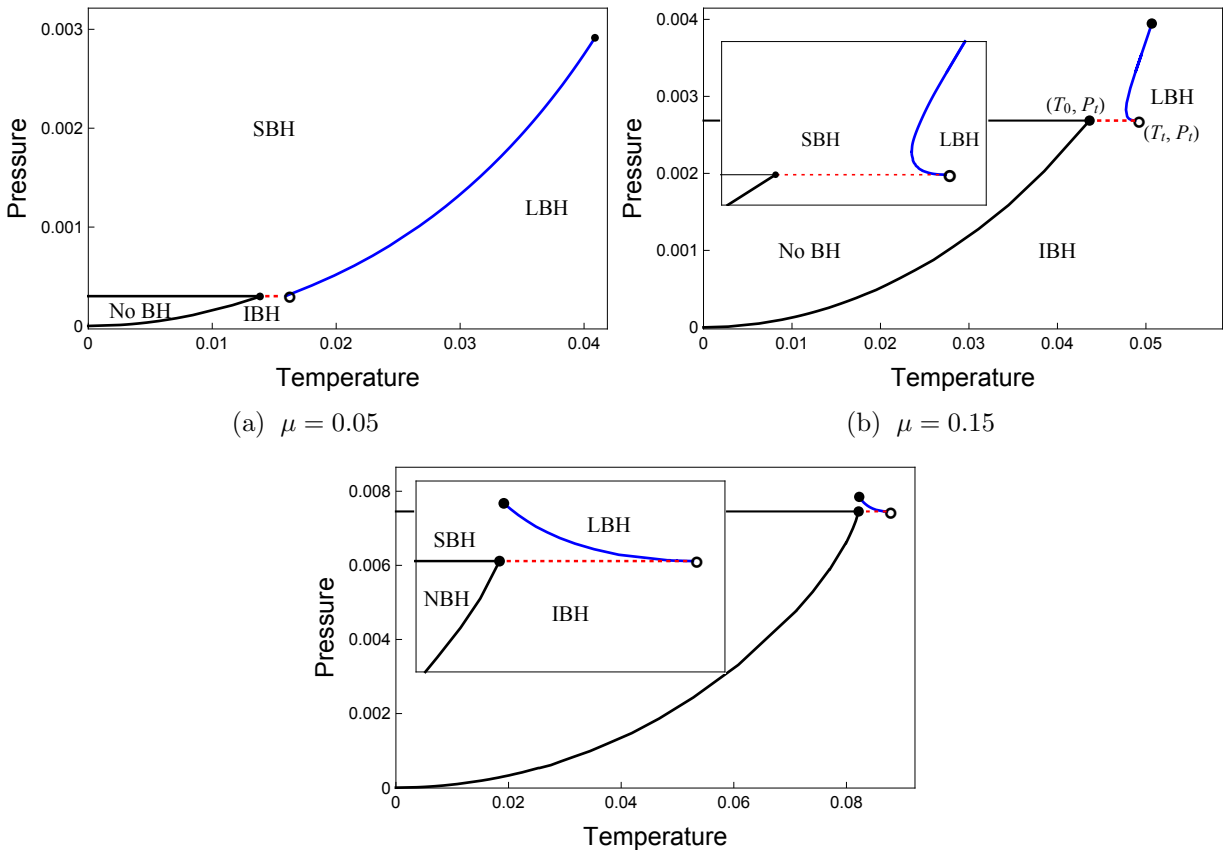

(a) $\mu = 0.05$

(b) $\mu = 0.15$

(c) $\mu \approx 0.25$

Figure 9.6: **Phase diagrams.** $P - T$ diagrams are displayed for various string tensions. The blue curve indicates the coexistence line of the first order phase transition. It terminates at a critical point (denoted by a black solid circle) on one end and at a bicritical point at $(T_t, P_t^{(Q)})$ (denoted by empty circle) on the other end. A zeroth-order phase transition coexistence curve emanates from the bicritical point, indicated by the dotted red line. The black curves bound a region for which no slowly accelerating black holes exist, the 'no black hole' region. The inset of the second diagram clearly illustrates the presence of a reentrant phase transition with pressure as the control parameter. Note also the slope of the blue coexistence line in the third diagram, which is 'opposite to' what happens for the non-accelerated case.

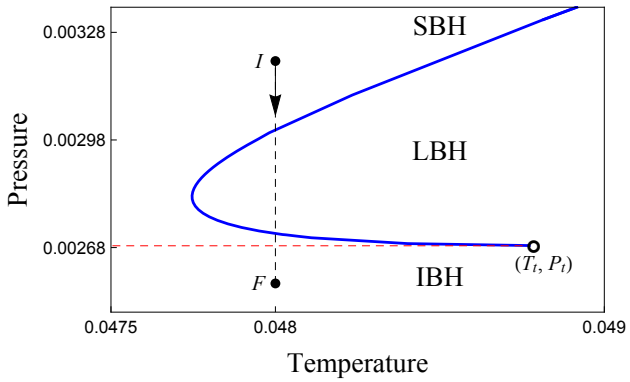

Figure 9.7: **Reentrant phase transition.** The inset of Fig. 9.6b, reproduced here, displays the pressure driven reentrant phase transition present for $\mu = 0.15$. Namely, as we follow the black dashed line from the initial point I of high pressure, to the final point F of low pressure, we cross twice the first order coexistence line (blue curve) and once the zeroth order coexistence line (denoted by dashed red curve), undergoing a reentrant phase transition from SBH to LBH back to SBH and finally to IBH. This is a first example where the reentrance is observed for black holes with the pressure as a control parameter.

At this intermediate μ the co-existence line of the first order phase transitions becomes double-valued, indicating the presence of a pressure driven RPT. This is shown in greater detail in Fig. 9.7. As we follow the black dashed line from the initial point I of high pressure, to the final point F of low pressure, we cross twice the first order coexistence line (blue curve) and once the zeroth order coexistence line (denoted by dashed red curve), undergoing a reentrant phase transition from SBH to LBH back to SBH and finally to IBH. This is the first example where reentrance is observed for black holes with the pressure as the control parameter.

Finally, for sufficiently large tensions, $\mu \approx 1/4$, the slope of the whole coexistence line becomes negative, as pressure decreases from P_c, temperature increases instead of decreases along the line, see Fig. 9.6c. This transition is very different from that of the liquid/gas phase transition.

9.2.5 Summary for charged, slowly accelerating black holes

Let us now summarise the phase behaviour of charged, slowly accelerating black holes. We have found that whereas the high pressure behaviour resembles that of the non-accelerating case, there exists a second critical point $P = P_t^{(Q)}$ at low pressures where the *swallowtail*

snaps. We have provided an intuitive explanation of this by looking at how the swallowtail plots cut the parameter space. We can understand the snapping of the swallowtail as a result of the existence of a critical slice through the *point* X in the parameter space, together with the existence of the slow acceleration boundary.

The coexistence line of the first order phase transition thus terminates at $P_t^{(Q)}$, where it is joined to a *zeroth order coexistence line*, across which we find a small to intermediate black hole phase transition. We refer to the point where the two coexistence lines intersect as a bicritical point, and denote it by $(P_t^{(Q)}, T_t)$.

So far in our investigations we have concentrated on the case when only one (south pole) string is present and the north pole axis is regular, in which case the critical pressure $P_t^{(Q)}$ is given by formula (9.30). If both strings were present, the behaviour we have discovered would remain qualitatively the same, with the critical pressure instead given by

$$P_t^{(Q)} = \frac{3(\mu_+ - \mu_-)^2}{8\pi Q^2} \,. \tag{9.35}$$

Since it is the difference of the two string tensions that causes the black hole to accelerate, we see that the existence of $P_t^{(Q)}$ is immediately linked to the black hole acceleration.

We also found a new form of a *reentrant phase transition* from the double-valued coexistence curve, as well as a *no black hole region* in the $P-T$ plane. This is the first example of a black hole RPT in which pressure is the parameter that montonically changes as we shift from one phase to another and then back to the first.

Finally, we have discovered the existence of (charged) *mini-entropic black holes*, whose temperature, electrostatic potential, and volume become unboundedly large whilst their entropy, horizon size, and mass remain finite, with the latter approaching zero. The physical properties of these objects remain to be understood.

Let us now switch off the charge parameter e, and consider instead the case of non-zero a, corresponding to rotating, slowly accelerating AdS black holes.

9.3 Rotating, slowly accelerating AdS black holes

We have seen in the previous section that the snapping swallowtail heralds several new phenomena, namely (i) a termination of first order phase transitions, (ii) the emergence of a 'no black hole' region in the $P-T$ plane and (iii) the phenomenon of zeroth order phase

transitions [42], all happening at the single pressure at which the swallowtail snaps. The characteristics of the 'snapping point' were further analyzed subsequently in [168].

In this section we will see that all of the above phenomena observed for the charged case remain present for the rotating case but with a number of subtle and interesting differences. Namely, unlike the charged case, 'point X' no longer belongs to the admissible parameter space and consequently slowly accelerating rotating uncharged mini-entropic black holes do not exist. Although the swallow tail still snaps at [168]

$$P_t^{(J)} = \frac{3(1-2\mu)^2}{8\pi|J|}\frac{x_0\sqrt{2x_0+1}}{2}\,, \tag{9.36}$$

where J is the angular momentum of the black hole, and

$$x_0 = \frac{\sqrt{1+12C^2}-1}{3}\,, \quad C = \frac{\mu}{1-2\mu}\,, \tag{9.37}$$

this happens for black holes outside of the slowly accelerating regime. Consequently, instead of one transition pressure $P_t^{(Q)}$, we now observe 3 important critical pressures: the pressure P_{nbh} at which the 'no black hole' region appears, the pressure $P_0 < P_{nbh}$ where the zeroth order phase transition starts, and the pressure $P_f < P_0$ at which zeroth and first order phase transitions co-terminate. In this sense the presence of rotation provides a "fine splitting" of the transition pressure P_t.

9.3.1 Parameter space

As before, let us first probe the admissible parameter space for which slowly accelerating rotating black holes exist and compare it to the parameter space of the charged case.

As we have already fixed the parameter K by imposing (9.17), our family of rotating black holes is characterized by the 4 parameters $\{a, A, l, m\}$. To simplify the analysis we shall use the dimensionless parameters $\tilde{A}$ and $\tilde{m}$ defined as before, and define also the dimensionless rotation parameter

$$\tilde{a} = aA\,. \tag{9.38}$$

The same constraints as that in sec. 9.2.1 dictate the admissible parameter space in the dimensionless $(\tilde{A}, \tilde{m}, \tilde{a})$ plane. Two dimensional slices of this three-dimensional parameter space can easily be displayed; see Fig. 9.8 a for a choice of $\tilde{a} = 0.2$; the full admissible parameter region would be a union over $\tilde{a}$ of such slices. Let us revisit the necessary constraints as presented in 9.2.1, this time for rotating black holes.

Signature of g.

The first condition $g > 0$ now yields

$$\tilde{m} < \frac{1}{2}\Xi = \frac{1}{2} + \frac{1}{2}\left(\tilde{a}^2 - \frac{\tilde{a}^2}{\tilde{A}^2}\right), \tag{9.39}$$

the boundaries of which yield the black curve in the left diagram in Fig. 9.8.

Existence of a bulk black hole.

Second, for a black hole to exist within the boundaries of the spacetime, we require

$$f(r_+) = 0 = f'(r_+), \tag{9.40}$$

which yields complicated equations for $\tilde{A} = \tilde{A}(\tilde{r}_+, \tilde{a})$ and $\tilde{m} = \tilde{m}(\tilde{r}_+, \tilde{a})$. These can be plotted parametrically, using $\tilde{r}_+ = r_+/l$ as the parameter, and are displayed in the left diagram in Fig. 9.8 as a red curve. Solutions on this curve represent extremal black holes while those above this curve represent non-extremal bulk black holes.

Validity of thermodynamics

The last condition requires that there are no additional horizons in the bulk besides the black hole horizon. We thus have to solve a condition for the existence of an extremal horizon on the boundary, which is $f(x = -y) = 0 = f'(x = -y)$ (Eqn. (9.22)). This yields the following equations:

$$\begin{aligned} \tilde{m} &= \frac{y(1+\tilde{a}^2y^2)^2}{1-y^2(\tilde{a}^2+3)-\tilde{a}^2y^4}, \\ \tilde{A} &= \frac{\sqrt{1-y^2(\tilde{a}^2+3)-\tilde{a}^2y^4}}{(1-y^2)\sqrt{1-\tilde{a}^2y^2}}, \end{aligned} \tag{9.41}$$

which again can be plotted parameterically, with $y \in [-1, 1]$ now playing the role of a parameter. The result is displayed in the left diagram in Fig. 9.8 by the blue curve. The spacetimes with additional (acceleration and cosmological) horizons are to the right of this curve and are excluded by the slow acceleration condition.

Putting everything together, it is now obvious that the parameter space of the rotating black holes (Fig. 9.8a) is qualitatively different from the parameter space of the charged

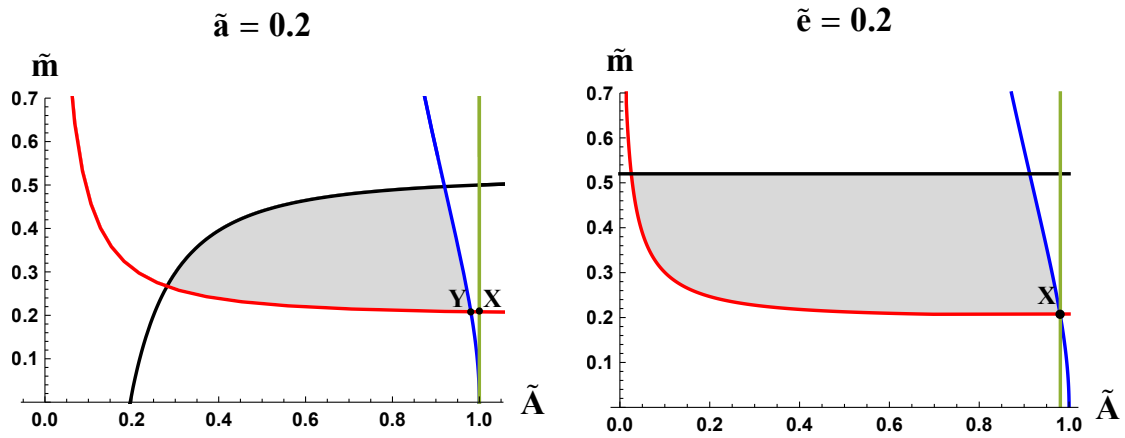

Figure 9.8: **Admissible parameter space comparison.** The admissible parameter space for rotating (left) and charged (right) slowly accelerating black holes is displayed by the shaded region in the $\tilde{A} - \tilde{m}$ plane. The left figure, displayed for fixed $\tilde{a} = 0.2$, summarizes the constraints discussed in the main text as follows: the black, red, and blue curves respectively correspond to the boundaries of the Lorentzian metric signature, the existence of a bulk black hole, and the absence of an acceleration horizon; the green line displays $\alpha = 0$. The right figure displays the analogous curves for the charged case with a fixed dimensionless charge parameter $\tilde{e} = eA = 0.2$. While in the charged case the point X lies at the intersection of three (red, blue, and green) boundary curves, rotation removes this degeneracy and we now observe two salient intersection points: X and Y.

black holes (Fig. 9.8b). While in the charged case the point X lies at the intersection of three (red, blue, and green) boundary curves, rotation removes this degeneracy and we now observe two salient intersection points: X and Y. The point X, at the intersection of green and red curves, corresponds to $P_t^{(J)}$ given by (9.36), or

$$P_t^{(J)} \approx \frac{3\mu^2}{8\pi|J|}\Big(1 - \mu^2 + O(\mu^4)\Big)\,. \tag{9.42}$$

It lies strictly outside the admissible region. This prevents the formation of mini-entropic black holes, which exist in the vicinity of the point X displayed in Fig. 9.8, and whose thermodynamic volume grow unbounded whilst their entropies remain finite.

The point Y, located at the intersection of blue and red curves, marks the emergence of

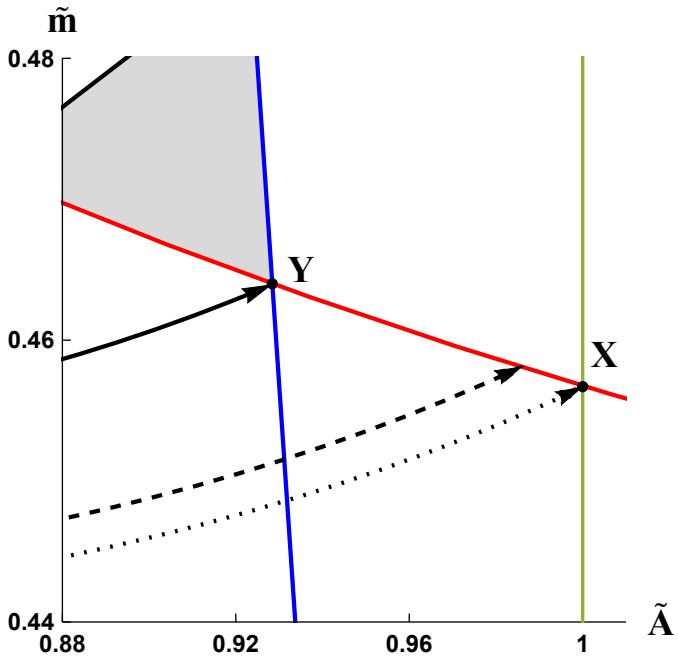

Figure 9.9: **Swallowtail slicing of the parameter space.** The arrows display the projections of three important swallowtails (with $J = 1$ and $\mu = 0.24$) into a single $\tilde{a} = 0.4$ plane of the parameter space near the points X and Y. The solid black arrow corresponds to $P = P_{nbh} \approx 0.00688$ and terminates at the point Y. On the $F-T$ diagram, this corresponds to a curve whose extremal black hole ($T = 0$ point) lies just within the admissible parameter space. Note that the arrow *does* lie within the admissible parameter space for all $\tilde{a} \in [0, 0.4]$. This is not obvious in the figure because the admissible region shrinks with increasing $\tilde{a}$. The dashed arrow displays the swallowtail with $P = P_0 \approx 0.0062$. Unlike the previous curve, it does not lie fully within the parameter space (and rather terminates at the slow acceleration boundary). It corresponds to a swallowtail similar to the one shown on Fig 9.12, but with the red point lying directly below the free-energy peak of the swallowtail. The dotted arrow is for $P = P_t^{(J)} \approx 0.00601$ and reaches the point X. Like the dashed case, it lies partly outside of the admissible region. Strictly speaking, swallowtails with different pressures terminate at different $\tilde{a}$ planes. However, for points X and Y the variation of $\tilde{a}$ is of the order $O(\mu^5)$ and can be in our figure neglected.

the no black hole region and occurs at P_{nbh}. At this pressure, the metric function develops two double roots—corresponding to the extremal black hole in the bulk and an extremal horizon at the boundary, giving

$$\tilde{m} = \tilde{a} + \tilde{a}^3 \,, \quad \tilde{A} = \frac{1}{\sqrt{1+\tilde{a}^2}} \,. \tag{9.43}$$

Equating these with (9.46) below yields

$$P_{nbh} = \frac{3\mu^2}{8\pi|J|} \,. \tag{9.44}$$

For small μ, this is very close to the transition pressure (9.36), as is clear from (9.42). Note also that two important pressures P_0 and P_f necessarily lie in between these two pressures; we shall discuss these in the next section.

An additional piece of information is encoded in how the μ, J , $P =$ const. swallowtail curves cut through the parameter space. To display these, we use the following 3 equations:

$$J = \frac{3\tilde{a}\tilde{m}}{8\pi P \tilde{A}^2 K_+^2} \,, \quad \mu = \frac{\tilde{m}}{K_+} \,, \quad K_+ = 1 - \frac{\tilde{a}^2}{\tilde{A}^2} + \tilde{a}^2 + 2\tilde{m} \,, \tag{9.45}$$

to find

$$\begin{aligned} \tilde{m} &= \frac{(1+\tilde{a}^2)\mu^2}{8\pi\tilde{a}PJ/3 + \mu - 2\mu^2} \,, \\ \tilde{A} &= \frac{\sqrt{\tilde{a}^2 + 3\mu\tilde{a}(1-2\mu)/(8\pi PJ)}}{\sqrt{1+\tilde{a}^2}} \,, \end{aligned} \tag{9.46}$$

which can be plotted parameterically over $\tilde{a}$. For illustration, the projections of the three important swallowtails at $P_{nbh}, P_0 \approx P_f$, and $P_t^{(J)}$ for $J = 1$ and $\mu = 0.24$ are displayed in Fig. 9.9. The fact that the latter two terminate at the slow acceleration boundary has far reaching consequences for the phase transitions, which we turn to now.

9.3.2 Phase Transitions

In this section, we show that although similar in many aspects, the phase behaviour of rotating black holes is richer than in the charged case. Perhaps most intriguing is the phenomenon of 'fine splitting' of the transition pressure. In our considerations below, we set $J = 1$ and plot the corresponding $P - T$ phase diagrams for various string tensions μ, see Figs. 9.10 and 9.11.

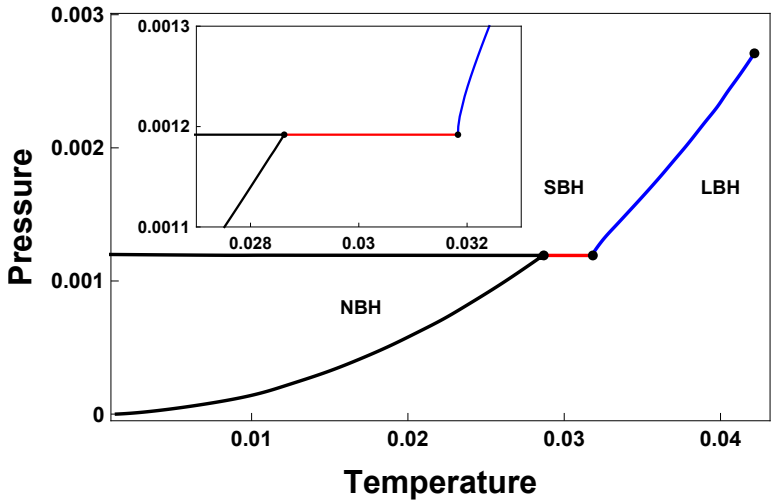

Figure 9.10: **Phase diagram:** $\mu = 0.1$**.** For small tensions, the $P - T$ phase diagram is similar to the charged case, with termination of the first order coexistence line (blue), the presence of a zeroth order transition line (red) and a 'no black hole' (NBH) region delimited by the black lines. The first order transition separates small black hole (SBH) and large black hole (LBH) solutions. The inset shows an enlarged view near $P = P_f$, where the first order phase transition terminates. At this μ, we have $P_0 \approx P_f \approx P_{nbh} \approx 0.001194$.

Fine Splitting of Transition Pressures

For small tensions, the phase diagram is qualitatively similar to that of the charged accelerating black hole, compare Fig. 9.10 with Fig. 9.6a. Namely, we observe a first order phase transition (displayed by the blue curve), which terminates at a critical point at $P = P_c$ on one end and at a termination point at $P = P_f$ on the other end. (Whereas the critical point at P_c is a standard feature of many black holes, the existence of the termination point seems unique for accelerating black holes.) From this termination point a zeroth-order phase transition coexistence line (displayed by the red curve) emerges and eventually ends at $P = P_0$ on the boundary (black curve) of the no black hole region, which appears at $P = P_{nbh}$.

In the charged case these pressures are in fact exactly equal, given by the transition pressure $P_t^{(Q)}$, (9.30). However, in the rotating case this is only true approximately and the situation is in fact much more subtle. Namely, these pressures order as follows:

$$P_{nbh} \gtrsim P_0 \gtrsim P_f \gtrsim P_t^{(J)} \,, \tag{9.47}$$

and though they seem indistinguishable in Fig. 9.10, the distinction is more apparent for bigger string tensions μ, as shown in Fig. 9.11 and its inset.

The origin of this fine splitting can be traced to the qualitatively different parameter space in the rotating case, and in particular to the different behaviour of the slow acceleration bound. In the charged case, such a bound does not play any role in equilibrium thermodynamics: it is completely absent for $P > P_t^{(Q)}$, and below $P_t^{(Q)}$ it only removes small unstable black holes in the upper branch of the free energy that do not correspond to the global minimum. In the rotating case, however, this bound can occur in the stable branch and thus affects the thermodynamic behaviour, as illustrated in Fig. 9.12.

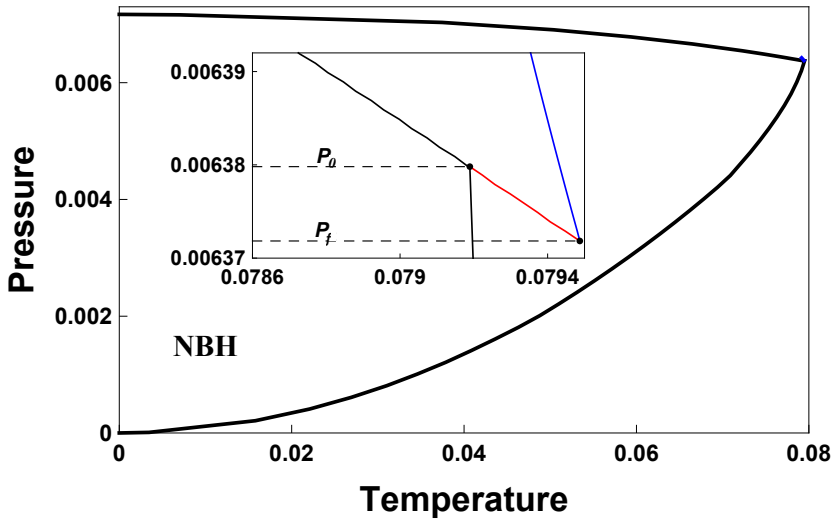

Figure 9.11: **Phase diagram: $\mu = 0.245$.** For this μ, the $P - T$ diagram clearly illustrates the fine splitting of the transition pressures. Comparing with the $\mu = 0.1$ case, the first order phase transition and zeroth order phase transition curves shrank considerably. However, the inset shows that the zeroth order transition line has a non-trivial negative gradient, and the gradient of the first order phase transition went from positive to negative. For this tension we have $P_{nbh} \approx 0.007165, P_0 \approx 0.00637981, P_f \approx 0.00637184$, and $P_t^{(J)} \approx 0.006215$, all apparently distinct.

The appearance of a no black hole region, at P_{nbh}, corresponds to the pressure at which the last slowly accelerating black hole (displayed by a red dot in Fig. 9.12) coincides with an extremal black hole on the lower branch of the swallowtail. As pressure decreases,

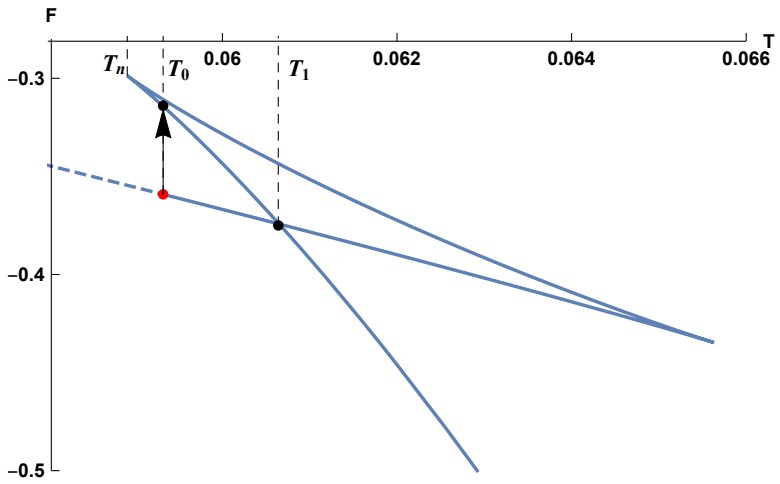

Figure 9.12: **Slow acceleration bound and its effect on phase transitions.** The $F-T$ diagram shows a swallowtail at a pressure $P_f < P < P_0$. The 'last' slowly accelerating black hole is highlighted by a red dot – the part of the lower temperature branch of black holes (that develop extra horizons) denoted by a dashed curve is removed. This is the origin of the temperature driven reentrant phase transition as well as of the no black hole region. At $T = T_1$, a first order phase transition occurs as the thermodynamically favoured state moves from the large black hole branch to the small black hole branch, with a discontinuity in the black hole radius. As the temperature decreases further to T_0, a zeroth order phase transition occurs, when the small black hole transits into an intermediate black hole with a jump in the free-energy. At this pressure, the no black hole region starts at $T = T_n$, the temperature of the upper cusp.

the last slowly accelerating black hole 'moves to the right', eliminating a branch of black holes to the left (denoted by the dashed curve) that no longer obey the slow acceleration condition. As a consequence, the no black hole region continuously grows larger, until a zeroth order phase transition appears at P_0, where the black hole at the red dot has the same temperature as the upper cusp of the swallow tail. For a slightly smaller pressure, there develops a small range of temperatures for which the lower branch is already removed but there is a corresponding new branch of black holes (on the lower left branch of the upper left cusp in Fig. 9.12) that become stable, and we observe a zeroth-order phase transition. This situation holds until the pressure P_f is reached for which the red dot black hole moves all the way to the intersection of the swallow tail, at which point both the zeroth–order and the first order phase transitions simultaneously disappear. For even smaller pressures, the red dot black hole keeps moving further right and no longer occurs

in the stable branch. This behaviour finally terminates at the transition pressure $P_t^{(J)}$ for which the swallowtail snaps and completely disappears, as in the case of a charged black hole.

In other words, in the rotating case the interesting phase behaviour happens above the pressure for which the the actual snapping occurs. This is a consequence of the existence of solutions on the small black hole branch of the swallowtail that develop acceleration horizons and thus do not lie in the admissible parameter space; the corresponding analysis is depicted in Fig. 9.9. Recall from the introduction that solutions with an acceleration horizon are excluded from our parameter space as it introduces a second temperature into the picture which in general differs from the black hole temperature. The resulting black hole will therefore not be in thermodynamic equilibrium.

Reentrant phase transitions

The fact that $P_0 > P_f$ results in a non-trivial negative slope of the zeroth-order coexistence line. As a consequence there will be a temperature driven reentrant phase transition for $P_0 > P > P_f$. For any fixed P in this range, there is a large to small to large black hole phase transition as the temperature monotonically increases, as shown in the inset of Fig. 9.13.

This behaviour can be seen from a different perspective in Fig. 9.12. Beginning at high temperatures $T > T_f$ the stable solution is on the lowest branch of the swallowtail, corresponding to a large black hole. As the temperature decreases the solution moves up and to the left of the swallowtail with the black hole radius decreasing continuously. At $T = T_f$ a first order phase transition occurs as the thermodynamically favoured state moves from the large black hole branch to the small black hole branch at the lower left, with a discontinuity in the black hole radius. As T decreases further, once $T = T_0$ a zeroth order phase transition occurs, when the small black hole transits into an intermediate (large) black hole with a jump in the free-energy. The corresponding branch finally disappears at $T = T_n$, which marks the onset of the no black hole region – as no (slowly accelerating) black holes exist below T_n.

As tension increases, the slope of the first order coexistence line becomes negative in a certain range of temperatures and we can observe a pressure driven reentrant phase transition similar to the charged case. This happens in a tiny range of tensions around $\mu \approx 0.19$ as shown in main part of Fig. 9.13. The double valued first order transition curve leads to a reentrant SBH/LBH/SBH/LBH phase transition as the pressure monotonically decreases from I to F, crossing the first order coexistence line twice and zeroth-order

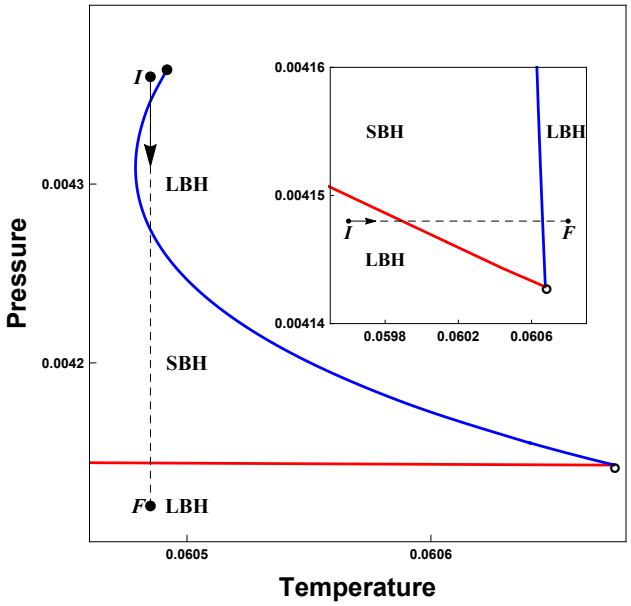

Figure 9.13: **Pressure and temperature driven reentrant phase transitions.** First order (blue) and zeroth order (red) coexistence lines are displayed for $\mu = 0.19$. For this tension the first order line is double-valued, which together with the zeroth-order phase transition, gives rise to a pressure driven SBH/LBH/SBH/LBH reentrant phase transition as we move from the initial point I to the final point F in the diagram. The inset dislays the temperature driven LBH/SBH/LBH phase transition, innate to the rotating case, that happens in the tiny range of pressure $P \in (P_f, P_0)$, as we move from the initial point I to the final point F in the inset.

coexistence line once. Note that whereas the pressure driven reentrant phase transition is also observed for the charged case, the temperature driven reentrant phase transition described above is new.

9.4 Summary

We have discovered that the thermodynamic behaviour of rotating accelerating black holes has subtle but significant distinctions as compared to the their charged counterparts. The key distinction between them is that the coexistence line in a $P - T$ plot separating small black holes from large ones and the NBH region induces a 'fine splitting' of transition pressures. Namely, we observe a sequence of pressures $P_{nbh} > P_0 > P_f$ in which the

minimum pressure possible for a small black hole as $T \to 0$ is larger than the pressure P_0 at the onset of a zeroth order phase transition, which is larger still than the pressure P_f at which the zeroth and first order phase transitions merge. Although the swallowtail still snaps at $P_t^{(J)} < P_f$, this does not affect the global minimum of the free energy and thence has no effect on the equilibrium thermodynamics. This is in contrast to the charged case, for which $P_{nbh} = P_0 = P_f = P_t^{(J)}$, and which in turn leads to the existence of mini-entropic black holes. The splitting is fine in that $P_{nbh} \approx P_0 \approx P_f \approx P_t^{(J)}$, with the correction of the order of μ^2, c.f. Eqs. (9.42) and (9.44). Likewise, the lifting of this pressure degeneracy means that mini-entropic black holes do not exist in the rotating case.

Furthermore, this splitting has an interesting physical consequence in that it admits two kinds of reentrant phase transitions, one at fixed T where the pressure monotonically decreases and one at fixed P in the range $P_0 > P > P_f$ where the temperature monotonically increases. Both these types of phase transitions (although qualitatively different from our case) are also present for black holes with triple points [43].

It is clear that accelerating black holes contain interesting but often subtle new thermodynamic phenomena, and there are still things to be learned. While a full study including both charge and rotation remains to be carried out, of particular interest would be to go beyond the slow-acceleration regime. This would involve the presence of two horizons, with all the associated difficulties this scenario entails [167]. However it might be possible to circumvent these problems by either by placing the system in a cavity [169, 170] or by adjusting parameters to recover thermodynamic equilibrium [171], approaches that have proved to be successful for asymptotically de Sitter black holes.

We have here considered the slow and fast cases as (thermodynamically) 'disconnected', neglecting the branch of fast accelerating black holes completely. Despite the fact that fast accelerating black holes are 'smoothly connected' to slowly accelerating ones in the parameter space, the asymptotic structures of the spacetimes they describe are completely different. A transition from slow to fast acceleration is in many respects similar to a transition from AdS to dS asymptotics: new horizons appear in the fast accelerating case and change drastically the asymptotic and thermodynamic properties of the spacetime, as a comparison of the corresponding Penrose diagrams [149] clearly indicates. Whether or not phase transitions can take place between them remains a question for future investigation.

Chapter 10

Conclusions and Open Questions

10.1 Part I

What have we learned?

In Part I of this thesis, we have investigated how the response of UDW detectors detect non-local spacetime features as well as how the entanglement harvested between a pair of detectors is affected by the presence of moving mirrors in 1+1D.

It has been known that the localized vacuum excitations of quantum fields are affected by global spacetime geometries but what was perhaps not so clear was whether these can be picked up by point-like detectors switched on only for short periods of time. We have found an affirmative answer from the examples in Chapters 4 - 6. In each of the scenarios, the detectors were placed in a shell inside which the spacetime was Minkowski. By interacting with the field for a duration during which no signal could have been exchanged between the shell and the detectors, the detectors were able to detect features about the shell and the exterior spacetime. In Chapter 4, we have seen that the detectors were able to detect the presence of a spherical shell, and that there is an optimal position inside the shell for the detection. In Chapter 5, we have shown that the detectors were further able to distinguish between static and rotating shells of the same mass and radii. However, they were able to do so only when displaced away from the axis of rotation. This illustrates that detection of spacetime features does not follow trivially from the fact that the field vacuum holds non-local information - specific calibration of the detector settings may be necessary. Physically, the addition of rotation to the shell drags inertial detectors inside

into rotation with respect to inertial observers located at infinity. We can thus consider Chapter 5 to be an illustration of quantum detection of inertial frame dragging.

The two scenarios considered in Chapters 4 and 5 both featured curved spacetimes outside of the shells. Chapter 6 presents a slightly different scenario in which the exterior spacetimes are no longer curved but instead feature conical deficits. We have shown that the detectors are able to once again detect the deficit and investigated how the detection depends on parameters such as the detector energy gap, position of the detector and the radius of a second perfectly reflecting shell concentric to the first. Recently, the authors of [172] have considered the more practical aspect of how data collected from UDW detectors can be processed using machine learning to efficiently extract knowledge about the presence of a spherical shell. We refer the reader to this reference for a nice discussion on the general principles behind using local quantum probes to detect global features of the field. We should also stress again that all detections considered here involved the vacuum state of the quantum field — detection of these features using a classical detector with all classical fields in their ground state within the light-crossing time would have been impossible. It will be interesting to investigate how the situation changes when thermal states are considered instead.

In Chapter 7, we have seen a somewhat surprising enhancement of entanglement harvesting in the presence of moving mirrors when the naive expectation might have been a suppression of entanglement due to the additional noise coming from the dynamical Casimir effect. In addition, we found regions of entanglement shadow close to non-static mirrors similar to those seen close to black holes. Another interesting finding is the late time linear increase in entanglement harvested which is analogous to that observed for the (regularized) entanglement entropy of the field when the mirror is asymptotically null.

Recall that our detector-massless scalar field interaction is a toy model for describing interactions of atoms with the quantum EM field. The above investigations tell us that theoretically, different spacetime geometries and boundary conditions will lead to small differences in the spontaneous excitation probabilities of and entanglement harvested between atoms.

Future prospects

Given the above results, there are various immediate extensions which can be considered. For example, it will be interesting to investigate if there is any general correspondence between the entanglement in UDW detectors and the entanglement entropy of the field as seen in Chapter 7. This can be done by exploring situations in which both of these quan-

tities can be computed, such as the various toy-models for gravitational collapse presented in [123]. Such a correspondence, if found, could justify further the use of UDW detectors for studying field entanglement.

One can also imagine placing detectors in the spacetime of a collapsing massive shell and study the resulting response and entanglement between detectors. This would require more advanced computations than that in Chapters 4 and 7, with the shell now being dynamical and the scattering of wave modes being due to an effective potential coming from spacetime curvature instead of a simple Dirichlet boundary. Such a task possibly can only be accomplished fully numerically. It would be interesting to see how much of the features observed in Part I of the thesis will be retained, e.g., can a detector placed inside the shell detect its collapse, will the shell play a similar role to the mirrors of 7 and enhance the entanglement harvested between two detectors placed outside the shell, will entanglement increase linearly in time once a horizon is formed? Entanglement in the quantum field between the regions internal and external to the black hole is the source of the information paradox [10, 11]. Imagine placing one detector inside the collapsing shell and a second detector outside. Naively, the first detector will eventually be destroyed after the shell collapses into a black hole, leaving the total field + second detector system in a mixed state. What is worth considering then is how the entanglement between the two detectors evolve. Perhaps at some point the entanglement drops to zero due to for example the formation of a "firewall" [23] or perhaps a firewall is not necessary for breaking the entanglement. In any case, this study will us provide some insights on the information loss paradox.

Clearly, the situations studied in this thesis remain as toy models as they stand. The considered parameters for the detection of a spherical shell will for example translate into a shell of around $0.01 M_{\odot} \approx 10^{28} Kg$ for a radius of $50\, cm$ while it will clearly be difficult to accelerate a mirror close to the speed of light to investigate entanglement harvesting close to the mirror. However it is not inconceivable that these effects can be experimentally studied in analogue gravity systems [173]. Under this program, analogue systems for investigating the Hawking effect [174, 175, 176], Unruh effect [177, 178, 179] and cosmological particle production [180] have been considered. Experimental demonstration of the dynamical Casimir effect was indeed not achieved by accelerating actual mirrors, but by changing the electrical length of a cavity using a superconductor quantum interference device [46]. Other analogue systems for DCE includes for example [181, 182]. It will be interesting to study whether a suitable analogue system for studying the effects of null mirrors can be found.

10.2 Part II

What have we learned?

In Part II of this thesis, we have studied the phase transitions of slowly accelerating black holes in AdS spacetimes using the thermodynamic quantities found in [162, 161]. We have found a new phenomenon of snapping swallowtails in the $F-T$ diagram, where the entire branch of small black holes disappears. This results in a no black hole phase in the $P-T$ phase diagram, a region in the parameter space where no slowly accelerating black holes exists. We have also observed reentrant phase transitions in both charged and rotating cases respectively at large μ values as well as zeroth order phase transitions in the rotating case.

Future prospects

A natural extension of this work would be to include black holes that are beyond the slowly accelerating regime. These black holes should be the new phase replacing the no black hole region in our phase diagrams. However, the difficulty there is the presence of multiple horizons, being the acceleration horizon in addition to the black hole horizon. The different temperatures of these horizons implies that we no longer have a system in thermodynamic equilibrium. However, one possibility put forward in [162] is to study the thermodynamics of each horizon separately.

As we have seen in the introduction, one of the main motivations of studying black holes in AdS is the AdS/CFT correspondence. Thus having looked at the phase transitions of the bulk AdS black hole, it is natural to ask if it teaches us something about the dual CFT living on the boundary (for example, is there a dual phase transition). Unfortunately the holographic dictionary does not currently allow for a straightforward translation of the studied bulk phase transition to the boundary as it unclear what a variation of Λ corresponds to in the CFT. It has been suggested that variations in Λ correspond to varying the number of degrees of freedom N of the CFT in [183, 184, 185, 186] but [187, 188] showed it corresponded more accurately to variations in both N and the volume of the CFT. In particular by considering variations in the Newton's constant G, it is possible to keep N fixed (which is desirable as this keeps us in the same CFT) while Λ is varied hence variations in Λ should more appropriately be considered as variations in the volume of the CFT. It will thus be interesting to use the dictionary in [187, 188] to translate the thermodynamics in the bulk accelerating black holes to that of the boundary CFT. However as shown recently in [189], variations in δG will redefine the bulk volume term (if N is to be kept

fixed) and thus modify the phase behaviour of the black hole. Hence to understand the phase transitions in the context of holography, the first steps would be to study the bulk using the new volume term, find the dual to $\delta\mu$ and use the dictionary of [187, 188] to relate the bulk to the boundary. While phase transitions of the bulk AdS black hole can be derived solely from classical considerations, duality to the CFT on the boundary provides the quantum degrees of freedom in explaining the origin of the thermodynamic properties of the black hole.

References

[1] Wan Cong, J. Bičák, David Kubizňák, and Robert B. Mann. Quantum distinction of inertial frames: Local versus global. *Phys. Rev. D*, 101:104060, 2020.

[2] Wan Cong, J. Bičák, D. Kubizňák, and Robert B. Mann. Quantum Detection of Inertial Frame Dragging. *Phys. Rev. D*, 103(2):024027, 2021.

[3] Wan Cong, Jiri Bicak, David Kubiznak, and Robert B. Mann. Quantum detection of conicity. *Phys. Lett. B*, 820:136482, 2021.

[4] Wan Cong, Erickson Tjoa, and Robert B. Mann. Entanglement Harvesting with Moving Mirrors. *JHEP*, 06:021, 2019. [Erratum: JHEP 07, 051 (2019)].

[5] Wan Cong, Chen Qian, Michael R. R. Good, and Robert B. Mann. Effects of Horizons on Entanglement Harvesting. *JHEP*, 10:067, 2020.

[6] Niloofar Abbasvandi, Wan Cong, David Kubiznak, and Robert B. Mann. Snapping swallowtails in accelerating black hole thermodynamics. *Class. Quant. Grav.*, 36(10):104001, 2019.

[7] Niloofar Abbasvandi, Wasif Ahmed, Wan Cong, David Kubizňák, and Robert B. Mann. Finely Split Phase Transitions of Rotating and Accelerating Black Holes. *Phys. Rev. D*, 100(6):064027, 2019.

[8] Steven Carlip. Quantum gravity: A Progress report. *Rept. Prog. Phys.*, 64:885, 2001.

[9] S. W. Hawking. Particle Creation by Black Holes. *Commun. Math. Phys.*, 43:199–220, 1975. [,167(1975)].

[10] Samir D. Mathur. The Information paradox: A Pedagogical introduction. *Class. Quant. Grav.*, 26:224001, 2009.

[11] William G. Unruh and Robert M. Wald. Information Loss. *Rept. Prog. Phys.*, 80(9):092002, 2017.

[12] Stephen A. Fulling. Nonuniqueness of canonical field quantization in Riemannian space-time. *Phys. Rev. D*, 7:2850–2862, 1973.

[13] P. C. W. Davies. Scalar particle production in Schwarzschild and Rindler metrics. *J. Phys. A*, 8:609–616, 1975.

[14] W. G. Unruh. Notes on black hole evaporation. *Phys. Rev. D*, 14:870, 1976.

[15] Edward Witten. APS Medal for Exceptional Achievement in Research: Invited article on entanglement properties of quantum field theory. *Rev. Mod. Phys.*, 90(4):045003, 2018.

[16] Tatsuma Nishioka. Entanglement entropy: holography and renormalization group. *Rev. Mod. Phys.*, 90(3):035007, 2018.

[17] Juan Martin Maldacena. The Large N limit of superconformal field theories and supergravity. *Adv. Theor. Math. Phys.*, 2:231–252, 1998.

[18] Edward Witten. Anti-de Sitter space, thermal phase transition, and confinement in gauge theories. *Adv. Theor. Math. Phys.*, 2:505–532, 1998.

[19] Sergey N. Solodukhin. Entanglement entropy of black holes. *Living Rev. Rel.*, 14:8, 2011.

[20] Mark Van Raamsdonk. Building up spacetime with quantum entanglement. *Gen. Rel. Grav.*, 42:2323–2329, 2010.

[21] Eduardo Martin-Martinez and Nicolas C. Menicucci. Entanglement in curved spacetimes and cosmology. *Class. Quant. Grav.*, 31(21):214001, 2014.

[22] Eduardo Martin-Martinez and Jorma Louko. (1+1)D Calculation provides evidence that quantum entanglement survives a firewall. *Phys. Rev. Lett.*, 115(3):031301, 2015.

[23] Ahmed Almheiri, Donald Marolf, Joseph Polchinski, and James Sully. Black Holes: Complementarity or Firewalls? *JHEP*, 02:062, 2013.

[24] Benni Reznik, Alex Retzker, and Jonathan Silman. Violating bell's inequalities in vacuum. *Phys. Rev. A*, 71:042104, 2005.

[25] Andrzej Dragan and Ivette Fuentes. Probing the spacetime structure of vacuum entanglement. 2011, [arXiv: 1105.1192].

[26] Laura J. Henderson, Alessio Belenchia, Esteban Castro-Ruiz, Costantino Budroni, Magdalena Zych, Časlav Brukner, and Robert B. Mann. Quantum Temporal Superposition: The Case of Quantum Field Theory. *Phys. Rev. Lett.*, 125(13):131602, 2020.

[27] Laura J. Henderson and Nicolas C. Menicucci. Bandlimited Entanglement Harvesting. *Phys. Rev. D*, 102(12):125026, 2020.

[28] Benito A Juárez-Aubry and Jorma Louko. Onset and decay of the 1 + 1 hawking–unruh effect: what the derivative-coupling detector saw. *Classical and Quantum Gravity*, 31(24):245007, 2014.

[29] L Sriramkumar and T Padmanabhan. Finite-time response of inertial and uniformly accelerated unruh - DeWitt detectors. *Classical and Quantum Gravity*, 13(8):2061–2079, 1996.

[30] Alejandro Satz. Then again, how often does the Unruh-DeWitt detector click if we switch it carefully? *Class. Quant. Grav.*, 24:1719–1732, 2007.

[31] Daniel Hümmer, Eduardo Martín-Martínez, and Achim Kempf. Renormalized unruh-dewitt particle detector models for boson and fermion fields. *Phys. Rev. D*, 93:024019, 2016.

[32] B R Iyer and A Kumar. Detection of dirac quanta in rindler and black hole spacetimes and the ξ quantisation scheme. *Journal of Physics A: Mathematical and General*, 13(2):469–478, 1980.

[33] Shih-Yuin Lin and B. L. Hu. Backreaction and the unruh effect: New insights from exact solutions of uniformly accelerated detectors. *Phys. Rev. D*, 76:064008, 2007.

[34] Eric G. Brown, Eduardo Martín-Martínez, Nicolas C. Menicucci, and Robert B. Mann. Detectors for probing relativistic quantum physics beyond perturbation theory. *Phys. Rev. D*, 87:084062, 2013.

[35] B. L. Hu, Shih-Yuin Lin, and Jorma Louko. Relativistic Quantum Information in Detectors-Field Interactions. *Class. Quant. Grav.*, 29:224005, 2012.

[36] S. W. Hawking. Gravitational radiation from colliding black holes. *Phys. Rev. Lett.*, 26:1344–1346, 1971.

[37] S. S. Gubser, Igor R. Klebanov, and Alexander M. Polyakov. Gauge theory correlators from noncritical string theory. *Phys. Lett. B*, 428:105–114, 1998.

[38] David Kastor, Sourya Ray, and Jennie Traschen. Enthalpy and the Mechanics of AdS Black Holes. *Class. Quant. Grav.*, 26:195011, 2009.

[39] David Kubiznak and Robert B. Mann. P-V criticality of charged AdS black holes. *JHEP*, 07:033, 2012.

[40] David Kubiznak, Robert B. Mann, and Mae Teo. Black hole chemistry: thermodynamics with Lambda. *Class. Quant. Grav.*, 34(6):063001, 2017.

[41] Sharmila Gunasekaran, Robert B. Mann, and David Kubiznak. Extended phase space thermodynamics for charged and rotating black holes and Born-Infeld vacuum polarization. *JHEP*, 11:110, 2012.

[42] Natacha Altamirano, David Kubiznak, and Robert B. Mann. Reentrant phase transitions in rotating anti–de Sitter black holes. *Phys. Rev.*, D88(10):101502, 2013.

[43] Natacha Altamirano, David Kubiznak, Robert B. Mann, and Zeinab Sherkatghanad. Kerr-AdS analogue of triple point and solid/liquid/gas phase transition. *Class. Quant. Grav.*, 31:042001, 2014.

[44] Keith K. Ng, Robert B. Mann, and Eduardo Martin-Martinez. The equivalence principle and QFT: Can a particle detector tell if we live inside a hollow shell? *Phys. Rev.*, D94(10):104041, 2016.

[45] C W F Everitt, D B DeBra, B W Parkinson, et al. Gravity Probe B: Final Results of a Space Experiment to Test General Relativity. *Phys. Rev. Lett.*, 106:221101, 2011.

[46] C. M. Wilson, G. Johansson, A. Pourkabirian, M. Simoen, J. R. Johansson, Duty T., F. Nori, and P. Delsing. Observation of the dynamical casimir effect in a superconducting circuit. *Nature*, 479:376–379, 2011.

[47] N. D. Birrell and P. C. W. Davies. *Quantum Fields in Curved Space*. Cambridge Monographs on Mathematical Physics. Cambridge University Press, 1982.

[48] Bryce S. DeWitt. *General Relativity: An Einstein Centenary Survey,* edited by S.W. Hawking and W. Israel, pg 680–745. Cambridge University Press, Cambridge, England, 1979.

[49] B. F. Svaiter and N. F. Svaiter. Inertial and noninertial particle detectors and vacuum fluctuations. *Phys. Rev. D*, 46:5267–5277, 1992.

[50] Alejandro Pozas-Kerstjens and Eduardo Martín-Martínez. Harvesting correlations from the quantum vacuum. *Phys. Rev. D*, 92:064042, 2015.

[51] Valerio Scarani. The device-independent outlook on quantum physics. *Acta Physica Slovaca*, 62:347, 2012.

[52] William K. Wootters. Entanglement of formation of an arbitrary state of two qubits. *Phys. Rev. Lett.*, 80:2245–2248, 1998.

[53] Grant Salton, Robert B. Mann, and Nicolas C. Menicucci. Acceleration-assisted entanglement harvesting and rangefinding. *New J. Phys.*, 17:035001, 2015.

[54] Lee Hodgkinson and Jorma Louko. Static, stationary and inertial Unruh-DeWitt detectors on the BTZ black hole. *Phys. Rev. D*, 86:064031, 2012.

[55] Paul Langlois. Causal particle detectors and topology. *Annals of Physics*, 321(9):2027–2070, 2006.

[56] Shih-Yuin Lin, Chung-Hsien Chou, and Bei-Lok Hu. Entanglement Dynamics of Detectors in an Einstein Cylinder. *JHEP*, 03:047, 2016.

[57] Eduardo Martín-Martínez, Alexander R. H. Smith, and Daniel R. Terno. Spacetime structure and vacuum entanglement. *Phys. Rev. D*, 93:044001, 2016.

[58] Alexander R.H. Smith and Robert B. Mann. Looking Inside a Black Hole. *Class. Quant. Grav.*, 31:082001, 2014.

[59] P. C. W. Davies and Adrian C. Ottewill. Detection of negative energy: 4-dimensional examples. *Phys. Rev. D*, 65:104014, 2002.

[60] Eric Poisson. *A Relativist's Toolkit: The Mathematics of Black-Hole Mechanics*. Cambridge University Press, 2004.

[61] Josef Lense and Hans Thirring. Ueber den Einfluss der Eigenrotation der Zentralkoerper auf die Bewegung der Planeten und Monde nach der Einsteinschen Gravitationstheorie. *Phys. Z.*, 19:156–163, 1918.

[62] H. Thirring. Über die Wirkung rotierender ferner Massen in der Einsteinschen Gravitationstheorie. *Phys. Z.*, 19:33, 1918.

[63] Ignazio Ciufolini and John Archibald Wheeler. *Gravitation and Inertia*. Princeton University Press, 1995.

[64] Jiri Bičák, Joseph Katz, Tomas Ledvinka, and Donald Lynden-Bell. Effects of rotating gravitational waves. *Phys. Rev.*, D85:124003, 2012.

[65] W Barker, T Ledvinka, D Lynden-Bell, and J Bičák. Rotation of inertial frames by angular momentum of matter and waves. *Classical and Quantum Gravity*, 34(20):205006, 2017.

[66] C. Misner, K. S. Thorne, and J. A. Wheeler. *Gravitation*. W. H. Freeman, San Francisco, 1973.

[67] James M. Bardeen and Jacobus A. Petterson. The Lense-Thirring Effect and Accretion Disks around Kerr Black Holes. *Astrophys. J. Lett.*, 195:L65, 1975.

[68] J.B. Barbour and H. Pfister, editors. *Mach's principle: From Newton's bucket to quantum gravity. Proceedings, Conference, Tuebingen, Germany, July 1993*. Birkhauser, Boston, USA, 1995.

[69] Herbert Pfister and Markus King. *Inertia and Gravitation: The Fundamental Nature and Structure of Space-Time,* Lecture Notes in Physics, volume 897. Springer International Publishing, Cham, 2015.

[70] H Pfister and K H Braun. Induction of correct centrifugal force in a rotating mass shell. *Classical and Quantum Gravity*, 2(6):909–918, 1985.

[71] Dieter R. Brill and Jeffrey M. Cohen. Rotating masses and their effect on inertial frames. *Phys. Rev.*, 143:1011–1015, 1966.

[72] C W F Everitt, B Muhlfelder, D B DeBra, et al. The gravity probe b test of general relativity. *Classical and Quantum Gravity*, 32(22):224001, 2015.

[73] J Katz, D Lynden-Bell, and J Bičák. Instantaneous inertial frames but retarded electromagnetism in rotating relativistic collapse. *Classical and Quantum Gravity*, 15(10):3177–3194, 1998.

[74] T. Levi-Civita. ds^2 einsteiniani in campi newtoniani. IX: L'analogo del potenziale logaritmico. *Rend. Accad. Lencei*, 28:101–109, 1919.

[75] M. B. Hindmarsh and T. W. B. Kibble. Cosmic strings. *Rept. Prog. Phys.*, 58:477–562, 1995.

[76] A. Vilenkin and E. P. S. Shellard. *Cosmic Strings and Other Topological Defects*. Cambridge University Press, 2000.

[77] A. Vilenkin. Gravitational Field of Vacuum Domain Walls and Strings. *Phys. Rev. D*, 23:852–857, 1981.

[78] III Gott, J. R. Gravitational lensing effects of vacuum strings - Exact solutions. *Astrophysical Journal*, 288:422–427, 1985.

[79] Holger Bech Nielsen and P. Olesen. Vortex Line Models for Dual Strings. *Nucl. Phys. B*, 61:45–61, 1973.

[80] David Garfinkle. General relativistic strings. *Phys. Rev. D*, 32:1323–1329, 1985.

[81] Jens Boos. Angle deficit and nonlocal gravitoelectromagnetism around a slowly spinning cosmic string. *Int. J. Mod. Phys. D*, 29(14):2043027, 2020.

[82] T. M. Helliwell and D. A. Konkowski. VACUUM FLUCTUATIONS OUTSIDE COSMIC STRINGS. *Phys. Rev. D*, 34:1918–1920, 1986.

[83] Valeri P. Frolov and E. M. Serebryanyi. Vacuum Polarization in the Gravitational Field of a Cosmic String. *Phys. Rev. D*, 35:3779–3782, 1987.

[84] B. Linet. Quantum Field Theory in the Space-time of a Cosmic String. *Phys. Rev. D*, 35:536–539, 1987.

[85] Diego D. Harari and Vladimir D. Skarzhinsky. Pair Production in the Gravitational Field of a Cosmic String. *Phys. Lett. B*, 240:322–326, 1990.

[86] Vladimir D. Skarzhinsky, Diego D. Harari, and Ulf Jasper. Quantum electrodynamics in the gravitational field of a cosmic string. *Phys. Rev. D*, 49:755–762, 1994.

[87] P. C. W. Davies and Varun Sahni. Quantum gravitational effects near cosmic strings. *Class. Quant. Grav.*, 5:1, 1988.

[88] Wenting Zhou and Hongwei Yu. Spontaneous excitation of a uniformly accelerated atom in the cosmic string spacetime. *Phys. Rev. D*, 93:084028, 2016.

[89] A.M. Amirkhanjan, V.P. Frolov, and V.D. Skarzhinsky. Detector in the gravitational field of a cosmic string. *Astroparticle Physics*, 3(2):197 – 208, 1995.

[90] A. H. Bilge, M. Hortacsu, and N. Ozdemir. Can an Unruh detector feel a cosmic string? *Gen. Rel. Grav.*, 30:861–876, 1998.

[91] Wenting Zhou and Hongwei Yu. Boundarylike behaviors of the resonance interatomic energy in a cosmic string spacetime. *Phys. Rev. D*, 97(4):045007, 2018.

[92] G. De A. Marques, J. G. de Assis, and V. B. Bezerra. Some effects on quantum systems due to the gravitational field of a cosmic string. *J. Math. Phys.*, 48:112501, 2007.

[93] Ying Yang, Jieci Wang, Mengjie Wang, Jiliang Jing, and Zehua Tian. Parameter estimation in cosmic string spacetime by using the inertial and accelerated detectors. *Class. Quant. Grav.*, 37(6):065017, 2020.

[94] Pingyang He, Hongwei Yu, and Jiawei Hu. Entanglement dynamics for static two-level atoms in cosmic string spacetime. *Eur. Phys. J. C*, 80(2):134, 2020.

[95] J. Bičák and M Žofka. Notes on static cylindrical shells. *Classical and Quantum Gravity*, 19(14):3653–3664, 2002.

[96] Thomas G. Philbin. Perfect fluid cylinders and walls: Sources for the Levi-Civita space-time. *Class. Quant. Grav.*, 13:1217–1232, 1996.

[97] J. Bičák, T. Ledvinka, B. G. Schmidt, and M. Žofka. Static fluid cylinders and their fields: Global solutions. *Class. Quant. Grav.*, 21:1583–1608, 2004.

[98] Paul C. W. Davies, Tevian Dray, and Corinne A. Manogue. Detecting the rotating quantum vacuum. *Phys. Rev. D*, 53:4382–4387, 1996.

[99] G. W. Gibbons and S. W. Hawking. Cosmological event horizons, thermodynamics, and particle creation. *Phys. Rev. D*, 15:2738–2751, 1977.

[100] Greg L. Ver Steeg and Nicolas C. Menicucci. Entangling power of an expanding universe. *Phys. Rev. D*, 79:044027, 2009.

[101] Antony Valentini. Non-local correlations in quantum electrodynamics. *Physics Letters A*, 153(6):321 – 325, 1991.

[102] Laura J. Henderson, Robie A. Hennigar, Robert B. Mann, Alexander R. H. Smith, and Jialin Zhang. Harvesting Entanglement from the Black Hole Vacuum. *Class. Quant. Grav.*, 35(21):21LT02, 2018.

[103] Kensuke Gallock-Yoshimura, Erickson Tjoa, and Robert B. Mann. Harvesting Entanglement with Detectors Freely Falling into a Black Hole. 2021, [arXiv: 2102.09573].

[104] David C. M. Ostapchuk, Shih-Yuin Lin, Robert B. Mann, and B. L. Hu. Entanglement Dynamics between Inertial and Non-uniformly Accelerated Detectors. *JHEP*, 07:072, 2012.

[105] Keith K. Ng, Robert B. Mann, and Eduardo Martín-Martínez. Unruh-DeWitt detectors and entanglement: The anti–de Sitter space. *Phys. Rev. D*, 98(12):125005, 2018.

[106] Alejandro Pozas-Kerstjens, Jorma Louko, and Eduardo Martin-Martinez. Degenerate detectors are unable to harvest spacelike entanglement. *Phys. Rev. D*, 95(10):105009, 2017.

[107] Shih-Yuin Lin, Chung-Hsien Chou, and Bei-Lok Hu. Entanglement Dynamics of Detectors in an Einstein Cylinder. *JHEP*, 03:047, 2016.

[108] Eduardo Martín-Martínez and Jorma Louko. $(1+1)$D calculation provides evidence that quantum entanglement survives a firewall. *Phys. Rev. Lett.*, 115:031301, 2015.

[109] P.C.W. Davies and S.A. Fulling. Radiation from a moving mirror in two-dimensional space-time conformal anomaly. *Proc. Roy. Soc. Lond. A*, A348:393–414, 1976.

[110] P. C. W. Davies and S. A. Fulling. Radiation from Moving Mirrors and from Black Holes. *Proc. Roy. Soc. Lond.*, A356:237–257, 1977.

[111] Robert D. Carlitz and Raymond S. Willey. Reflections on moving mirrors. *Phys. Rev. D*, 36:2327–2335, 1987.

[112] Paul R. Anderson, Michael R. R. Good, and Charles R. Evans. *Black hole - moving mirror I: An exact correspondence*, pages 1701–1704.

[113] Michael R. R. Good, Paul R. Anderson, and Charles R. Evans. *Black hole - moving mirror II: Particle creation*, pages 1705–1708.

[114] Michael R. R. Good, Paul R. Anderson, and Charles R. Evans. Mirror reflections of a black hole. *Phys. Rev. D*, 94:065010, 2016.

[115] Eugenio Bianchi and Matteo Smerlak. Entanglement entropy and negative energy in two dimensions. *Phys. Rev. D*, 90(4):041904, 2014.

[116] Michael R. R. Good, Paul R. Anderson, and Charles R. Evans. Time dependence of particle creation from accelerating mirrors. *Phys. Rev. D*, 88:025023, 2013.

[117] Michael R.R. Good, Yen Chin Ong, Aizhan Myrzakul, and Khalykbek Yelshibekov. Information preservation for null shell collapse: a moving mirror model. *Gen. Rel. Grav.*, 51(7):92, 2019.

[118] Shih-Yuin Lin, Chung-Hsien Chou, and B.L. Hu. Disentanglement of two harmonic oscillators in relativistic motion. *Phys. Rev. D*, 78:125025, 2008.

[119] David C.M. Ostapchuk, Shih-Yuin Lin, Robert B. Mann, and B.L. Hu. Entanglement Dynamics between Inertial and Non-uniformly Accelerated Detectors. *JHEP*, 07:072, 2012.

[120] Eduardo Martín-Martínez, Alexander R. H. Smith, and Daniel R. Terno. Spacetime structure and vacuum entanglement. *Phys. Rev. D*, 93:044001, 2016.

[121] Laura J. Henderson, Robie A. Hennigar, Robert B. Mann, Alexander R.H. Smith, and Jialin Zhang. Entangling detectors in anti-de Sitter space. *JHEP*, 05:178, 2019.

[122] Michael R. R. Good, Khalykbek Yelshibekov, and Yen Chin Ong. On Horizonless Temperature with an Accelerating Mirror. *JHEP*, 03:013, 2017.

[123] Eugenio Bianchi, Tommaso De Lorenzo, and Matteo Smerlak. Entanglement entropy production in gravitational collapse: covariant regularization and solvable models. *JHEP*, 06:180, 2015.

[124] J. M. Bardeen, B. Carter, and S. W. Hawking. The four laws of black hole mechanics. *Communications in Mathematical Physics*, 31(2):161–170, 1973.

[125] Robert M. Wald. *General Relativity*. Chicago Univ. Pr., Chicago, USA, 1984.

[126] D. Sudarsky and Robert M. Wald. Extrema of mass, stationarity, and staticity, and solutions to the Einstein Yang-Mills equations. *Phys. Rev. D*, 46:1453–1474, 1992.

[127] Robert M. Wald. Black hole entropy is the Noether charge. *Phys. Rev. D*, 48(8):R3427–R3431, 1993.

[128] H. Lü, C. N. Pope, and Qiang Wen. Thermodynamics of ads black holes in einstein-scalar gravity. *Journal of High Energy Physics*, 2015(3):165, 2015.

[129] S. W. Hawking and J. B. Hartle. Energy and angular momentum flow into a black hole. *Commun. Math. Phys.*, 27:283–290, 1972.

[130] M. Cvetic, G. W. Gibbons, D. Kubiznak, and C. N. Pope. Black Hole Enthalpy and an Entropy Inequality for the Thermodynamic Volume. *Phys. Rev.*, D84:024037, 2011.

[131] Robie A. Hennigar, David Kubiznak, and Robert B. Mann. Entropy Inequality Violations from Ultraspinning Black Holes. *Phys. Rev. Lett.*, 115(3):031101, 2015.

[132] Dietmar Klemm. Four-dimensional black holes with unusual horizons. *Phys. Rev.*, D89(8):084007, 2014.

[133] Robie A. Hennigar, David Kubizňák, Robert B. Mann, and Nathan Musoke. Ultraspinning limits and super-entropic black holes. *JHEP*, 06:096, 2015.

[134] Wilson G. Brenna, Robert B. Mann, and Miok Park. Mass and Thermodynamic Volume in Lifshitz Spacetimes. *Phys. Rev.*, D92(4):044015, 2015.

[135] S. M. Noorbakhsh and M. Ghominejad. Ultra-Spinning Gauged Supergravity Black Holes and their Kerr/CFT Correspondence. *Phys. Rev.*, D95(4):046002, 2017.

[136] S. M. Noorbakhsh and M. Ghominejad. Higher Dimensional Charged AdS Black Holes at Ultra-spinning Limit and Their 2d CFT Duals. 2017, [arXiv:1702.03448].

[137] Xing-Hui Feng, Hai-Shan Liu, Wen-Tian Lu, and H. Lu. Horndeski Gravity and the Violation of Reverse Isoperimetric Inequality. *Eur. Phys. J.*, C77(11):790, 2017.

[138] S. M. Noorbakhsh and M. H. Vahidinia. Extremal Vanishing Horizon Kerr-AdS Black Holes at Ultraspinning Limit. *JHEP*, 01:042, 2018.

[139] R. B. Mann. Super-Entropic Black Holes. *Springer Proc. Phys.*, 208:105–113, 2018.

[140] Brian P. Dolan, Anna Kostouki, David Kubiznak, and Robert B. Mann. Isolated critical point from Lovelock gravity. *Class. Quant. Grav.*, 31(24):242001, 2014.

[141] Antonia M. Frassino, David Kubiznak, Robert B. Mann, and Fil Simovic. Multiple Reentrant Phase Transitions and Triple Points in Lovelock Thermodynamics. *JHEP*, 09:080, 2014.

[142] Robie A. Hennigar, Robert B. Mann, and Erickson Tjoa. Superfluid Black Holes. *Phys. Rev. Lett.*, 118(2):021301, 2017.

[143] T. Narayanan and Anil Kumar. Reentrant phase transitions in multicomponent liquid mixtures. *Physics Reports*, 249(3):135–218, 1994.

[144] Shao-Wen Wei, Peng Cheng, and Yu-Xiao Liu. Analytical and exact critical phenomena of d-dimensional singly spinning Kerr-AdS black holes. *Phys. Rev. D*, 93(8):084015, 2016.

[145] Robie A. Hennigar and Robert B. Mann. Reentrant phase transitions and van der Waals behaviour for hairy black holes. *Entropy*, 17(12):8056–8072, 2015.

[146] H. Weyl. The theory of gravitation. *Annalen Phys.*, 359:117–145, 1917.

[147] Tullio Levi-Civita. ds2 einsteiniani in campi newtoniani. *Rend. Acc. Lincei*, 27:343, 1918.

[148] William Kinnersley and Martin Walker. Uniformly accelerating charged mass in general relativity. *Physical Review D*, 2(8):1359, 1970.

[149] Jiri Podolsky, Marcello Ortaggio, and Pavel Krtous. Radiation from accelerated black holes in an anti-de Sitter universe. *Phys. Rev.*, D68:124004, 2003.

[150] Fay Dowker, Jerome P. Gauntlett, David A. Kastor, and Jennie H. Traschen. Pair creation of dilaton black holes. *Phys. Rev.*, D49:2909–2917, 1994.

[151] S. Ross. Black hole pair creation. In *The future of theoretical physics and cosmology: Celebrating Stephen Hawking's 60th birthday. Proceedings, Workshop and Symposium, Cambridge, UK, January 7-10, 2002*, pages 264–277, 2002.

[152] Ruth Gregory and Mark Hindmarsh. Smooth metrics for snapping strings. *Phys. Rev.*, D52:5598–5605, 1995.

[153] Douglas M. Eardley, Gary T. Horowitz, David A. Kastor, and Jennie H. Traschen. Breaking cosmic strings without monopoles. *Phys. Rev. Lett.*, 75:3390–3393, 1995.

[154] Roberto Emparan and Harvey S. Reall. A Rotating black ring solution in five-dimensions. *Phys. Rev. Lett.*, 88:101101, 2002.

[155] Michael Appels, Ruth Gregory, and David Kubiznak. Thermodynamics of Accelerating Black Holes. *Phys. Rev. Lett.*, 117(13):131303, 2016.

[156] Michael Appels, Ruth Gregory, and David Kubiznak. Black Hole Thermodynamics with Conical Defects. *JHEP*, 05:116, 2017.

[157] Ruth Gregory. Accelerating Black Holes. *J. Phys. Conf. Ser.*, 942(1):012002, 2017.

[158] Marco Astorino. CFT Duals for Accelerating Black Holes. *Phys. Lett.*, B760:393–405, 2016.

[159] Marco Astorino. Thermodynamics of Regular Accelerating Black Holes. *Phys. Rev.*, D95(6):064007, 2017.

[160] Jialin Zhang, Yanjun Li, and Hongwei Yu. Thermodynamics of charged accelerating AdS black holes and holographic heat engines. *JHEP*, 02:144, 2019.

[161] Andres Anabalon, Michael Appels, Ruth Gregory, David Kubiznak, Robert B. Mann, and Alï Ovgun. Holographic Thermodynamics of Accelerating Black Holes. *Phys. Rev.*, D98:104038, 2018.

[162] Andrés Anabalón, Finnian Gray, Ruth Gregory, David Kubizňák, and Robert B. Mann. Thermodynamics of Charged, Rotating, and Accelerating Black Holes. *JHEP*, 04:096, 2019.

[163] S. W. Hawking and Don N. Page. Thermodynamics of Black Holes in anti-De Sitter Space. *Commun. Math. Phys.*, 87:577, 1983.

[164] Jiri Podolsky. Accelerating black holes in anti-de Sitter universe. *Czech. J. Phys.*, 52:1–10, 2002.

[165] Kenneth Hong and Edward Teo. A New form of the rotating C-metric. *Class. Quant. Grav.*, 22:109–118, 2005.

[166] J. B. Griffiths and J. Podolsky. A New look at the Plebanski-Demianski family of solutions. *Int. J. Mod. Phys.*, D15:335–370, 2006.

[167] David Kubiznak and Fil Simovic. Thermodynamics of horizons: de Sitter black holes and reentrant phase transitions. *Class. Quant. Grav.*, 33(24):245001, 2016.

[168] Ruth Gregory and Andrew Scoins. Accelerating Black Hole Chemistry. *Phys. Lett. B*, 796:191–195, 2019.

[169] Fil Simovic and Robert.B. Mann. Critical Phenomena of Charged de Sitter Black Holes in Cavities. *Class. Quant. Grav.*, 36(1):014002, 2019.

[170] Fil Simovic and Robert B. Mann. Critical phenomena of born-infeld-de sitter black holes in cavities. *Journal of High Energy Physics*, 2019(5):136, 2019.

[171] Saoussen Mbarek and Robert B. Mann. Reverse Hawking-Page Phase Transition in de Sitter Black Holes. *JHEP*, 02:103, 2019.

[172] Daniel Grimmer, Irene Melgarejo-Lermas, and Eduardo Martín-Martínez. Machine learning quantum field theory with local probes. 10 2019.

[173] Carlos Barcelo, Stefano Liberati, and Matt Visser. Analogue gravity. *Living Rev. Rel.*, 8:12, 2005.

[174] F. Belgiorno, S. L. Cacciatori, M. Clerici, V. Gorini, G. Ortenzi, L. Rizzi, E. Rubino, V. G. Sala, and D. Faccio. Hawking radiation from ultrashort laser pulse filaments. *Phys. Rev. Lett.*, 105:203901, 2010.

[175] Juan Ramón Muñoz de Nova, Katrine Golubkov, Victor I. Kolobov, and Jeff Steinhauer. Observation of thermal Hawking radiation and its temperature in an analogue black hole. *Nature*, 569(7758):688–691, 2019.

[176] Jonathan Drori, Yuval Rosenberg, David Bermudez, Yaron Silberberg, and Ulf Leonhardt. Observation of stimulated hawking radiation in an optical analogue. *Phys. Rev. Lett.*, 122:010404, 2019.

[177] A. Retzker, J. I. Cirac, M. B. Plenio, and B. Reznik. Methods for detecting acceleration radiation in a bose-einstein condensate. *Phys. Rev. Lett.*, 101:110402, 2008.

[178] Steffen Biermann, Sebastian Erne, Cisco Gooding, Jorma Louko, Jörg Schmiedmayer, William G. Unruh, and Silke Weinfurtner. Unruh and analogue Unruh temperatures for circular motion in 3+1 and 2+1 dimensions. *Phys. Rev. D*, 102(8):085006, 2020.

[179] Cisco Gooding, Steffen Biermann, Sebastian Erne, Jorma Louko, William G. Unruh, Joerg Schmiedmayer, and Silke Weinfurtner. Interferometric Unruh detectors for Bose-Einstein condensates. *Phys. Rev. Lett.*, 125(21):213603, 2020.

[180] Ralf Schutzhold, Michael Uhlmann, Lutz Petersen, Hector Schmitz, Axel Friedenauer, and Tobias Schatz. Analogue of cosmological particle creation in an ion trap. *Phys. Rev. Lett.*, 99:201301, 2007.

[181] J. C. Jaskula, G. B. Partridge, M. Bonneau, R. Lopes, J. Ruaudel, D. Boiron, and C. I. Westbrook. An acoustic analog to the dynamical Casimir effect in a Bose-Einstein condensate. *Phys. Rev. Lett.*, 109:220401, 2012.

[182] Iacopo Carusotto, Roberto Balbinot, Alessandro Fabbri, and Alessio Recati. Density correlations and dynamical Casimir emission of Bogoliubov phonons in modulated atomic Bose-Einstein condensates. *Eur. Phys. J. D*, 56:391–404, 2010.

[183] Clifford V. Johnson. Holographic Heat Engines. *Class. Quant. Grav.*, 31:205002, 2014.

[184] Brian P. Dolan. Bose condensation and branes. *Journal of High Energy Physics*, 2014(10):179, 2014.

[185] David Kastor, Sourya Ray, and Jennie Traschen. Chemical Potential in the First Law for Holographic Entanglement Entropy. *JHEP*, 11:120, 2014.

[186] Elena Caceres, Phuc H. Nguyen, and Juan F. Pedraza. Holographic entanglement entropy and the extended phase structure of STU black holes. *JHEP*, 09:184, 2015.

[187] Andreas Karch and Brandon Robinson. Holographic Black Hole Chemistry. *JHEP*, 12:073, 2015.

[188] Manus R. Visser. Holographic Thermodynamics Requires a Chemical Potential for Color. 2021, [arXiv:2101.04145].

[189] Wan Cong, David Kubiznak, and Robert B. Mann. Thermodynamics of AdS Black Holes: Central Charge Criticality. 2021, [arXiv:2105.02223].

Appendices

Appendix A

Stress-Energy of Spherical Shells

In this Appendix, we will recall the stress-energy tensor of a rotating spherical shell (setting $a = 0$ gives the results for the static spherical shell). This follows closely the presentation in [60].

As we have seen in Sec. 4.1, the second junction condition on the shell Σ relates the discontinuity in the derivatives of the metric, or equivalently in the extrinsic curvature K_{ij}, to the stress-energy tensor S_{ij} on Σ:

$$S_{ij} = -\frac{1}{8\pi}\Big([K_{ij}] - [K]h_{ij}\Big)\,. \tag{A.1}$$

Using the metric (5.1) exterior to our rotating spherical shell, the nonvanishing components of the extrinsic curvature turn out to be [60],

$$\begin{aligned}
K^t_{\ t} &= \frac{M}{R^2\sqrt{1-2M/R}}\,,\\
K^t_{\ \varphi} &= -\frac{3Ma\sin^2\theta}{R^2\sqrt{1-2M/R}}\,,\\
K^\varphi_{\ t} &= \frac{3Ma}{R^4}\sqrt{1-2M/R}\,,\\
K^\theta_{\ \theta} &= \frac{1}{R}\sqrt{1-2M/R} = K^\varphi_{\ \varphi}\,.
\end{aligned} \tag{A.2}$$

Meanwhile, the nonvanishing components of the extrinsic curvature as seen from the inside

are $K^\theta_\theta = K^\varphi_\varphi = 1/R$. From these, we obtain

$$\begin{aligned} S^t_t &= -\frac{1}{4\pi R}(1-\sqrt{1-2M/R})\,, \\ S^t_\varphi &= \frac{3Ma\sin^2\theta}{8\pi R^2\sqrt{1-2M/R}}\,, \\ S^\varphi_t &= -\frac{3Ma}{8\pi R^4}\sqrt{1-2M/R}\,, \\ S^\theta_\theta &= \frac{1-M/R-\sqrt{1-2M/R}}{8\pi R\sqrt{1-2M/R}} = S^\varphi_\varphi\,. \end{aligned} \tag{A.3}$$

This stress energy can be understood as describing a 2D perfect-fluid with a velocity field u^i, a surface density σ and a surface pressure p by rewriting it in the form

$$S^{ij} = \sigma u^i u^j + p(h^{ij} + u^i u^j)\,. \tag{A.4}$$

Specifically, we have [60]

$$\begin{aligned} \sigma &= \frac{1}{4\pi R}(1-\sqrt{1-2M/R})\,, \\ p &= \frac{1-M/R-\sqrt{1-2M/R}}{8\pi R\sqrt{1-2M/R}}\,, \\ u^i &= \frac{t^i + \tilde{\Omega}\varphi^i}{\sqrt{1-2M/R}}\,, \end{aligned} \tag{A.5}$$

where $t^i = (\partial/\partial t)^i$ and $\varphi^i = (\partial/\partial\varphi)^i$ and

$$\tilde{\Omega} = \frac{6Ma}{R^3}\frac{1-2M/R}{(1-\sqrt{1-2M/R})(1+3\sqrt{1-2M/R})}\,. \tag{A.6}$$

Hence the stress-energy tensor describes a perfect-fluid rotating rigidly with angular velocity $d\varphi/dt = \tilde{\Omega}$ with respect to inertial observers inside the shell. For $R \to 2M$, $\tilde{\Omega} \to 0$, the inertial observers are dragged completely by the shell. The angular velocity in the ϕ coordinate, i.e. with respect to static observers at infinity, is $\tilde{\Omega}_{\rm shell} = d\phi/dt = \tilde{\Omega} + 2Ma/R^3$, which is,

$$\tilde{\Omega}_{\rm shell} = \frac{2Ma}{R^3}\frac{1+2\sqrt{1-2M/R}}{(1-\sqrt{1-2M/R})(1+3\sqrt{1-2M/R})}\,. \tag{A.7}$$

Appendix B

Stress-Energy of Cylindrical Shells

In this Appendix we briefly review the stress-energy tensor of the cylindrical shell following the discussions in [95]. The general line element of a spacetime admitting cylindrical symmetry has the form,

$$ds^2 = -e^{2U(\tilde{r})}d\tilde{t}^2 + e^{-2U(\tilde{r})}[A(\tilde{r})^2 d\tilde{r}^2 + B(\tilde{r})^2 d\varphi^2 + C(\tilde{r})^2 d\tilde{z}^2]\,. \tag{B.1}$$

By substituting this ansatz into the vacuum Einstein's field equations, after appropriate rescaling and translation of the coordinates, the general solution has three arbitrary constants, r_0, m and c [97]:

$$ds^2 = -\big(\frac{r}{r_0}\big)^{2m} d\tau^2 + \big(\frac{r}{r_0}\big)^{2m(m-1)}(d\zeta^2 + dr^2) + r^2\big(\frac{r}{r_0}\big)^{-2m} d\varphi^2/c^2, \tag{B.2}$$

with the coordinate ranges $\tau \in \mathbb{R}$, $r \in \mathbb{R}^+$, $\zeta \in \mathbb{R}$ and $\varphi \in [0, 2\pi)$. However, we can get rid of r_0 by another coordinate rescaling

$$(\tau, \zeta, r, \varphi) \to (r_0^{\frac{m}{m^2-m+1}} t, r_0^{\frac{m(m-1)}{m^2-m+1}} z, r_0^{\frac{m(m-1)}{m^2-m+1}} \rho, \varphi)\,,$$

so that the final metric reads:

$$ds^2 = -\rho^{2m} dt^2 + \rho^{-2m}\Big[\rho^{2m^2}(dz^2 + d\rho^2) + \rho^2 d\varphi^2/c^2\Big]\,. \tag{B.3}$$

We are thus left with only 2 physical parameters m and c for the spacetime. This is the common form of the Levi-Civita metric appearing in the literature.

We now move on to discuss the cylindrical shell that can give rise to such a metric. A general cylindrical shell spacetime consists of two regions, each described by the metric in Eq. (B.3) with specific parameter choices: an "inside" region which is regular along the z-axis with $c_- = 1$ and $m_- = 0$ running from $0 \leq \rho_- \leq R_-$, and an "outside" region with arbitrary c_+ and m_+ running from $\tilde{R}_1 \leq \rho_+ \leq \tilde{R}_2$. These two regions are joined at the shell surface using the junction conditions, which sets $R_1 = \tilde{R}_1^{1-m_+}/c$, as well as the non-vanishing components of the stress-tensor of the shell as:

$$\begin{aligned} 8\pi S_{tt} &= 1/R_1 - \tilde{R}_1^{m_+ - m_+^2 - 1}(1 - m_+)^2 \,, \\ 8\pi S_{zz} &= \tilde{R}_1^{m_+ - m_+^2 - 1} - 1/R_1 \,, \\ 8\pi S_{\varphi\varphi} &= \tilde{R}_1^{m_+ - m_+^2 - 1} m_+^2 \,. \end{aligned} \tag{B.4}$$

We can define the mass per unit coordinate length of the cylinder as $\mu = 2\pi R_1 S_{tt}$, which in terms of the spacetime parameters, reads,

$$\mu = \frac{1}{4}\left(1 - \frac{1}{c_+}\frac{(1 - m_+)^2}{\tilde{R}_1^{m_+^2}}\right). \tag{B.5}$$

As we were only interested in studying the sensitivity of a UDW to the conical deficit outside the cylinder, we have set $m_+ = 0$ in the main text to avoid any effects on the UDW due to non-trivial curvature outside the cylinder. However, we see here that even in this case, the shell has a non-zero mass per unit length, given by Eq. (6.4) in the main text.